Irreversible Oxidation Reaction in Aqueous Rechargeable Zn-MnO₂ Batteries and Its Elimination for High Reversibility at Low Current Density

by

Yan Wu

A thesis

presented to the University of Waterloo

in fulfillment of the

thesis requirement for the degree of

Master of Applied Science

in

Chemical Engineering (Nanotechnology)

Waterloo, Ontario, Canada, 2021

Author's Declaration

I hereby declare that I am the sole author of this thesis. This is a true copy of the thesis, including any required final revisions, as accepted by my examiners.

I understand that my thesis may be made electronically available to the public.

Abstract

With the ascending requirements of global energy storage, secondary batteries are receiving significant attentions. Lithium-ion batteries (LIBs) have been dominating the market over the decades because of their superior energy density. However, shortages of LIBs such as safety issues, low storage in earth's crust restrict their applications. Therefore, seeking for alternative battery systems is becoming one of the most urgent topics. Rechargeable aqueous zinc-ion batteries (RAZIBs) are considered as potential candidates for large-scale energy storage because of their remarkable specific capacity from zinc metal (820 mAhg^{-1}), high safety, and environmentally friendliness. Among the choices for cathode materials involving vanadium oxides, sodium manganese oxides, and Prussian blue analogue, MnO_2 receives significant attention for its high theoretical capacity (308 mAhg^{-1} for 1 e$^-$ transfer; 615 mAhg^{-1} for 2 e$^-$ transfer) and non-toxicity.

Although rechargeable aqueous Zn/MnO_2 batteries have been researched for decades, the complicated cathode reactions are still not fully understood, especially the negative influences from the pH fluctuations during cycling and controversial discussions on Mn^{2+} additives. Additionally, the cycle life of the batteries under relatively low current density is not satisfactory. Hence, a series of experiments are performed in this work to study the reaction mechanism and capacity fading mechanism in Zn/MnO_2 batteries. Also, an efficient method on proton regulating to enhance the cycling performance was proposed.

Firstly, the main cathode reactions are addressed by characterization methods such as inductively coupled plasma mass spectrometry (ICP-MS), scanning electron microscopy

(SEM), transmission electron microscopy (TEM). It is demonstrated that conversion reactions ($MnO_2 \leftrightarrow MnOOH$) and dissolution/deposition reactions ($MnO_2 \leftrightarrow Mn^{2+}$) are the 2 types of main reactions happening in Zn/MnO_2 batteries. Zinc intercalations are not observed according to the characterization results. Afterwards, the irreversible side reactions which cause capacity loss are researched. It is reported in this work that side product from pH fluctuation, zinc sulphate hydroxide hydrates ($Zn_4(OH)_6SO_4 \cdot 5H_2O$, or ZHS), can react with Mn^{2+} ions when charged over 1.55V (vs. Zn/Zn^{2+}). The product generated from this reaction is identified as a lowly crystallized Woodruffite (($Zn,Mn)_2Mn_5O_{12} \cdot 4H_2O$, or ZMO), which is also demonstrated to be irreversible and harmful for the battery performance. This reaction is considered as the direct reason for short cycle life of Zn/MnO_2 batteries.

Therefore, strongly acidic cation exchange resin is used to modify the proton concentration locally (near cathode) and suppress the growth of ZHS side products during discharge process. As a result, the ZHS side product is eliminated at 1.55V (vs. Zn/Zn^{2+}) during charge process, and the irreversible reaction is hence inhibited. Without the undesired side reaction, the proposed battery with ion exchange resin can achieve significant improvements in both cycling performance and Coulombic efficiency at low C-rate, compared with the batteries without ion exchange resin.

Acknowledgements

Firstly, I would like to express my sincere gratitude to my academic supervisor, Professor Pu Chen, for providing the opportunity for me to pursue my graduate studies. His guidance and support are deeply appreciated. Without his guidance and input, this research could not have been successfully conducted.

Also, I would like to thank my advisory committee members, Professor Eric Croiset and Professor Yuning Li, for their valuable time and meaningful feedback towards the completion of this thesis.

I would like to express my heartfelt appreciation to my research colleagues including Dr. Yu Liu, Dr. Jian Zhi, Mei Han, Qiuyu Shi, Zhongyi Liu, Yuxiao Jiao and Feng Zhao for their selfless help in both lab work and daily life. I sincerely enjoy and will always remember the days we spent together.

Last but not least, I would like to express my sincere love to my parents, Hongjun Wu, Hua Zhong, and all my family members for their endless love and mental support. I would also like to thank my girlfriend, Zhaoyi Yin, for her dedication and mental support during my master career.

Table of Contents

List of Figures

xi

List of Tables

Chapter 1: Introduction

1.1 Rechargeable Batteries

Facing the challenge of global warming and energy crisis, the world is paying increasing attention to sustainable energy sources such as solar, wind, hydroelectric, biomass, and hydropower.[1] As the amount of energy produced rises, so does the demand for energy storage systems (ESS).[2] Rechargeable battery is a type of energy storage system that is frequently employed in our daily lives. It is widely applied in portable devices such as cell phones and laptops, transportation tools such as electrical vehicles, and energy storage power stations. A typical rechargeable battery is composed of positive electrode (cathode), electrolyte and negative electrode (anode). When a rechargeable battery is charged by an output power supply, the provided electrical energy can be transformed into chemical energy which is then stored in the battery. As a result, when the rechargeable battery is connected to an output electrical device, redox reactions spontaneously happen in both cathode and anode to convert the stored chemical energy back into electrical energy.

The first secondary battery in the history is lead-acid battery, which was designed by Gaston Planté in 1859.[3] As shown in Fig. 1a, lead-acid battery is composed of a PbO_2 cathode and Pb anode. H_2SO_4 aqueous solution is used as electrolyte. The overall reaction happening during discharge process is shown below:

$$Pb\ (s) + PbO_2\ (s) + 2\ H_2SO_4\ (aq) \rightarrow 2\ PbSO_4\ (s) + 2\ H_2O\ (l)$$
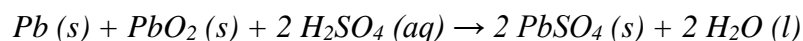
Due to its benefits such as low cost and great safety, lead-acid is still broadly adopted today in battery storage power station; however, low specific energy and toxicity of lead restrict its application in other areas such as portable devices and transportations.[4]
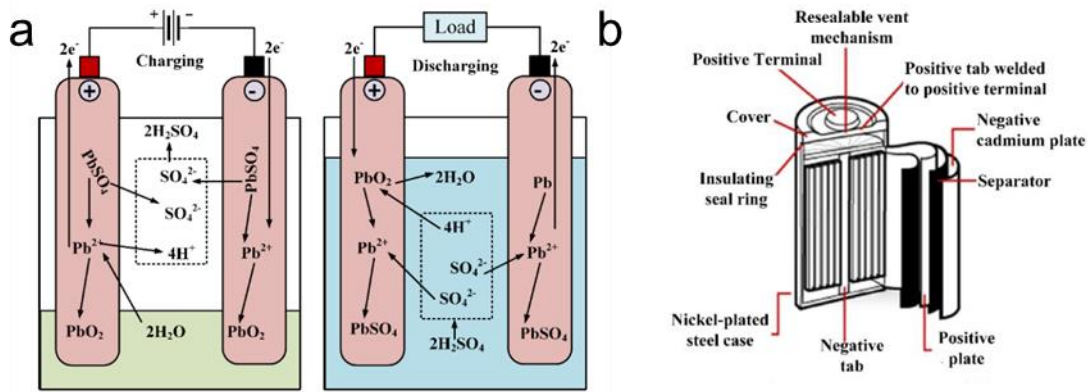
Figure 1. (a) Schematic illustration of lead-acid battery during charge and discharge process.[3] (b) Construction of a sealed nickel-cadmium battery.[3]

Nickel-cadmium (Ni-Cd) battery, as another kind of rechargeable battery, was invented in 1899.[5] Fig. 1b shows the structure of a sealed nickel-cadmium battery. Cd and NiO(OH) are utilized as anode material and cathode material, respectively. KOH is typically used as the alkaline electrolyte. The overall chemical reaction in nickel-cadmium battery is shown as followed:

$$2\ NiO(OH) + Cd + 2H_2O \rightarrow 2\ Ni(OH)_2 + Cd(OH)_2$$
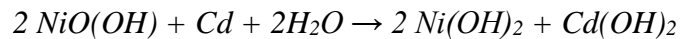
The ability of being charged in a relatively short period of time and low cost makes nickel-cadmium occupy some markets in portable electronics and toys. However, nickel-

cadmium battery can be self-discharged fast when not used, which limits its lifespan. Besides, the relatively low specific energy and the use of hazardous element cadmium severely restrict its applications in the modern society.[3]

As the demand for energy storage continued increasing, other nickel-based secondary batteries, including nickel-metal hydride battery, nickel-iron battery, nickel-zinc battery, and nickel-hydrogen battery, were designed and commercialized.[5] However, each of them has its own shortcomings. For example, nickel-metal hydride battery suffers from low Coulombic efficiency; nickel-iron battery is afflicted with low energy density and low specific power.[5]

Lithium-ion battery (LIB) was invented in 1970s and has been dominating the secondary battery markets for decades because of its superior energy density[6]. Many choices of cathode materials for LIBs have been developed and commercialized, including lithium cobalt oxide ($LiCoO_2$), lithium iron phosphate ($LiFePO_4$), lithium manganese oxide ($LiMn_2O_4$) and lithium nickel manganese cobalt oxide (or NMC).[7] Fig. 2 shows the basic working principle of a typical lithium-ion battery. During discharge process, lithium ions spontaneously migrate from anode to cathode and intercalate into the crystal structure of the cathode materials. When discharged, lithium ions can deintercalate from cathode and intercalate into the anode material. Because of the low reduction potential of lithium (-3.04 V vs. SHE)[8], lithium-ion battery can generally offer a high working voltage and hence benefits the energy density.

3
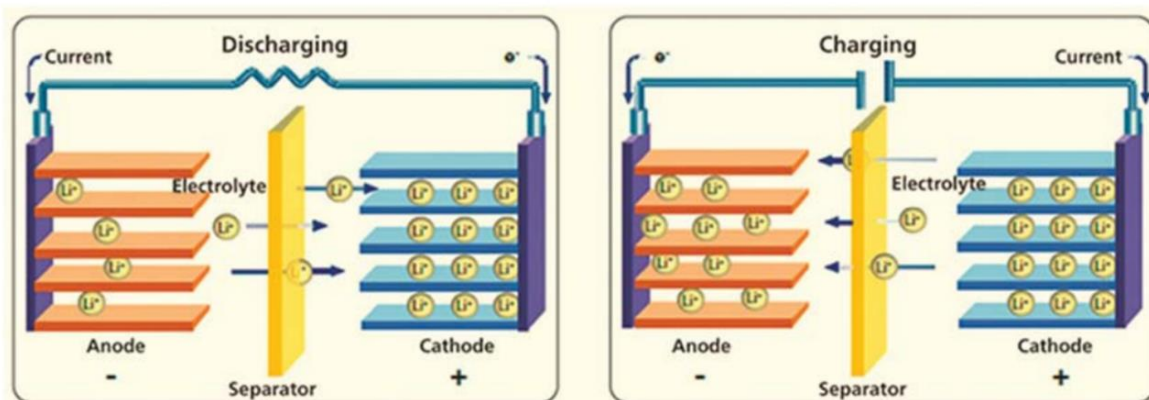
Figure 2. Working theory of a typical lithium-ion battery (LIB).[9]

Even though lithium-ion battery offers superior energy density and remarkable cycle life, it has some limitations. The use of organic flammable electrolyte can cause some safety issues such as explosion. Moreover, the element of lithium is relatively rare in the earth's crust, substitutions of lithium-ion battery need to be developed in the future.

1.2 Aqueous Rechargeable Zinc-ion Batteries

As a possible candidate of the next-generation secondary batteries, aqueous rechargeable zinc-ion battery is increasingly attracting researchers' attention. Table 1 shows the electrochemical characteristics of several charge carriers including Li^+, Na^+, K^+, Mg^{2+}, Ca^{2+}, Zn^{2+}, and Al^{3+}.[10,11] Zinc element is more prevalent in the earth's crust than lithium element, making zinc-ion batteries attractive for large-scale energy storage applications. More importantly, metals such as lithium, sodium, magnesium, and aluminum are active and can react with water or passivate in water; so, they are generally combined with organic electrolytes, which are flammable and can cause safety issues. Zinc metal is compatible with aqueous electrolyte which offers superior safety and ionic conductivities compared with organic

electrolyte. Furthermore, zinc has relatively low reduction potential (-0.76 V vs. SHE), considerable theoretical specific capacity (820 mAhg^{-1}), and remarkable specific volumetric capacity (5855 mAh·cm^{-3}) which provides considerable potential for high energy density batteries.

Table 1. Electrochemical Characteristics of Several Charge Carriers.[10,11]

Charge carrier	Li$^+$	Na$^+$	K$^+$	Mg^{2+}	Ca^{2+}	Zn^{2+}	Al^{3+}
Ionic radius (Å)	0.76	1.02	1.38	0.72	1.00	0.74	0.535
Hydrated radius (Å)	3.82	3.58	3.31	4.28	4.12	4.30	4.75
Theoretical specific capacity (mAhg^{-1})	3861	1166	685	2205	1337	820	2980
Specific volumetric capacity (mAh·cm^{-3})	2046	1131	610	3837	2059	5855	7748
Standard electrode potential (V vs. SHE)	-3.04	-2.71	-2.93	-2.37	-2.87	-0.76	-1.66
Abundance in earth's crust (ppm)	20	23600	20900	23300	41500	70	82300

1.3 Cathode Materials of Aqueous Rechargeable Zinc-ion Batteries

Despite the fact that aqueous rechargeable zinc-ion batteries are promising prospects for future rechargeable batteries, finding appropriate cathode materials which can provide high capacity and stable retention has proven to be one of the most challenging tasks.[11] Throughout the previous decades, Mn-based oxides, vanadium-based oxides, Prussian blue analog-based materials, polymer materials, and Chevrel phase compounds have been considered as promising cathode materials.[10] Fig. 3 shows the working voltage and specific capacity for recently reported electrode materials in Zn-ion batteries.[10] Chevrel phase compounds, Prussian

blue analog-based materials and polymer materials exhibit relatively high working voltages; however, they generally suffer from low specific capacities. Vanadium-based oxides such as vanadium oxides (V_2O_5), sodium vanadium oxides (or NVO), zinc vanadium oxides (or ZVO)
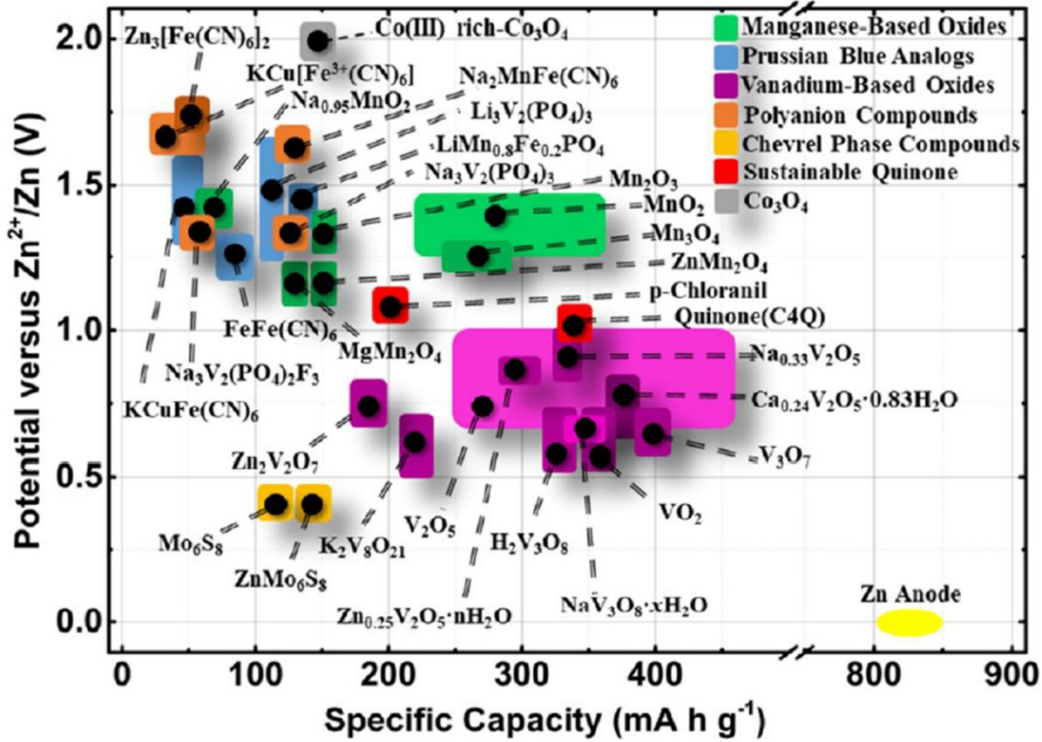
are

Figure 3. working voltage and specific capacity for both Zn anode and recently reported cathode materials.[10]

demonstrated to achieve high specific capacity ranging from ~200 mAhg^{-1} to ~400 mAhg^{-1} and long cycle life.[12] Nevertheless, the toxicity of vanadium element and low working voltage have bring much concern on the future applications.

Manganese-based oxides including manganese oxides (MnO_2, Mn_3O_4, etc.), zinc manganese oxides (or ZMO), sodium manganese oxides (or NMO) are frequently studied

cathode materials in aqueous zinc-ion batteries.[13] The non-toxicity, relatively cheap price, remarkable specific capacity and relatively high working voltages of manganese-based oxides cathode bring significant attention from researchers. Among all manganese-based oxides cathode materials, MnO_2 shows the highest theoretical capacity (308 mAhg^{-1} for 1e$^-$ transfer; 615 mAhg^{-1} for 2e$^-$ transfer).[14]

1.4 Aqueous Rechargeable Zn/MnO$_2$ Batteries

In 1987, Shoji et. al. introduced the first aqueous rechargeable zinc ion battery, which contains Zn anode, γ-MnO_2 cathode, and aqueous $ZnSO_4$ electrolyte.[15] The authors reported that the Zn/ZnSO$_4$/γ-MnO_2 battery obtained 53% of the MnO_2 theoretical capacity (1 e$^-$ transfer), and was rechargeable for more than 30 cycles. This paper provided the basic concept of Zn/ MnO_2 battery. Afterwards, the modification of MnO_2 cathode, Zn anode, and electrolyte has become the focus of scientific research in Zn/MnO$_2$ batteries.

The modifications of MnO_2 cathode include the study on different crystal structures of MnO_2. Table 2 is the previously reported crystallographic data of different MnO_2 minerals[16] and Fig. 4 shows the schematic crystal structures of some tunnel-type and layer-type MnO_2. Generally, tunnel structures or layer structures of MnO_2 are formed with MnO_6 octahedra sharing corners and edges. Hollandite-type MnO_2 (or named α-MnO_2) is made up with 2×2 tunnels; pyrolusite-type MnO_2 (or named β-MnO_2) is a 1×1 tunnel structure; ramsdellite-type MnO_2 (or named R-MnO_2) is composed of 2×1 tunnels; as for γ-MnO_2, it is an intergrowth of β-MnO_2 and R-MnO_2 with different degrees of microtwinning, resulting in both 1×2 tunnels and 1×1 tunnels; differently, birnessite-type MnO_2 (or named δ-MnO_2) was reported to be a

layer structure.[16–18] These various types of MnO$_2$ have been synthesized and electrochemically

tested by researchers, but they generally suffer from a fast capacity fading.[14] Besides, cathode

Table 2. Crystallographic data of different MnO$_2$ minerals.[16]

Compound	Mineral Name	Symmetry Space Group	Lattice Parameters (Å)	Features
α-MnO$_2$	Hollandite	Tetragonal (I4/m)	a=9.96; c=2.85	(2 × 2) tunnel
β-MnO$_2$	Pyrolusite	Tetragonal (P42/mnm)	a=4.39; c=2.87	(1 × 1) tunnel
R-MnO$_2$	Ramsdellite	Orthorhombic (Pbnm)	a=4.53; b=9.27; c=2.87	(1 × 2) tunnel
γ-MnO$_2$	Nsutite	Complex tunnel (hex.)	a=9.65; c=4.43	(1 × 1) / (1 × 2)
δ-MnO$_2$	Birnessite	Rhombohedral (R-3m)	a$_{hex}$=2.94; c$_{hex}$=21.86	(1 × ∞) layer
Na-Bir	Na-birnessite	Monoclinic (C2/m)	a=5.17; b=2.85; c=7.32	(1 × ∞) layer
Mg-Bir	Mg-birnessite	Monoclinic (C2/m)	a=5.18; b=2.84; c=7.33	(1 × ∞) layer
ε-MnO$_2$	Akhtenkite	Hexagonal (P63/mmc)	a=2.85; c=4.65	Dense stack
λ-MnO$_2$	Spinel	Cubic (Fd3m)	a=8.04	(1 × 1) tunnel
ψ-MnO$_2$	Psilomelane	Monoclinic (P2/m)	a=9.56; b=2.88; c=13.85	(2 × 3) tunnel
T-MnO$_2$	Todorokite	Monoclinic (P2/m)	a=9.75; b=2.85; c=9.59	(3 × 3) tunnel

modification methods such as polymer coating[19,20] and carbon-based conductive material

coating[21–23] were applied to help boost the electrochemical performance of Zn/MnO$_2$ batteries.

Methods to adjust electrolyte are mainly divided into cation adjustment such as pre-

adding Mn ions in electrolyte[24], anion adjustment such as bulky anion electrolyte[25], and quasi-

solid electrolyte[26]. It is worth mentioning that pre-adding Mn ions was widely reported as an

effective way to enhance the cyclability of MnO$_2$, but the underneath mechanism is unclear

and controversial[23,27,28]. This will be further discussed in section 1.4.2.
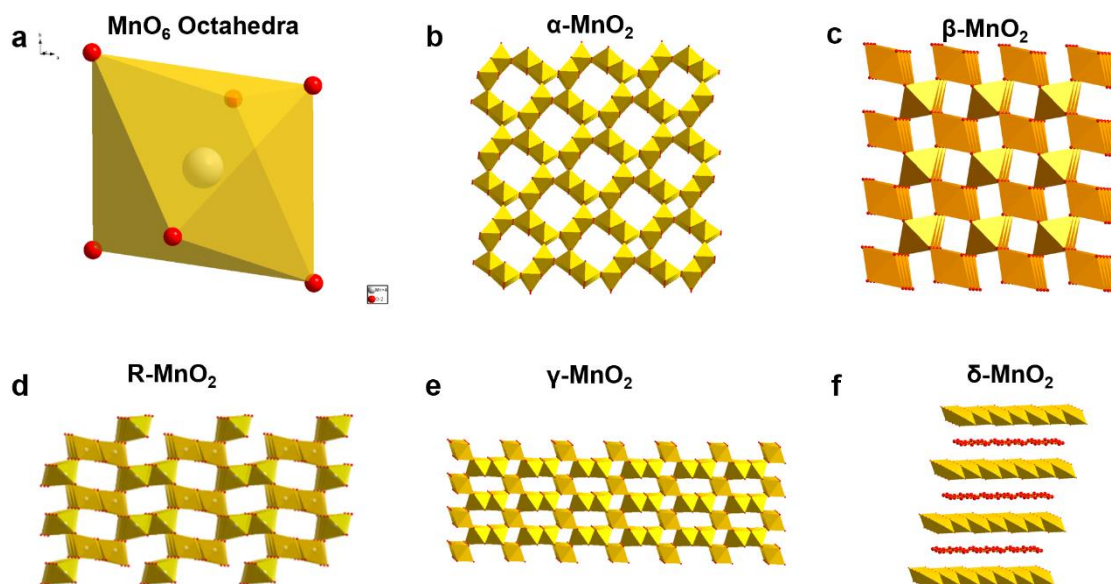
Figure 4. Schematic illustration of crystal structures for (a) MnO₆ octahedra, (b) α-MnO₂, (c) β-MnO₂, (d) R-MnO₂, (e) γ-MnO₂, (f) δ-MnO₂

Work done on Zn anode was primarily focused on solving the issues of dendrite growth. To achieve the goal of commercializing Zn/MnO_2 batteries, the mass of loading active materials in the battery needs to be scaled up. As more cathode materials take part into the electrochemical reactions, it is more difficult to uniformly strip/deposit Zn on the anode. As a result, the growth of Zn dendrite on the anode becomes an urgent issue which needs to be addressed. Many strategies such as coating carbon black on the anode[29] and introducing a fluoride-based artificial interphase on the anode[30] were demonstrated to be useful for achieving relatively uniform zinc stripping/deposition and suppressing the growth of Zn dendrite.

1.4.1 Previously Reported Reaction Mechanisms and Their Limitations

Although rechargeable aqueous Zn/MnO_2 batteries have been researched for many years on cathode, anode and electrolyte, the energy storage mechanism is not fully understood. This phenomenon motivates researchers to investigate on the reaction mechanisms of Zn/MnO_2 batteries these years.

The reaction happening on the Zn anode is shown as followed:

$$Zn \leftrightarrow Zn^{2+} + 2\ e^{-}$$
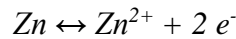
The reaction mechanism for Zn anode is simple and undoubted. Zn metal is reduced into Zn^{2+} ions and released to the electrolyte during discharge process, which is called Zn stripping process. During charge process, cations in the electrolyte are driven to the negative elctrode by the force of electric field; then, Zn^{2+} ions near anode are oxidized and deposited back on the anode.

Nevertheless, the reaction mechanisms for MnO_2 cathode are much more complicated than those for Zn anode. There are three mainstream mechanisms explaining the main cathode reactions of Zn/MnO_2 with mildly acidic $ZnSO_4$ electrolyte.

In 2012, Wei et. al. introduced an intercalation/deintercalation mechanism.[31] Specifically, the authors synthesized α-, β-, γ- and δ-MnO_2 and galvanostatically tested their electrochemical performance. It was found that the specific capacity was independent on surface areas but directly affected by the tunnel sizes or interlayer distances. Hence, the authors believe that the cathode reaction can be explained by Zn intercalation/deintercalation in MnO_2

tunnel structure (α-, β-, γ-MnO$_2$) or layer structure (δ-MnO$_2$). The proposed electrochemical reaction happens on cathode is shown in the following:

$$x\ Zn^{2+} + 2x\ e^- + MnO_2 \leftrightarrow Zn_X MnO_2$$

In 2016, Pan et. al. introduced that the cathode reaction mechanism of Zn/MnO$_2$ battery could be explained by a conversion reaction between manganese dioxide and protons instead of zinc intercalation/deintercalation.[24] The reported high-resolution transmission electron microscopy (HRTEM) and X-ray diffraction (XRD) results demonstrated the formation of a triclinic MnOOH and Zn$_4$(OH)$_6$SO$_4$·xH$_2$O (ZHS) on the cathode after discharge process. Additionally, the lattice fringes of the discharge products on cathode do not match any crystallized Zn$_x$MnO$_2$. Therefore, the cathode reaction mechanisms were revised as followed:

$$H_2O \leftrightarrow H^+ + OH^-$$

$$MnO_2 + H^+ + e^- \leftrightarrow MnOOH$$

$$1/2\ Zn^{2+} + OH^- + 1/6\ ZnSO_4 + x/6\ H_2O \leftrightarrow 1/6\ Zn_4(OH)_6SO_4 \cdot xH_2O$$
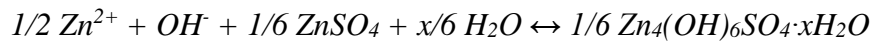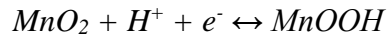
Then, Sun set. al. suggested a more complex H$^+$/Zn^{2+} co-insertion mechanism in 2017.[32] As shown in Fig. 5, their results of galvanostatic intermittent titration technique (GITT) and electrochemical impedance spectroscopy (EIS) proved that the reduction reactions in region I is much more kinetically preferred than those in region II. They therefore deduced that the 1st discharge plateau at relatively high voltage range was conducted by a relatively easy H$^+$ insertion, whereas the 2nd discharge plateau at relatively low voltage ranges was caused by Zn^{2+} insertion.
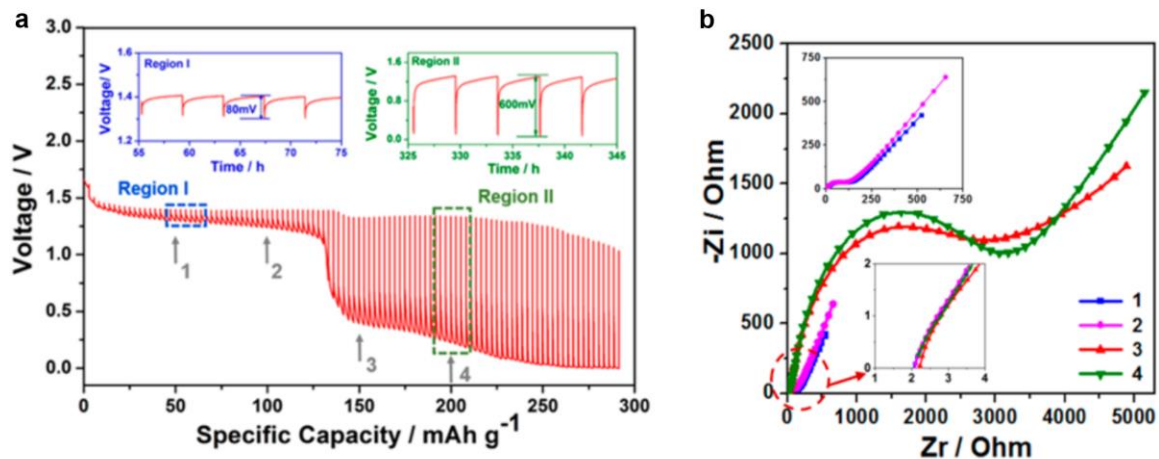
Figure 5. (a) Galvanostatic intermittent titration technique (GITT) result of Zn/MnO₂ battery during discharge process. (b) Electrochemical impedance spectroscopy (EIS) of Zn/MnO₂ battery at selected states (1,2,3,4 referred to Fig. 5a).[32]

Besides the main reactions, side reactions, especially dissolution reactions ($MnO_2 \rightarrow Mn^{2+}$), have been reported to be the key reason for rapid capacity loss in Zn/MnO₂ batteries. Lee et. al. indicated that the generation of $Zn_4(OH)_6SO_4 \cdot xH_2O$ precipitates on cathode was caused by the MnO_2 dissolution which consumed protons in electrolyte.[33] The proposed dissolution reactions are shown below:

$$3\ MnO_2 + 8\ Zn^{2+} + 2\ SO_4^{2-} + 16\ H_2O + 6\ e^- \rightarrow 3\ Mn^{2+} + 2\ Zn_4(OH)_6SO_4 \cdot 5H_2O$$
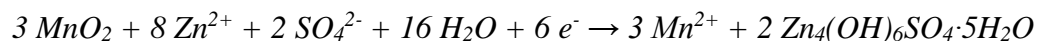
This dissolution reaction has been considered as an irreversible side reaction, and strategies have been developed to inhibit the MnO_2 dissolution such as pre-adding Mn^{2+} ions in electrolyte.[27,34]

However, recent literatures have reported Zn/MnO_2 batteries utilizing dissolution and deposition reactions as main reactions.[35–37] For example, the Zn/MnO_2 battery designed by Qiao's group realized a high specific capacity of 570 mAhg^{-1} that is close to the theoretical capacity based on 2 e$^-$ transfer of MnO_2 (615 mAhg^{-1}).[37] Furthermore, at 30 mA·cm^{-2}, their battery obtained a considerable capacity retention of ~92% after 1800 cycles, which demonstrated the reversibility of the dissolution reaction.

To conclude, even though the cathode reaction mechanism of Zn/MnO_2 battery has been researched for years, and some novel guidance for Zn/MnO_2 battery design has been indicated, there are still some remaining doubts such as the reversibility of the dissolution reaction, and the capacity contributions from intercalation, conversion, and dissolution reactions. Also, although the abovementioned literatures have reported the side products ZHS generated on the cathode surface, negative influences from ZHS are barely discussed. These questions motivate us to further understand the reaction mechanisms and contribute to the future design of Zn/MnO_2 batteries.

1.4.2 Pre-adding Mn ions in Electrolyte and its Limitations

As discussed in section 1.4.1, the dissolution reaction ($MnO_2 \rightarrow Mn^{2+}$) was consider as an irreversible side reaction by many researchers. As a result, pre-adding Mn^{2+} ions in electrolyte has been developed to improve the cyclability of Zn/MnO_2 batteries. Pre-adding Mn^{2+} ions in electrolyte was firstly introduced in 2016.[24] As shown in Fig. 6a, pre-adding 0.1 M $MnSO_4$ in electrolyte dramatically improved the cycling performance and the function of pre-added Mn^{2+} ions was ascribed to be suppressing the dissolution reaction. Similar

improvement was further observed in 2017 (Fig 6b).[27] Instead of $ZnSO_4$ electrolyte system, a bulky anion electrolyte ($Zn(CF_3SO_3)_2$ electrolyte) was utilized and demonstrated to be compatible with pre-added Mn^{2+} ions. However, the authors stated that the mechanism behind pre-addition of Mn^{2+} in electrolyte was yet unknown.
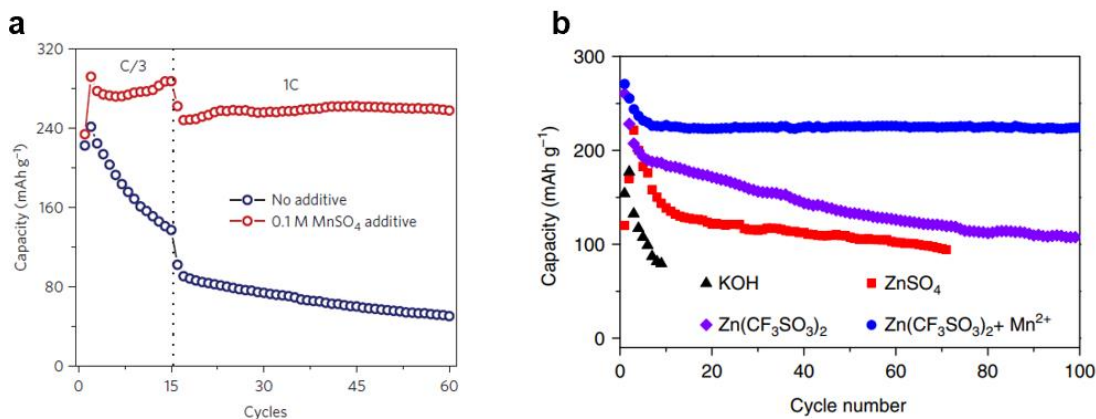
Figure 6. Cyclability of Zn/MnO₂ battery with/without Mn²⁺ additives in (a) ZnSO₄ electrolyte system[24], (b) Zn(CF₃SO₃)₂ system[27].

Since its invention, the Mn^{2+} pre-addition method has been frequently applied in subsequent scientific studies. Table 3 organizes the reported Zn/MnO_2 batteries with their maximum capacity and cycling performance during 2017-2021. Pre-addition of Mn^{2+} ions to the electrolyte, as established in these papers, is an effective strategy for boosting cycling performance, but the principle behind it have been contentious since they were presented. For instance, in 2020, Qiu et. al. assembled $Zn/\delta-MnO_2$ batteries with $MnSO_4$ additives in electrolyte and studied the phase evolution of MnO_2 cathode during cycling.[38] From their experimental results, the pre-added Mn^{2+} can be continually oxidized onto cathode and

14

generate ε-MnO$_2$ when the battery is charged, which is the reason for capacity improvement. To conclude, the authors believe that the addition of Mn^{2+} cannot stabilize the MnO$_2$ cathode,

Table 3. Recently reported Zn/MnO$_2$ batteries with their maximum capacity and cycling performance. (Note: CNT stands for carbon nano tube; N-CNSs stands for nitrogen-doped carbon nanosheets; CNF stands for carbon nano fiber; V$_o$ stands for oxygen-defected)

Cathode	Electrolyte	Maximum Capacity (mAhg^{-1})	Capacity Retention and Corresponding Current Density	Reference
MnO$_2$/gelatin	2 M ZnSO$_4$ + 0.2 M MnSO$_4$	415	90% after 1000 cycles; 0.5 Ag^{-1}	14
β-MnO$_2$/C	3 M Zn(CF$_3$SO$_3$)$_2$ + 0.1 M MnSO$_4$	150	100% after 400 cycles; 0.3 Ag^{-1}	22
MnO$_2$/polypyrrole	2 M ZnSO$_4$ + 0.1 M MnSO$_4$	256	100% after 500 cycles; 1 Ag^{-1}	34
MnO$_2$/CNT/PEDOT	2 M ZnCl$_2$ + 0.4 M MnSO$_4$	290	77% after 500 cycles; 5.4 Ag^{-1}	39
MnO$_2$/polyfurfural	1 M Zn(CF$_3$SO$_3$)$_2$ + 0.2 M MnSO$_4$	500	99% after 160 cycles; 0.5 Ag^{-1}	40
β-MnO$_2$	3 M ZnSO$_4$ + 0.2 M MnSO$_4$	288	91% after 200 cycles; 0.5 C	41
α-MnO$_2$/graphene	2 M ZnSO$_4$ + 0.2 M MnSO$_4$	382	94% after 3000 cycles; 3 Ag^{-1}	42
MnO$_2$/N-CNSs	2 M ZnSO$_4$ + 0.2 M MnSO$_4$	304	92% after 1800 cycles; 2 Ag^{-1}	43
MnO$_2$/CNF	2 M ZnSO$_4$ + 0.1 M MnSO$_4$	297	100% after 2750 cycles; 3 Ag^{-1}	44
V$_o$-MnO$_2$	2 M ZnSO$_4$ + 0.1 M MnSO$_4$	314	81% after 1000 cycles; 5 Ag^{-1}	45
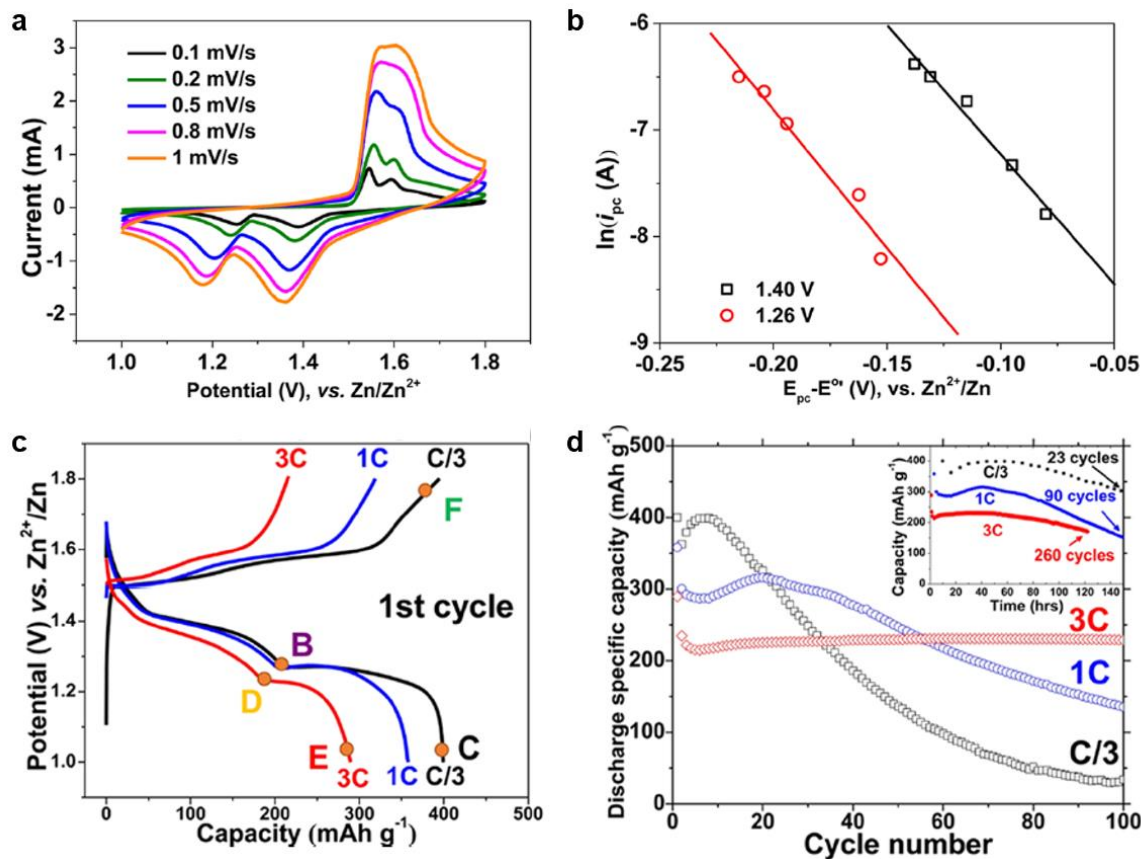
Figure 7. (a) Cyclic voltammetry (CV) results. (b) Corresponding plot of ln(i_{pc}) versus ($E_{pc} - E^{o'}$). (c) Galvanostatic charge/discharge profile at different current density. (d) Corresponding cycling performance.[46]

and the improved cyclability is from the consumption of additional Mn^{2+} ions in electrolyte. Similar statements can be found in other literatures.[47,48] As many researches were conducted in coin cells where the MnO_2 mass loading is relative low and the electrolyte is excess, the additional capacity from deposition of Mn^{2+} additive can be high enough to hinder the realistic electrochemical performance of MnO_2 cathode. Therefore, the functioning theory of Mn^{2+}

16

additives needs to be further inspected and other strategies should be developed for the future application of Zn/MnO_2 batteries.

Also, it is worth mentioning that although Mn^{2+} additives can improve the cycling performance at relatively high current densities, few literatures reported outstanding performance under low current densities. To address this question, Yang's group compared the electrochemical performance of Zn/MnO_2 batteries at different current densities.[46] According to their galvanostatic tests and cyclic voltammetry (CV) results (as shown in Fig. 7), the 1st discharge plateau (at ~1.4 V) was more kinetically favorable than the 2nd discharge plateau (at ~1.26V); as a result, when the current density increased, the 1st discharge plateau was barely affected, but the 2nd discharge plateau was shorten significantly. With a decrease of kinetically unfavorable reaction, the battery can achieve a relatively high reversibility. However, it is well known that commercial batteries such as lithium-ion batteries used in practical scenario are generally discharged at a low current density for continuous energy supply. So, for the future commercialization of Zn/MnO_2 batteries, reversibility at low current densities needs to be improved.

To conclude, although pre-adding Mn^{2+} in electrolyte can help enhance the cycling performance, their functioning theory is still controversial. Insignificant improvement of battery lifespan at low current density is also a limitation of pre-adding Mn^{2+} in electrolyte. To achieve high reversibility of Zn/MnO_2 at a relatively low current density remains a challenging and important task.

Chapter 2: Characterization Techniques

2.1 Material Characterization Techniques

In this section, Material characterization techniques involving scanning electron microscopy (SEM), low-resolution and high-resolution transmission electron microscopy (TEM), energy-dispersive X-ray spectroscopy (EDS), X-ray diffraction spectroscopy (XRD), Fourier transform infrared spectroscopy (FT-IR), inductively coupled plasma mass spectroscopy (ICP-MS) will be discussed regarding to their functioning principle and specific models.

2.1.1 Scanning Electron Microscopy (SEM)

The invention of the first scanning electron microscope can be traced back to 1938.[49] Increasing the resolution of microscopes was the goal of developing electron microscopes.[50] The wavelength of visible light limits the resolution of optical microscopy; specifically, the resolution limit of optical microscopes is half of the visible light wavelength (~2000 Å).[51] However, the wavelength of an accelerated electron is dependent on its speed which can be theoretically close to the velocity of light.[50] The relationship between the accelerating voltage and corresponding electron wavelength is shown in Table 4.[50] If the applied voltage is high enough, the wavelength of the accelerated electron can be much smaller than that of visible light (400-800 nm), and the obtained resolution can be much higher than the conventional optical microscope. Therefore, SEM has received extensive attention from scientists and was finally commercialized in 1996.[49]

Table 4. The relationship between applied voltage, velocity of accelerated electrons and wavelength of accelerated electrons.[50]

Accelerating Voltage/kV	Velocity of Electrons/ms^{-1}	Ratio of Electron Velocity to Light Velocity	Wavelength of electrons/pm
10	5.83×10^7	0.194	12.20
100	1.64×10^8	0.548	3.70
200	2.08×10^8	0.695	2.51
500	2.59×10^8	0.863	1.42
1000	2.83×10^8	0.941	0.87
3000	2.97×10^8	0.989	0.36

The basic construction of a scanning electron microscope is shown in Fig. 8a. Generally, an SEM is constructed with a high-voltage electron gun, magnetic lens series, a sample stage in high vacuum circumstance, detectors, and imaging systems.[52] The high-velocity electron sources are generated by the electron gun which is combined with accelerating fields; when the generated electrons pass through the lens systems, electron beams can be formed and sharpened; then, the incident electron beams can interact with the atoms of the specimen, and the interaction signals are collected by the detector which are further analyzed by the imaging systems (the interaction process requires high vacuum circumstance to avoid unnecessary interactions with air).[53]

To be specific, the interaction between specimen atoms and the incident primary electrons can generate different signals, including backscattered electrons (BSE), secondary

electrons (SE), characteristic X-ray, as well as Auger electron (as shown in Fig. 8b).[53] Different
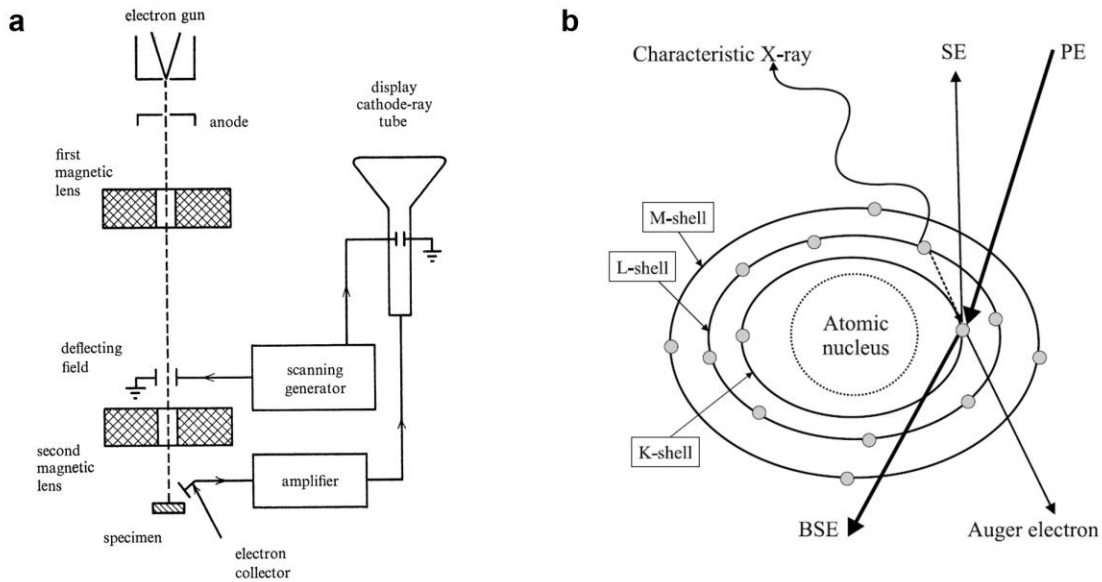
Figure 8. (a) Schematic construction of a scanning electron microscope.[53] (b) Interaction between the incident primary electrons and the specimen atoms.[52]

generated electrons give different information of the sample. Secondary electron (SE) are valence electrons getting away from the surface of the atoms, and they can give the information of the sample surface.[52] Backscattered electrons (BSE) are generated by the reflection of the sample atom, which is a type of elastic interaction; these electrons can give sample details on element distribution.[54] Another type of commonly used information is from the characteristic X-ray; this information is collected by an energy-dispersive spectroscopy (EDS) and can quantitatively show the amount and distribution of various elements on the detected samples, which will be further discussed in section 2.1.3.[52]
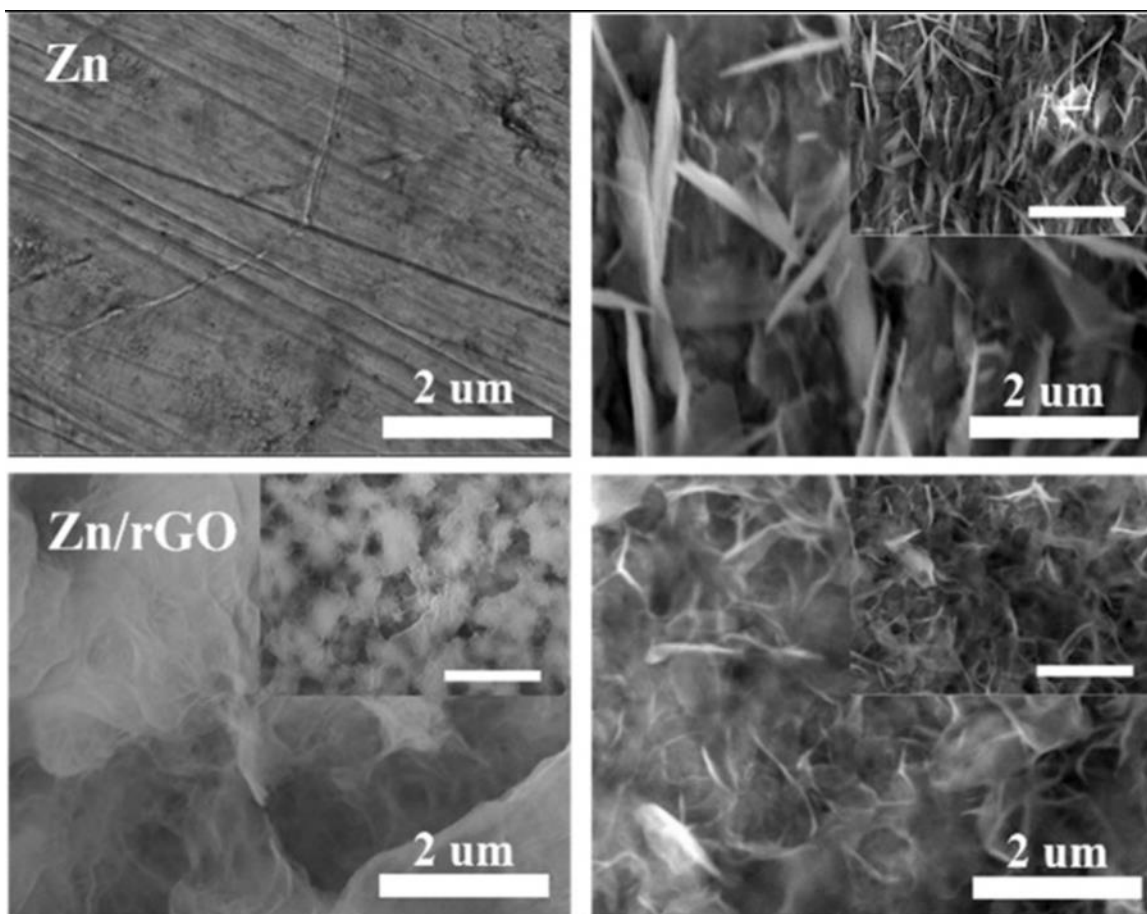
Figure 9. An example of SEM images in aqueous zinc ion batteries.[55]

Fig. 9 gives an example of SEM images applied in aqueous zinc ion batteries. Since SEM is a technique which can be used to observe sample morphologies on nano-scale, it is frequently used in battery research to detect morphology evolution (both cathode material and anode material) during cycling. In this thesis, morphology of electrode materials are characterized by field emission scanning electron microscopy (FESEM, Zeiss LEO 1530).

2.1.2 Transmission Electron Microscopy (TEM)

Different from scanning electron microscope, transmission electron microscope collects sample information by electrons transmitted through the sample, which therefore requires a higher accelerating voltage and thinner specimen than those of scanning electron microscope.[56] Fig. 10 shows the basic components of a transmission electron microscope. TEM and SEM are mainly differed on their lens systems. As discussed in previous section, the lens

Electron gun
Filament
Gun lens/accelerator

Condenser lens 1

Condenser lens 2
Condenser Aperture

EDX

Probe Cs corrector

Condenser mini-lens

Computer

x-tilt
y-tilt

XY Scan coils/deflectors
Objective prefield
Sample Holder
Objective lens
Objective Aperture
Selected Area Aperture
Intermediate lens
Bi-prism
Projector lens

Screen

ADF detector
Imaging Filter
CCD camera

Figure 10. The basic components of a transmission electron microscope.[56]

systems in SEM are used for generating and sharpening the electron beams which further interact with the specimen; however, in TEM, several lens systems can also be found below

the sample stage, which is for further magnifying the electrons transmitted through the sample.[56] With a higher accelerating voltage, the wavelengths of the electron beams in TEM can be lower than those in SEM. Also, the electron beams can transmit through the prepared thin sample, which provides information for the inner structure of the specimen.[56] Therefore, in the case of studying inner structure of materials, TEM exhibits better applications than SEM.
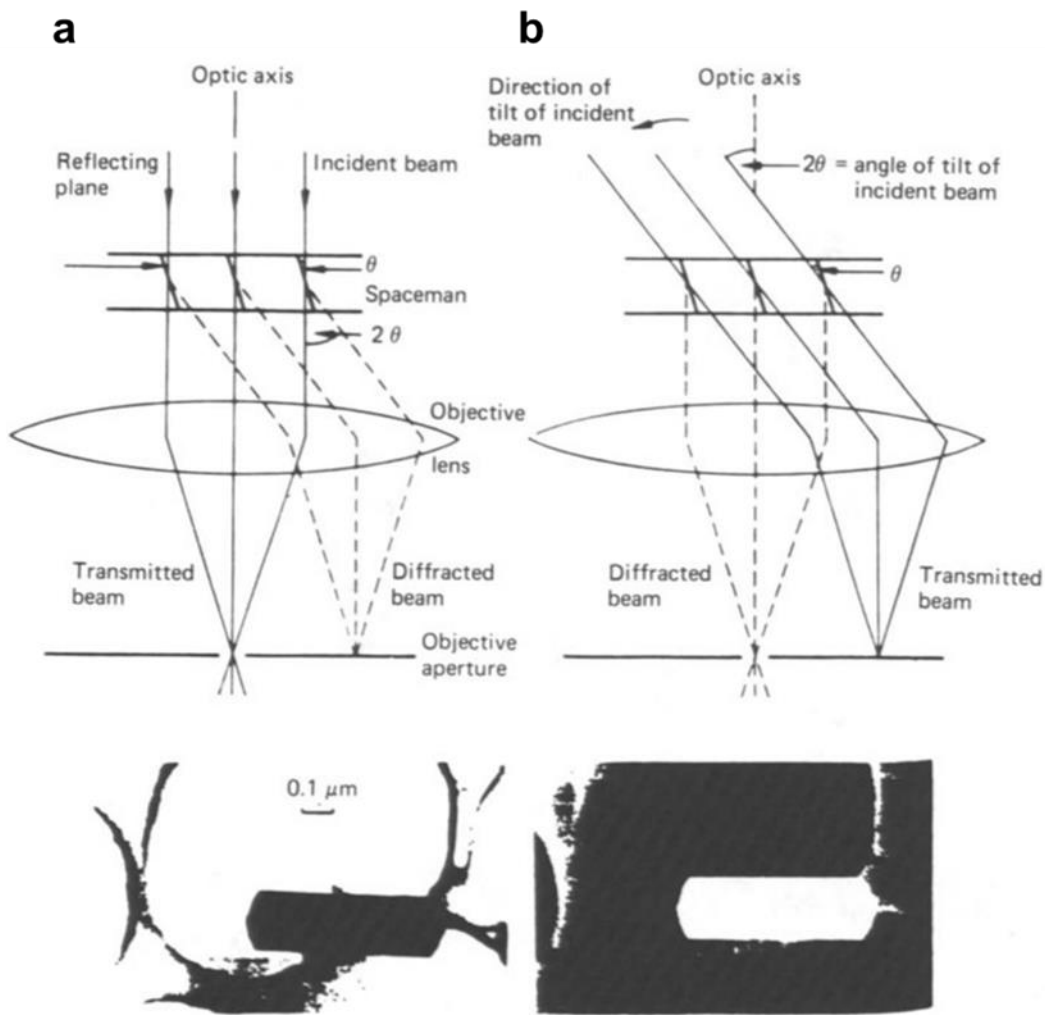
Figure 11. (a) Bright-field imaging method and its corresponding image. (b) Dark-field imaging and its corresponding image.

Depending on different settings of the imaging system, bright-field image, dark-field image, and high-resolution image can be obtained. Fig. 11a and Fig. 11b shows the working principle of bright-field imaging and dark-field imaging as well as their corresponding formed images. The aperture is adjusted in bright-field imaging to only let in transmitted beams; so, the backdrop is bright, and the specimen region is dark.[57] Dark-field imaging, on the other hand, is achieved by only permitting diffracted beams to pass through; as a result, the backdrop is dark, and the specimen region is light.[57] In addition, combining the diffracted and the transmitted beams to capture phase interference yields a high-resolution picture, which is a helpful approach for studying crystal structures.[57]
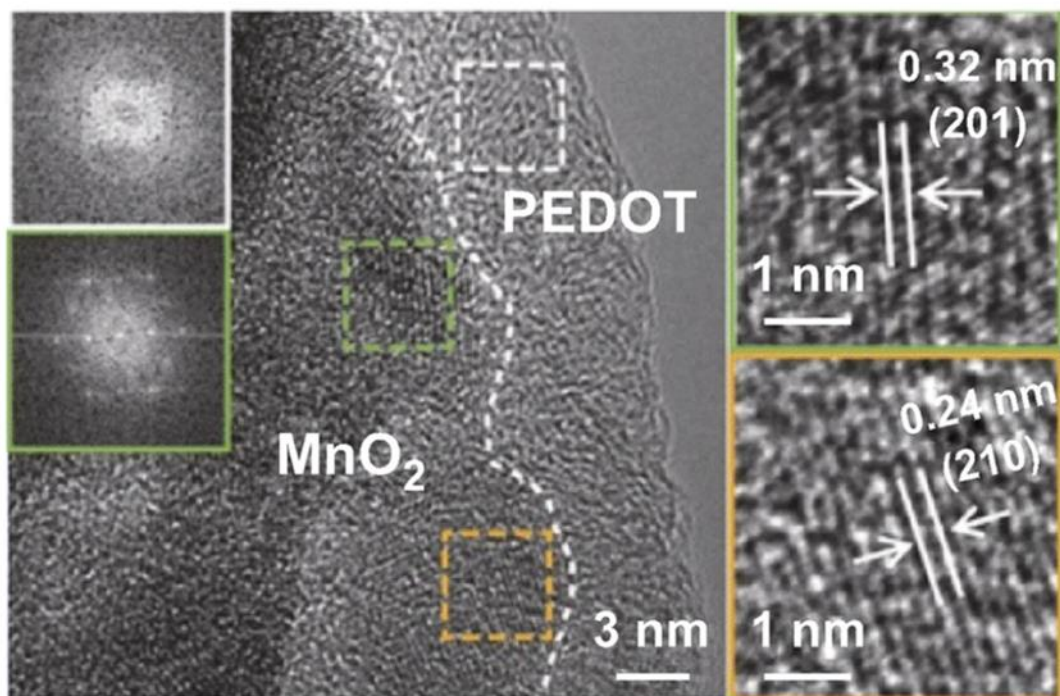
Figure 12. An example of the application of high-resolution transmission electron microscopy in aqueous zinc ion battery.[58]

Fig. 12 gives an instance for the application of high-resolution transmission electron microscopy (HRTEM) in aqueous zinc ion battery. Typically, the lattice fringes showing phase information can be obtained by HRTEM, which is useful for determining the crystal structures of the observed materials. Moreover, even amorphous materials can be detected by HRTEM technique, which will show as disordered region.[24]

In this thesis, the type of transmission electron microscopy used is JEM-F200 under 200 kV accelerating voltage.

2.1.3 Energy-dispersive X-ray Spectroscopy (EDS)

As discussed in previous sections, the high-velocity electron beams used in SEM and TEM can interact with the specimen atoms and generate characteristic X-ray. This process is accomplished by two steps. Firstly, the incident electron beams have high enough energy to excite the specimen electrons in their inner shell (K shell or L shell); then, the excitation leads to residual holes in the inner shell, which can be further filled by electrons from higher energy level combining with an X-ray emission.[59] Hence, the emitted X-ray contains information of
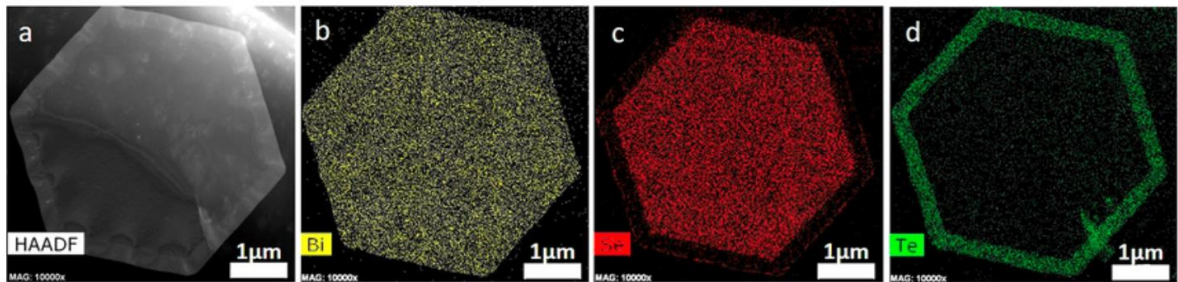
Figure 13. An example of EDS mapping combined with TEM technique.[60]

25

the sample atoms, which can be collected and analyzed to show the amount of elements on the

sample materials and their distribution.[59] This technique is commonly used with SEM and

TEM, to determine the elements distribution and contribution in a selected area. Fig. 13 shows

an example of EDS mapping result combined with TEM.

In this thesis, the type of used EDS facility is JED2300T.

2.1.4 X-ray Diffraction Spectroscopy (XRD)

X-ray diffraction spectroscopy (XRD) is a widely used technique for determining

crystal structure of materials. The operating principle of XRD is based on Bragg's law. Fig. 14

shows the schematic illustration of Bragg's law. Basically, the incident X-ray has an included

angle θ with sample lattice planes. In most cases, the incident X-ray gets scattered by the lattice

planes, and the scattered X-rays have different phases which make the total interference near

zero. The critical case occurs when the wavelength, distance between lattice planes, and the
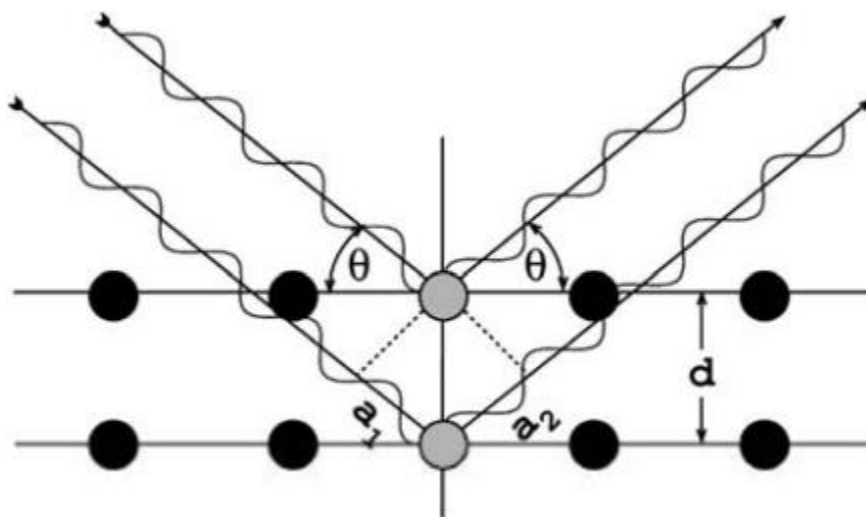
Figure 14. Schematic illustration of Bragg's law.[61]

incident angle have the following relationship:

$$n\,\lambda = 2\,d\,sin\theta$$

(Note: n is an integer, λ stands for the wavelength of the incident X-ray, d is the distance between lattice planes, θ is the incident angle.)
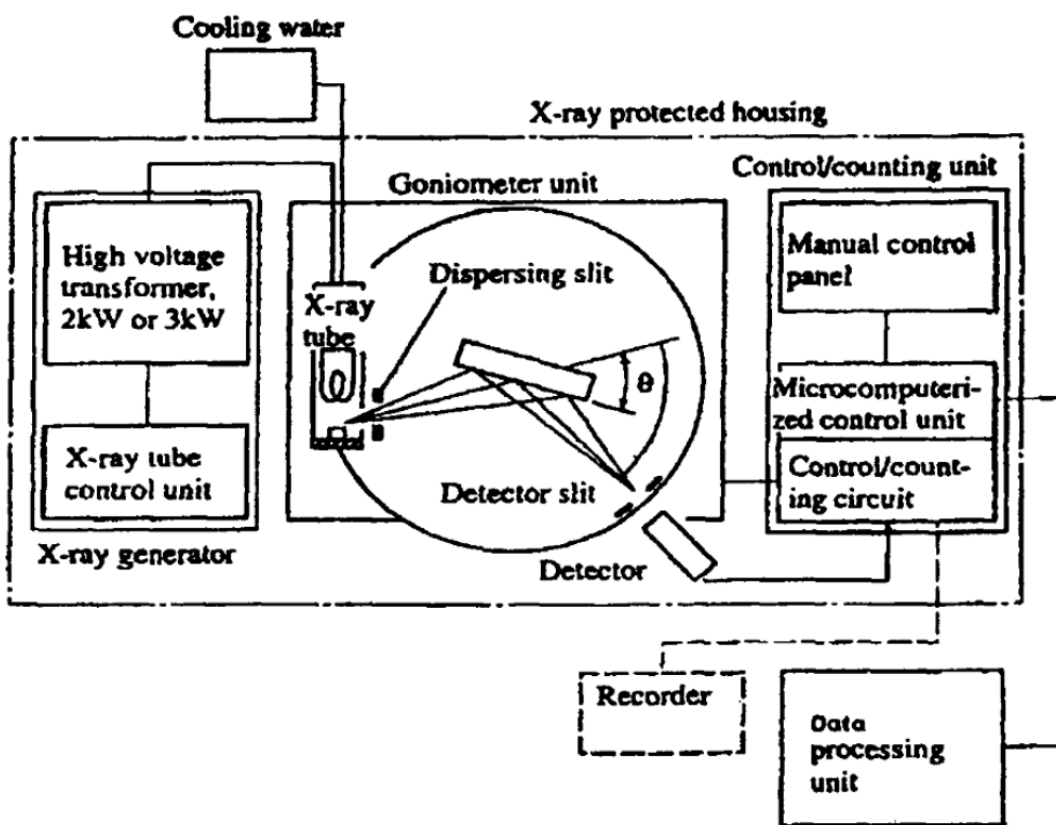
Figure 15. The basic components of an XRD facility.[62]

In this special case, the scattered X-rays have the same phase, resulting in a constructive interference which shows distinctive intensity of scattered X-rays in XRD spectrum.[61] So, by

detecting the intensity of the scattered X-rays and their corresponding angles, researchers can obtain the information of material crystal structures.

Fig. 15 shows the basic constructions of an XRD facility.[62] The X-ray is formed by the X-ray generator, where a high voltage is applied to accelerate electrons and a copper target is designed to be hit and generate X-rays. The X-ray tube is connected by a chiller to cool down the equipment which is heated by the X-ray generation process. Dispersing slits and detector slits are designed for reducing the scanning area and decreasing influences from sample holders. X-ray detectors are connected with a counting unit to collect and analyze the scattered X-rays.

In this thesis, Brüker D8 Discover with Cu Kα radiation ($\lambda = 1.54$ Å) is used to study the phase of cathode materials.

2.1.5 Fourier Transform Infrared Spectroscopy (FT-IR)

Fourier transform infrared spectroscopy (FT-IR) is a frequently employed technique for studying the functional groups of sample materials. Fig. 16 shows the schematic process from emitting light to achieving spectrum data. Basically, FT-IR facility can emit light with different wavelength in the infrared range, and the light at specific wavelength can be absorbed by the sample materials for energy level transition. Specifically, electrons in sample molecules can be excited to higher energy levels via rotational transition and vibrational transition by absorbing the energy (equivalent to the energy distance between transited energy level and original energy level) supplied by the incident light. Hence, by collecting the transmittance and the corresponding wavelength, information of the sample molecule energy level can be obtained.[63,64]

28
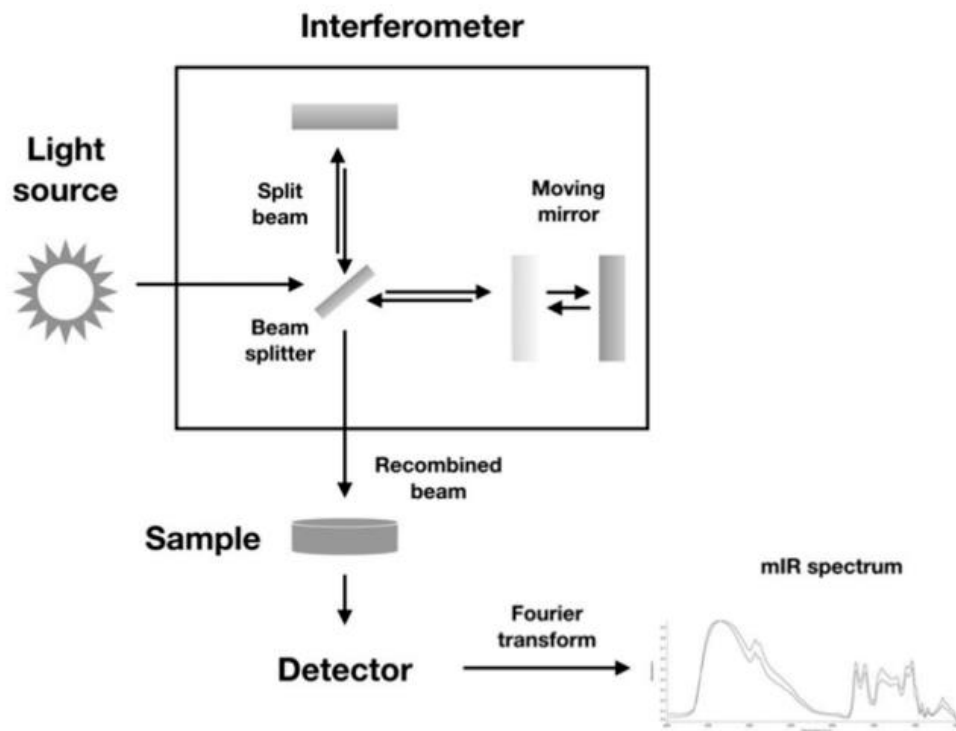
Figure 16. Schematic process of obtaining a FT-IR spectrum.[64]

In this study, Brüker Optics Vertex 70 Spectrometer with the wavelength range from 400 cm^{-1} to 4000 cm^{-1} is used to investigate the functional groups of the ion exchange resin.

2.1.6 Inductively Coupled Plasma Mass Spectrometry (ICP-MS)

Inductively coupled plasma mass spectrometry (ICP-MS) is usually utilized to determine the concentration/amount of metal elements in sample materials. As shown in Fig. 17, the major components of ICP-MS include the sample delivery device, inductively coupled plasma, interface region, ion lens system, mass filter, as well as the detector. The introduced sample needs to be in liquid phase. Therefore, solid sample needs to experience a digestion

process, a filtration process, and a dilution process if necessary. Generally, the solid sample is
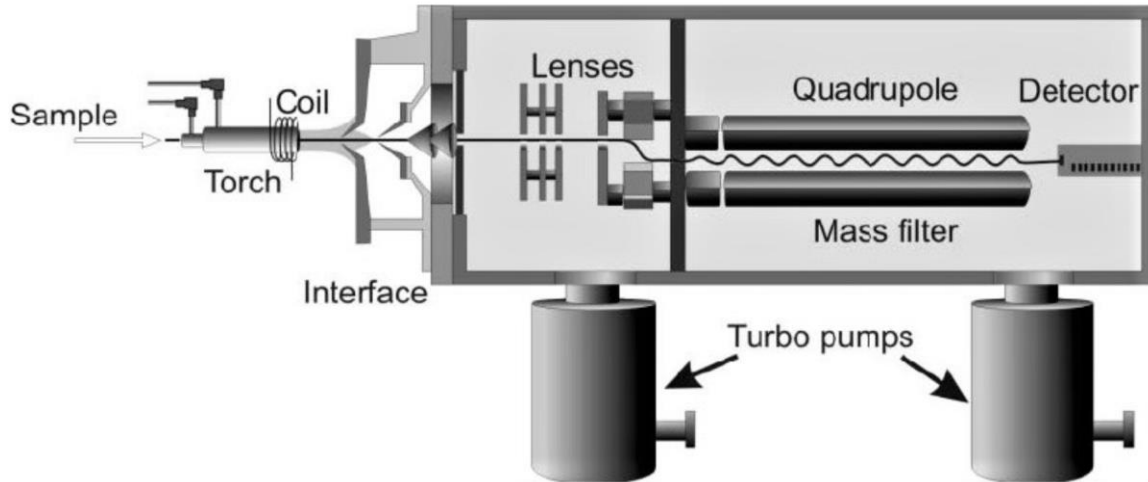
Figure 17. Fundamental components of an ICP-MS facility.[65]

digested by nitric acid, filtered, and diluted to attain an acidic solution with trace metal ion concentration. The liquid sample is then introduced the ICP-MS equipment, turns into an aerosol, which is further ionized by the argon plasma with high-temperature. Afterwards, the generated ions transform through the interface, focused by the ion lens system, and filtered by the mass-charge ratio. The detector collects the ions and eventually calculates the amount/concentration of the sample ions.[65]

2.2 Electrochemical Characterization Techniques

In this section, electrochemical characterization techniques including galvanostatic battery test and electrochemical impedance spectroscopy will be discussed regarding to their principles and facility specifications.

2.2.1 Galvanostatic Test

Before the introduction of galvanostatic test, several definitions of rechargeable batteries will be discussed firstly.

Specific capacity of the cathode/anode in a rechargeable battery is in the unit of Ahg^{-1}, which is defined as the current that a unit mass of cathode/anode material can deliver/store over a unit of time.

Open circuit voltage stands for the voltage of a rechargeable battery when the output circuit is disconnected.

Working/operating voltage is defined as the average voltage when the battery is connected to an output circuit.

Cycling performance is often judged by the cycle number and capacity retention. The capacity retention can be calculated as following formula:

capacity retention = capacity after specific cycles/ maximum capacity

for example, if a rechargeable battery has a maximum specific capacity of 1 Ahg^{-1}; after 300 cycles, the battery still has a specific capacity of 0.8 Ahg^{-1}. Then, it can be defined that the battery has 80% capacity retention after 300 cycles.

All above discussed parameters can be determined by a battery tester. There are two general charge/discharge modes for battery testing: potentialstatic mode and galvanostatic mode. Potentialstatic mode means that the battery is cycled by a constant voltage; galvanostatic mode means that the battery is cycled by a constant current.

Figure 18. A picture of Neware battery tester.[66]

In this study, Zn/MnO$_2$ batteries are tested by a Neware tester (BTS4000-5V, Fig. 18) via galvanostatic mode. Depending on different batteries involved, the electrochemical window is set as 1 V – 1.9 V and 1 V – 1.95 V.

2.2.2 Electrochemical Impedance Spectroscopy (EIS)

Electrochemical impedance spectroscopy is a common strategy to measure different types of impedance in rechargeable batteries, such as electrolyte/electrode resistance R$_\Omega$, charge-transfer resistance R$_{ct}$, double-layer capacitance C$_d$, and Warburg impedance Z$_w$. Basically. When an alternating current (AC) is applied to a rechargeable battery, the total impedance of the battery is a complex number including its real part Z$_{Re}$ and its imaginary part
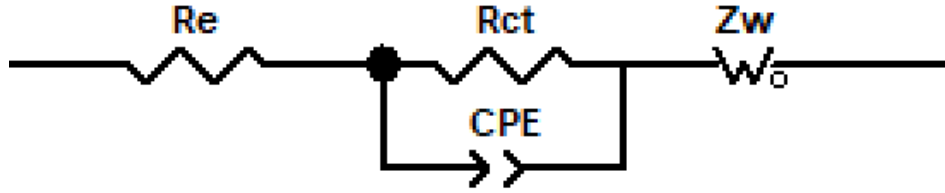
Figure 19. A general equivalent circuit of a rechargeable battery.

Z_{Im}. For a general circuit (Fig. 19), the impedance Z_{Re} and Z_{Im} can be expressed by the following formulas:

$$Z_{Re} = R_\Omega + \frac{Rct + \sigma\omega^{-1/2}}{(C_d\sigma\omega^{1/2} + 1)^2 + \omega^2C_d^2(Rct + \sigma\omega^{-1/2})^2}$$

$$Z_{Im} = \frac{\omega C_d(Rct + \sigma\omega^{-1/2})^2 + \sigma\omega^{-1/2}(\omega^{1/2}C_d\sigma + 1)}{(C_d\sigma\omega^{1/2} + 1)^2 + \omega^2C_d^2(Rct + \sigma\omega^{-1/2})^2}$$

(Note: ω is frequency; σ is mass-transfer coefficient.)

When the applied AC has low frequency ($\omega\rightarrow0$), the relationship between Z_{Re} and Z_{Im} can be simplified as followed:

$$Z_{Im} = Z_{Re} - R_\Omega - R_{ct} + 2\sigma^2C_d$$

Therefore, the Nyquist plot (Z_{Im} vs. Z_{Re}) will be a straight line with the slope of 1, as shown in Fig. 20a.

On the other hand, when the applied frequency is high enough ($\omega\rightarrow\infty$), the relationship between Z_{Re} and Z_{Im} can be simplified as followed:

$$(Z_{Re} - R_\Omega - R_{ct}/2)^2 + Z_{Im}^2 = (Rct/2)^2$$

33

The corresponding Nyquist plot will be a half-circle with its center on $R_\Omega + R_{ct}/2$ and radius of Rct/2, as shown in Fig. 20b.
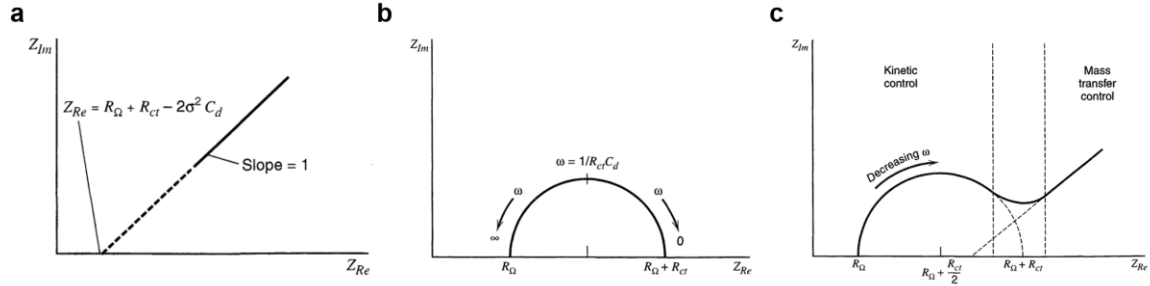
Figure 20. Nyquist plots of electrochemical system (such as batteries) (a) at low frequencies, (b) at high frequencies, (c) containing both low frequencies and high frequencies.[67]

When the applied AC ranges from low frequencies to high frequencies, the Nyquist plot will show as a half-circle with a linear tail, as shown in Fig. 20c. As a conclusion, by fitting the data points via an equivalent circuit, researchers can obtain the values of different types of impedances.[67]

In this work, EIS is performed via a Bio-Logic VMP3 electrochemical workstation with frequencies ranging from 100 mHz to 1 MHz.

Chapter 3: Revised Energy Storage Mechanisms and Capacity Fading Mechanisms in Zn/β-MnO₂ Batteries

In Chapter 3, a series experiments including electrochemical tests and characterization results will be discussed. Based on the experimental results, revised energy storage mechanisms and capacity fading mechanisms in Zn/β-MnO₂ are proposed.

3.1 Fabrication of Zn/β-MnO₂ Batteries and Zn/Zn₄(OH)₆SO₄·5H₂O Batteries

This section mainly introduces the fabrication method of Zn/β-MnO₂ batteries as well as Zn/Zn₄(OH)₆SO₄·5H₂O batteries used in this thesis, including the synthesis of β-MnO₂, synthesis of Zn₄(OH)₆SO₄·5H₂O, recipe for cathode fabrication, and coin cell assembling method.

3.1.1 Synthesis of β-MnO₂

β-MnO₂ nanowires are synthesized by a simple chemical redox reaction. Specifically, 1.69 g MnSO₄·H₂O (≥ 99%, Sigma-Aldrich) and 0.8 g NaOH (≥ 97%, Sigma-Aldrich) are dissolved into 200 mL deionized H₂O and 50 mL deionized H₂O, respectively. Both solutions are stirred until the solutions are clear. Afterwards, 1 mL 30wt% H₂O₂ (30wt% in H₂O, Sigma-Aldrich) is transferred to the NaOH solution, which is further stirred for 1 min. Subsequently, the mixture of H₂O₂ and NaOH solutions are slowly added into the MnSO₄ solution. The mixed solution is continuously stirred for 24 h. After the magnetic stirring, the precipitates are collected by centrifuge process and washed with deionized H₂O three times. The obtained

precipitates are dried at 80°C for 12 h and manually ground to powders. Then, the powders are calcinated in oven with air atmosphere at 250°C for 6 h. The reaction equation is shown below:

$$MnSO_4 + H_2O_2 + 2NaOH \rightarrow MnO_2 \downarrow + Na_2SO_4 + 2H_2O$$
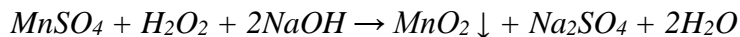
3.1.2 Synthesis of $Zn_4(OH)_6SO_4 \cdot 5H_2O$

$Zn_4(OH)_6SO_4 \cdot 5H_2O$ is simply synthesized by a chemical reaction refer to the previous literature[68]. Specifically, 1.44 g $ZnSO_4 \cdot 7H_2O$ ($\geq$ 98%, Alfa Aesar) are dissolved in 50 mL deionized H_2O, and 0.3 g NaOH ($\geq$ 97%, Sigma-Aldrich) are dissolved in 50 mL deionized H_2O. Both solutions are magnetically stirred until clear. Afterwards, the $ZnSO_4$ solution is slowly added into the NaOH solution. After 1 h magnetic stirring, the milky precipitates is filtered, washed with deionized H2O three times, and dried at 80°C for 12 h.

3.1.3 Cathode Fabrication and Coin Cell Assembling

The cathode fabrication is accomplished by mixing the active material (β-MnO_2 or $Zn_4(OH)_6SO_4 \cdot 5H_2O$) with conductive material and binder, coating the mixed slush on a current collector, drying under vacuum, and cutting into small disc which fits our coin cell. To be specific, a slurry composed of 70wt% β-MnO_2 (or $Zn_4(OH)_6SO_4 \cdot 5H_2O$), 20wt% acetylene black (MTI), 10wt% PVDF in NMP ($\geq$ 99.5%, Sigma-Aldrich) solvent is uniformly coated on conductive PE film (All-Spec) by doctor blade and dried at 60°C under vacuum for 12 h. The PE film with active material coating is then cut into discs with diameter of 12 mm for battery assembling. The active material mass loading for β-MnO_2 cathode is around 2.5 mg, and the active material mass loading for β-MnO_2 cathode is around 4 mg.

Then, CR2032 coin cells are assembled with cathode discs, 2 layers of absorbed glass mat (diameter: 12 mm, thickness: 0.5 mm, NSG corporation) as separator, and polished zinc (diameter: 12mm, thickness: 0.2mm, Rotometals) as anode. 115 μL of 2 M $ZnSO_4$, 2 M $ZnSO_4$ + 0.1 M $MnSO_4$, and 2 M $ZnSO_4$ + 0.2 M $MnSO_4$ are utilized as electrolyte in different cases.

3.2 Material Characterization and Electrochemical Performance of Zn/β-MnO₂ Batteries and Zn/Zn₄(OH)₆SO₄·5H₂O Batteries

In this section, material characterization methods involving ex-situ XRD, SEM, TEM, ICP-MS, and electrochemical testes are performed to investigate the energy storage mechanisms in Zn/β-MnO_2 batteries.

3.2.1 Characterization of the Synthesized MnO₂

Powder XRD, HRTEM and SEM are conducted to determine the phase and morphology of the synthesized MnO_2. Fig. 21a shows the HRTEM results and Fig. 21b shows XRD of the synthesized MnO_2. The diffraction peaks of synthesized MnO_2 significantly matches the pyrolusite MnO_2 (or β-MnO_2, PDF 24-0735). Specifically, the peaks shown at around 28.7°, 37.3°, 41.0°, 42.8°, 56.7°, 59.4°, 65.0°, 67.2° and 72.4° can be ascribed to the (1 1 0), (1 0 1), (2 0 0), (1 1 1), (2 1 1), (2 2 0), (0 0 2), (3 1 0), and (3 0 1) planes in β-MnO_2, respectively. The HRTEM also shows a lattice fringe of 0.312 nm, which can be assigned to the (1 1 0) phase of β-MnO_2. From the SEM image (Fig. 21c), the synthesized β-MnO_2 is composed of nanowires with length of several micrometers.

37
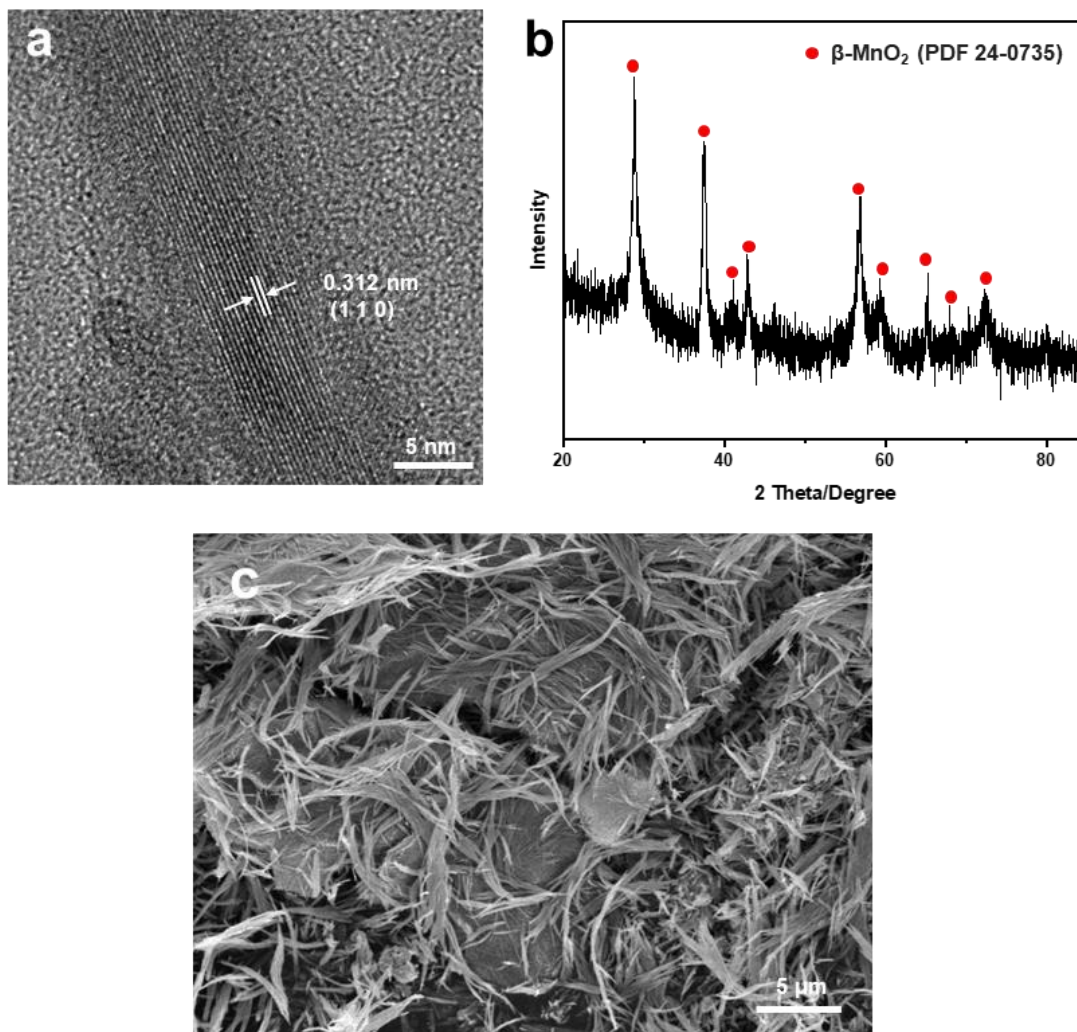
Figure 21. (a) High resolution TEM image of the synthesized MnO₂. (b) XRD patterns of the synthesized MnO₂. (c) SEM image of the synthesized MnO₂.

3.2.2 Ex-situ XRD Studies of the β-MnO₂ Cathode during Cycling

Firstly, 2 M ZnSO4 solution is employed as electrolyte to study the general electrochemical performance of Zn/MnO₂ battery. Galvanostatic test is performed from 1V to 1.9 V under 50 mAg⁻¹, starting with discharge process.
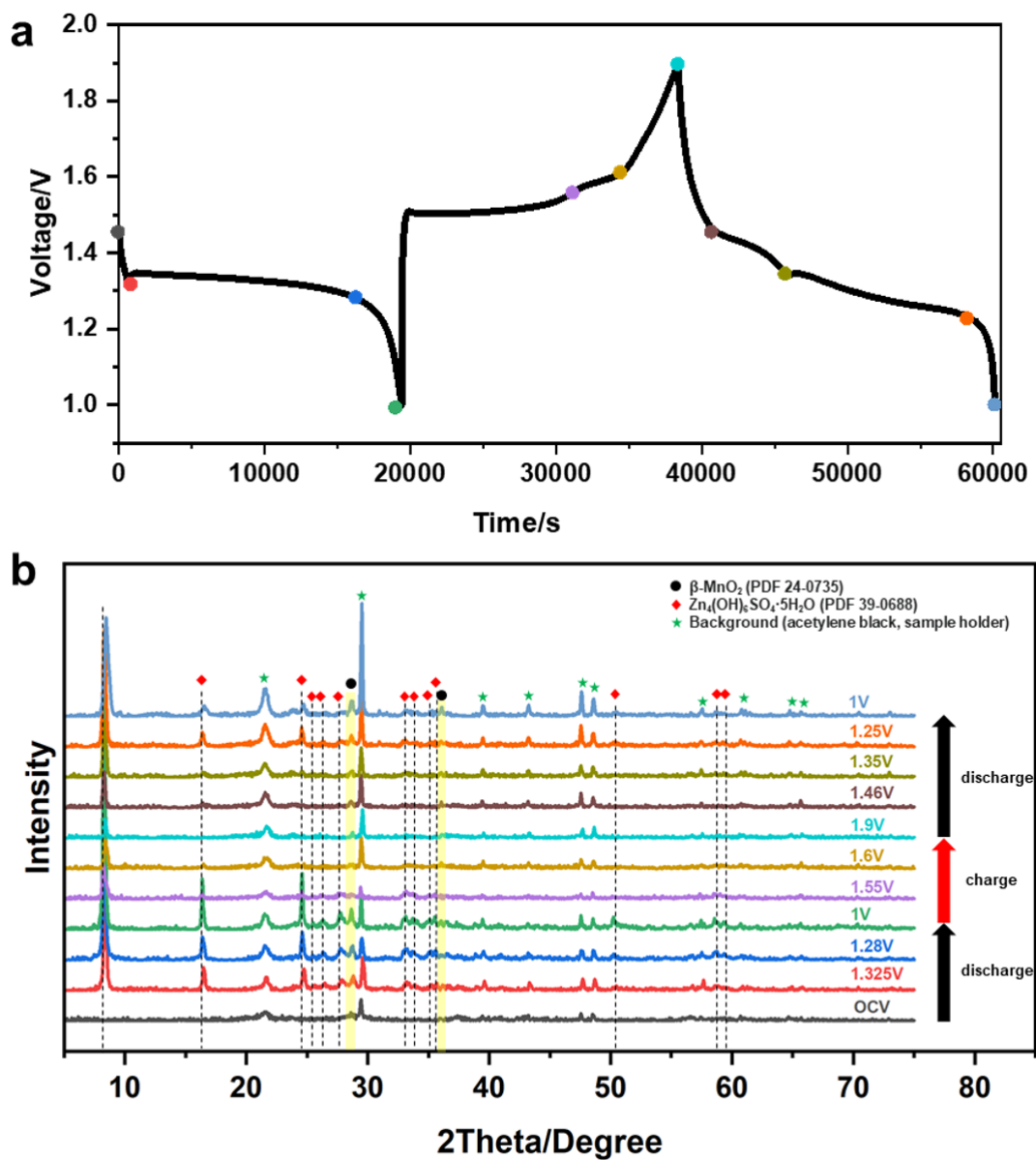
Figure 22. (a) Discharge/charge profile for first 2 cycles of Zn/β-MnO₂ battery in 2 M ZnSO₄ electrolyte (1 V - 1.9 V, 50 mAg⁻¹) and selected states for ex-situ XRD. (b) Ex-situ XRD of the cathode during first 2 cycles.

As a general overview of the crystal structure evolution during cycling, ex-situ XRD is performed for the first 2 cycles. The chosen voltages for ex-situ XRD is shown in Fig. 22a, and the corresponding diffraction peaks are shown in Fig. 22b. When the battery is discharged at its 1st cycle, new diffraction peaks arise at around 8.1°, 16.2°, 24.4°, 25.3°, 26.1°, 27.6°, 28.5°, 32.8°, 33.6°, 34.9°, 35.4°, 36.3°, 50.1°, 58.5°, 59.2°, which can be attributed to (0 0 1),(0 0 2), (0 0 3), (2 -1 2), (1 -1 3), (0 1 3), (-1 0 3), (3 -1 0), (1 2 1), (-3 1 1), (2 -3 2), (1 2 2), (0 0 6), (1 -5 0), (0 0 7) planes in $Zn_4(OH)_6SO_4{\cdot}5H_2O$ (PDF 39-0688), respectively. When the battery is further charged at its 2nd cycle, the diffraction peaks for ZHS weaken, indicating that the amount of ZHS decreases when charged. However, it is essential to note that even when the battery is charged to 1.55V and 1.6V at its 2nd cycle, diffraction peaks for ZHS can still be detected, especially for peaks at small angles such as 8.07° and 16.22° (The importance of the residual ZHS at 1.55 V and 1.6 V will be discussed in subsequent content). Then, after the battery is discharged back to 1 V at its 2nd cycle, the diffraction peaks of ZHS become stronger again. As discussed in Chapter 1, the generation of ZHS during discharge process is caused by the conversion reaction and dissolution reaction which consumes protons in the electrolyte. The reaction equations are shown below:

$$MnO_2 + H^+ + e^- \rightarrow MnOOH$$

$$3MnO_2 + 8Zn^{2+} + 2SO_4^{2-} + 16H_2O + 6e^- \rightarrow 3Mn^{2+} + 2Zn_4(OH)_6SO_4{\cdot}5H_2O$$
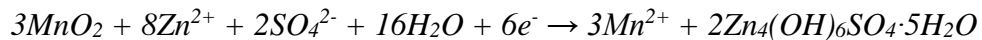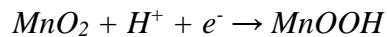
When the battery is further charged, the abovementioned reactions can happen backwards partially, causing the reduction of pH and the weaknesses of ZHS diffraction peaks.

3.2.3 SEM Studies of the β-MnO₂ Cathode during Cycling

To verify the XRD results and investigate the evolution of morphologies during cycling, SEM images of cathode surface and cross-section are taken. The original cathode (as shown in Fig. 23a) is simply composed of MnO_2 nanowires. After the battery is fully discharged (1 V), the surface of the cathode is covered with layers of hexagonal flakes (as shown in Fig. 23b). From our EDS results (as shown in Fig. 24a), the hexagonal flakes contain elements of Zn, O, S, and can be ascribed to ZHS, which is consistent with the ex-situ XRD results. When the battery is charged to 1.55 V at its 2nd cycle (as shown in Fig 23c), layers of hexagonal morphologies still exist, but their dimensions are reduced significantly, which explains the attenuation of ZHS characteristic peaks in XRD patterns. Remarkably, a layer of irregular aggregations form on the surface of the cathode after the battery is further charged to 1.6 V (as shown in Fig 23d). EDS results show that the formed aggregations are composed of Zn, Mn, O, S (as shown in Fig. 24b). The existence of Mn demonstrates that the formed aggregates are not ZHS. After the battery is fully charged to 1.9 V, as shown in Fig 23e, the morphology of the entire cathode surface transforms into the irregular aggregations. Furthermore, even after the battery is fully discharged (1 V), the formed aggregations still exist, and parts of them are covered by the ZHS hexagonal flakes that are newly generated during the discharge process (Fig. 23f). This phenomenon proves that the generation of the irregular aggregations is irreversible.
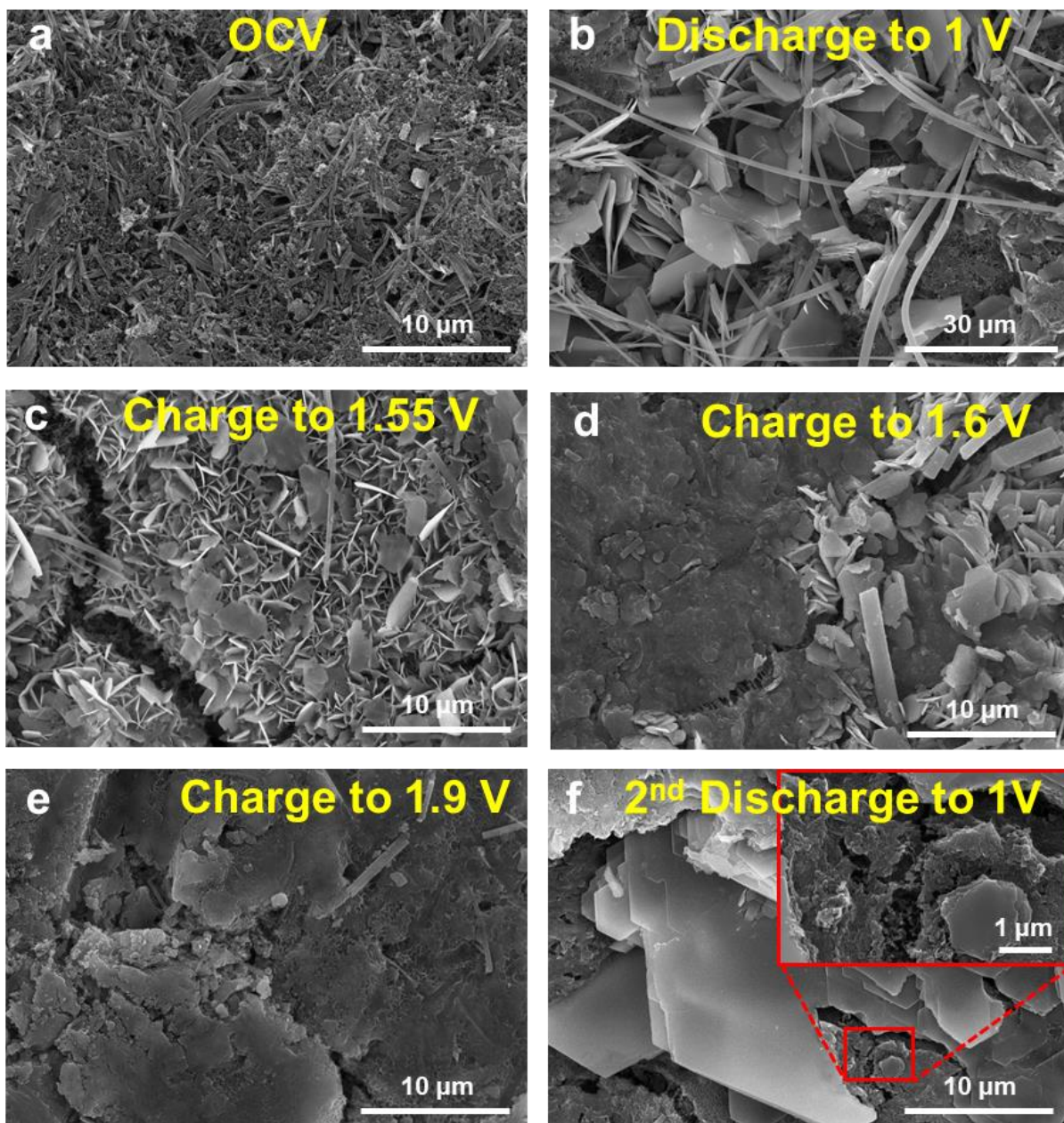
Figure 23. SEM images of cathode (a) at open circuit voltage, (b) after discharged to 1V at 1st cycle, (c) after charged to 1.55V at 2nd cycle, (d) after charged to 1.6V at 2nd cycle, (e) after charged to 1.9V at 2nd cycle, (f) after discharged to 1V at 2nd cycle.

a

Element	Weight %	Atomic %	Net Int.	Error %	Kratio	Z	R	A	F
C K	6.27	13.03	25.83	16.46	0.01	1.17	0.9	0.17	1
O K	41.79	65.15	791.18	8.46	0.16	1.13	0.92	0.33	1
Si K	2.63	2.33	129.26	9.55	0.01	1.03	0.97	0.52	1.01
S K	4.93	3.84	263.07	6.16	0.04	1.01	0.99	0.7	1.01
Mn K	1.94	0.88	55.94	12.27	0.02	0.86	1.04	0.99	1.21
Zn K	36.87	14.07	422.14	3.58	0.34	0.84	1.05	1	1.08
Au L	5.56	0.70	17.50	39.91	0.04	0.59	1.13	1.02	1.13

b

Element	Weight %	Atomic %	Net Int.	Error %	Kratio	Z	R	A	F
C K	10.42	23.42	44.12	13.37	0.03	1.2	0.89	0.21	1
O K	29.48	49.73	476.42	8.79	0.11	1.16	0.91	0.33	1
S K	3.48	2.93	163.30	8.42	0.03	1.04	0.98	0.72	1.01
Mn K	26.29	12.91	576.92	2.93	0.25	0.89	1.03	0.99	1.08
Zn K	24.82	10.25	238.36	4.44	0.23	0.87	1.05	0.99	1.08
Au L	5.51	0.75	14.81	41.74	0.04	0.61	1.13	1.02	1.13

Figure 24. EDS results of (a) the formed hexagonal flakes after the battery is discharged to 1 V at its 1ˢᵗ cycle, (b) the formed aggregations after the Zn/β-MnO₂ battery is charged to 1.6 V at its 2nd cycle.

43

To obtain a clearer view of the formed aggregations, the cathode is cut by a scalpel, and the cross-section is observed under SEM. Fig. 25a shows the cross-section of the original
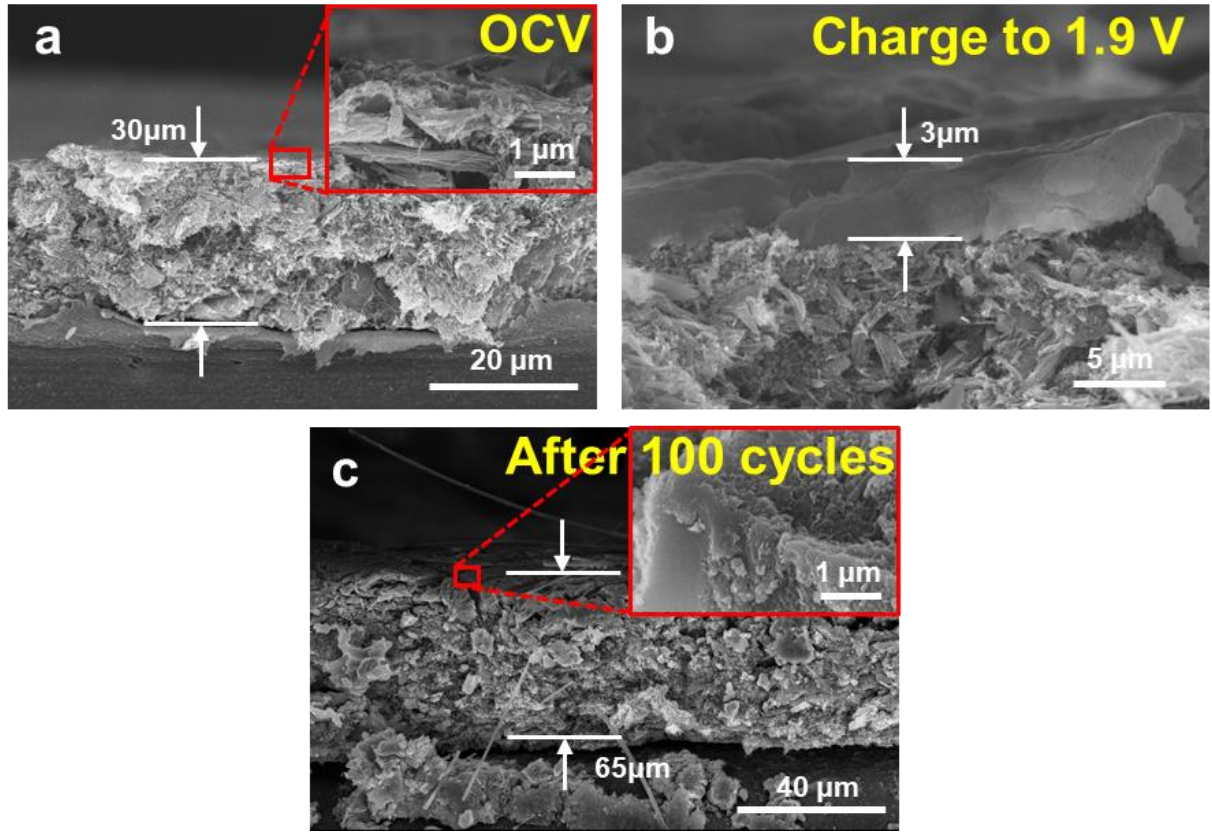
Figure 25. SEM images of cathode cross-section (a) at open circuit voltage, (b) after charged to 1.9V at 2nd cycle, (c) after charged to 1.9V at 100th cycle.

cathode, which is primarily made up of β-MnO_2 nanowires. The thickness of the cathode is about 30 μm. Fig. 25b shows the cross-section of the cathode after the battery is fully charged to 1.9 V at its 2nd cycle. Notably, a layer of aggregations with about 3 μm thickness form on the top surface of the cathode. Beneath the aggregated layer, the morphology of MnO_2 nanowires remains intact. Nevertheless, after the battery is fully charged (1.9 V) at its 100th

cycle, there are significant changes on the cathode morphology, as shown in Fig. 25c. The entire cathode transforms into irregular aggregations and nanowires cannot be observed. In addition, the thickness of cathode material increases to 65 μm, indicating a large volume change which is harmful to the battery system. The newly formed aggregations can also be directly observed on the surface of the cathode after cycled 100 times, which are shown in Fig. 26. After 100 cycles, the color of the cathode surface turns from black into dull brown, which is very likely caused by the formation and accumulation of the aggregations.
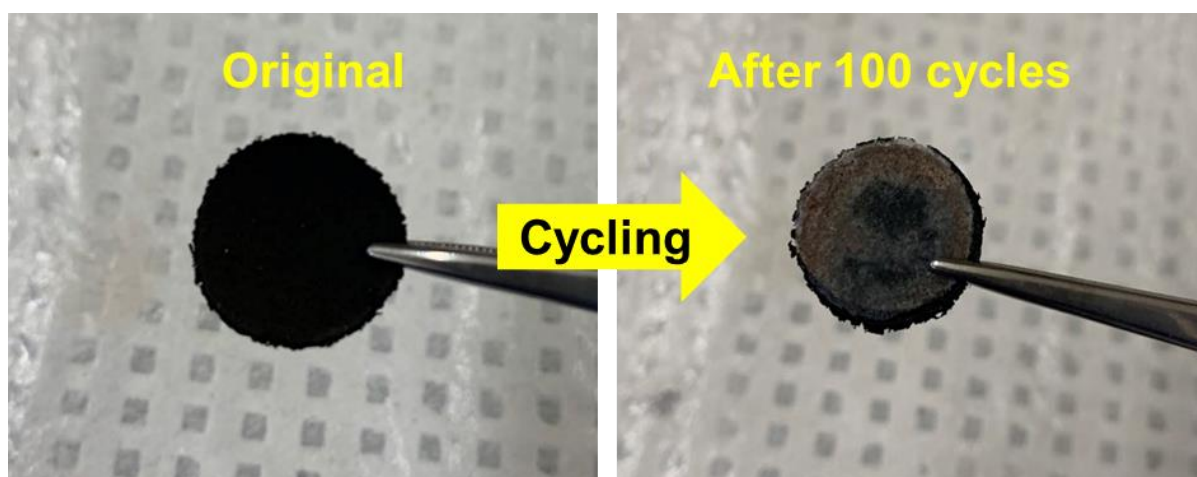
Figure 26. Pictures of the cathode disc before and after cycling.

Based on the SEM results, the generation of the irregular aggregations, which happens from 1.55 V to 1.9 V during charge process, is irreversible. As a result, when the battery is cycled, the MnO_2 nanowires gradually converts into the irregular aggregations. Also, since the formation of the aggregations containing Zn, Mn, O, S happen in the charge process where the cathode is oxidized, it is very likely that the aggregation is formed due to the reaction between ZHS and Mn ions dissolved in the electrolyte.

45

3.2.4 Characterization of the Synthesized Zn₄(OH)₆SO₄·5H₂O Cathode

To further verify that ZHS is the precursor the irregular aggregations, $Zn_4(OH)_6SO_4 \cdot 5H_2O$ is synthesized and used as cathode materials. Fig. 27 and Fig. 28 shows the XRD patterns and SEM images with EDS mapping, respectively. The diffraction peaks matches the standard card of $Zn_4(OH)_6SO_4 \cdot 5H_2O$ (PDF 39-0688) very well. Moreover, from the SEM image with EDS mapping, the synthesized ZHS shows the morphology of nanoflakes, which are similar as observed ZHS nanoflakes on β-MnO_2 cathode after discharged.
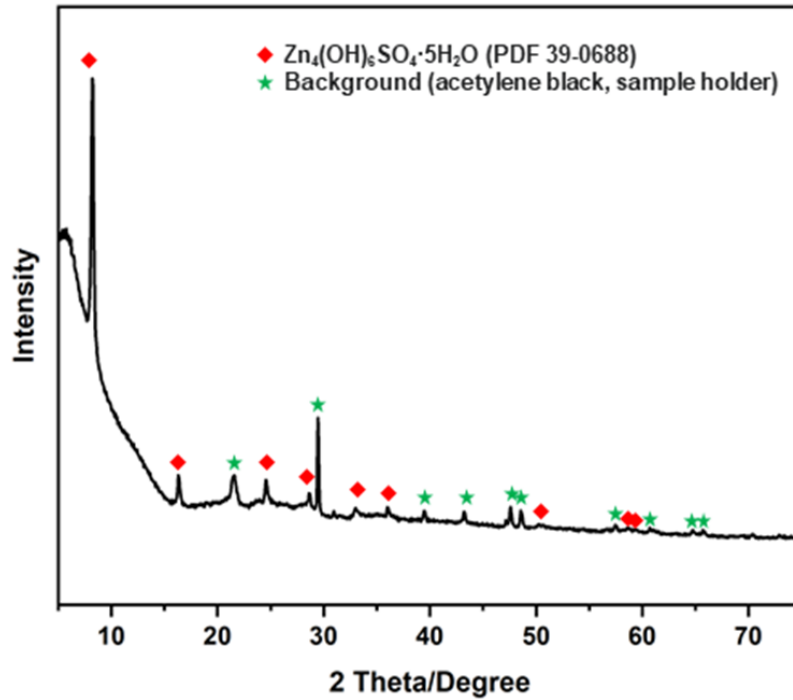
Figure 27. XRD patterns of the ZHS cathode.
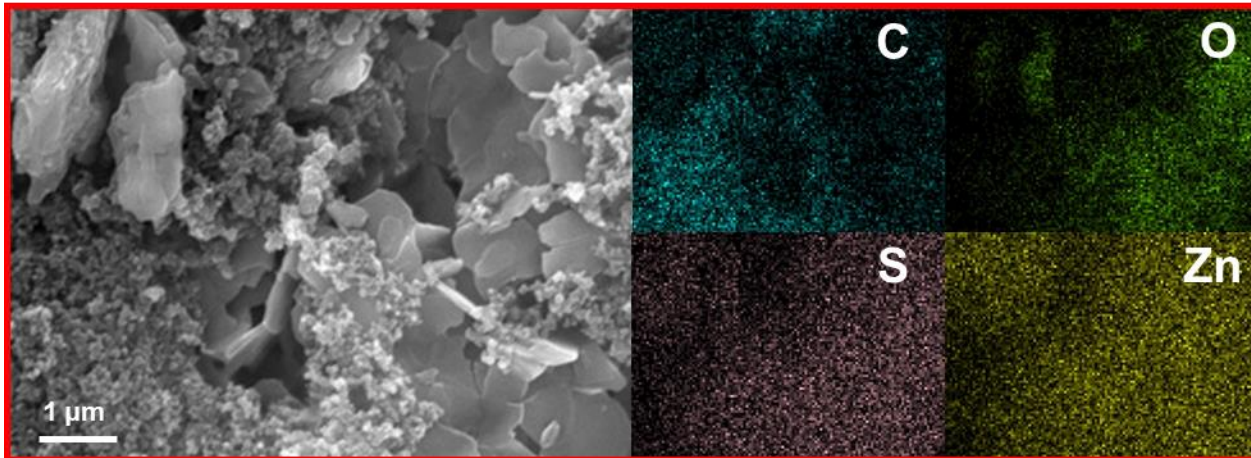
Figure 28. SEM image and corresponding EDS mapping of the ZHS cathode.

3.2.5 Galvanostatic Test of the Zn/Zn$_4$(OH)$_6$SO$_4$·5H$_2$O Battery

Cathode containing ZHS as active materials is made and 2 M ZnSO$_4$ + 0.1 M MnSO$_4$ solution is used as electrolyte. The pH of the electrolyte is modified to around 5.5 by slowly dissolving ZnO in the electrolyte. The adjusted pH is to imitate the pH of the electrolyte after 1st discharge process[69]. The assembled battery is then charged with the electrochemical window 1.0 V-1.9 V at the current density of 50 mAg^{-1}. As shown in Fig. 29, there is only 1 plateau during charge process, which originates from 1.55 V to 1.65 V. It is significantly consistent with the voltages where the irreversible reaction takes place in Zn/β-MnO$_2$ battery during charge process. Moreover, the discharge capacity is obviously less than the charge capacity at 1st cycle, demonstrating that the reaction in charge process is irreversible.

47
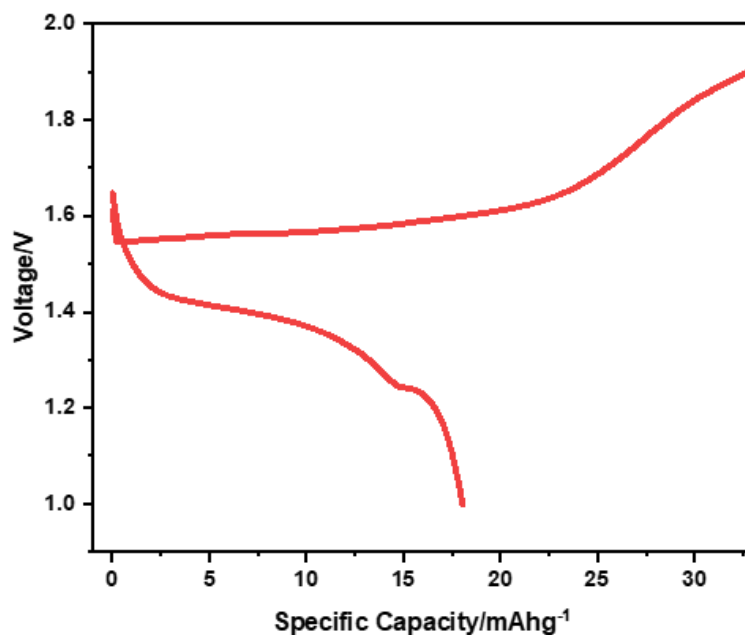
Figure 29. Charge/discharge profile for the 1st cycle of ZHS/Zn battery in 2 M ZnSO$_4$ + 0.1 M MnSO$_4$ electrolyte (1 V - 1.9 V, 50 mAg^{-1})

3.2.6 SEM studies of the Zn$_4$(OH)$_6$SO$_4$·5H$_2$O Cathode during Cycling

SEM images are taken to observe the morphology evolution in ZHS cathode during cycling. As shown in Fig. 30a, the original cathode mainly contains Zn$_4$(OH)$_6$SO$_4$·5H$_2$O nanoflakes. After the battery is fully charged (1.9 V), the irregular aggregations form on the surface of the cathode (as shown in Fig. 30b). From the EDS results (as shown in Fig. 31), the formed aggregations contain Zn, Mn, O, and S. Besides, the formed aggregations still exist even after the battery is fully discharged (1 V) (Fig. 30c). This phenomenon strongly illustrates that ZHS is able to react with Mn ions from the electrolyte to form irregular aggregations at

over 1.55 V during the charge process, and the formed aggregations are difficult to be dissolved back into Mn^{2+} ions.
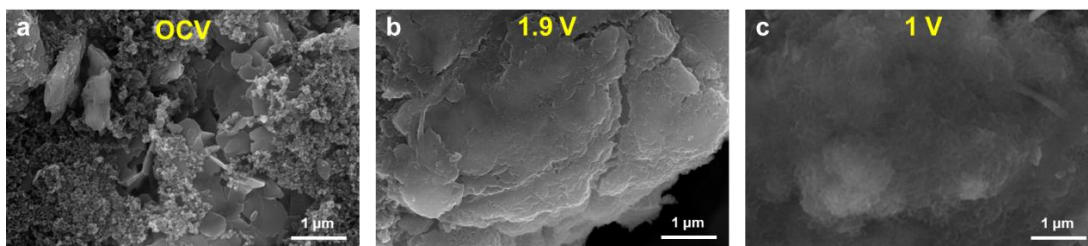
Figure 30. SEM images of the ZHS cathode (a) at open-circuit voltage, (b) after fully charged (1.9 V), (c) after further fully discharged (1 V).
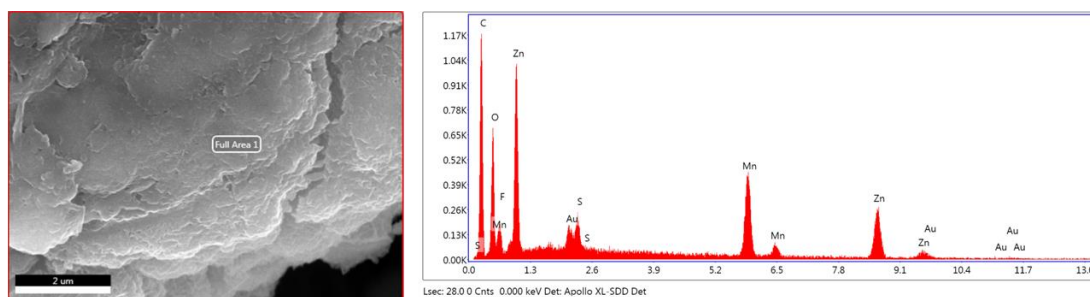
Element	Weight %	Atomic %	Net Int.	Error %	Kratio	Z	R	A	F
C K	45.24	66.75	255.98	9.09	0.16	1.1	0.94	0.31	1
O K	19.02	21.06	154.29	10.91	0.04	1.06	0.96	0.19	1
F K	3.54	3.30	32.10	15.83	0.01	0.99	0.97	0.16	1
S K	1.19	0.66	55.71	12.11	0.01	0.95	1.02	0.81	1.01
Mn K	10.71	3.45	214.97	4.02	0.10	0.81	1.06	1.01	1.11
Zn K	16.26	4.41	141.06	5.02	0.14	0.78	1.07	1	1.1
Au L	4.05	0.36	9.76	41.99	0.03	0.55	1.14	1.03	1.15

Figure 31. EDS results of the formed aggregations after the ZHS/Zn battery is charged to 1.9 V.

49

3.2.7 TEM and HRTEM studies of the β-MnO₂ Cathode during Cycling

As previously demonstrated, ZHS can react with Mn^{2+} ions to form irregular aggregations; however, the crystal structures of the formed aggregations are still unknown.
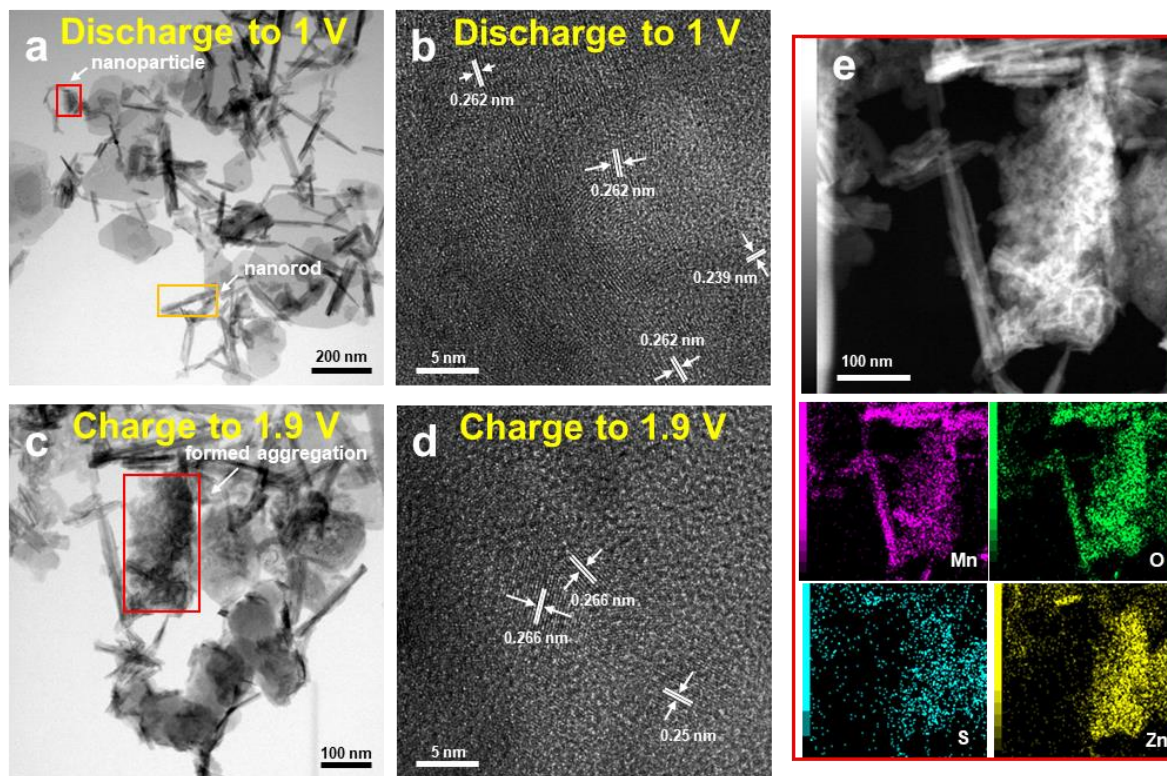
Figure 32. TEM images of cathode materials (a) after discharged to 1 V at 1st cycle, (c) after charged to 1.9 V at 2nd cycle. High-resolution TEM images of (b) formed nanoparticles after discharged to 1 V at 1st cycle, (d) formed aggregation after charged to 1.9 V at 2nd cycle. (e) EDS mapping of the formed aggregation after charged to 1.9 V at 2nd cycle.

To further study the crystal structure evolution of the formed aggregations and the reaction mechanisms, TEM and high-resolution TEM are performed for the cathode of the

Zn/β-MnO$_2$ battery material during cycling. As shown in Fig. 32a, after fully discharged (1 V) at its 1st cycle, ZHS nanoflakes, nanorods, and a newly formed nanoparticles can be observed on the cathode. High-resolution TEM is then conducted for the newly formed particles. Fig. 32b shows the lattice fringes of 0.262 nm and 0.239 nm, which can be ascribed to the (0 2 0) and (2 0 0) planes in monoclinic MnOOH.[70] Additionally, the nanorods are observed by high-resolution TEM and EDS mapping, which are shown in Fig. 33a. The lattice fringes of 0.312 nm and 0.241 nm are in agreement with the d-space of (1 1 0) and (1 0 1) planes in β-MnO$_2$.[71]

Moreover, from the EDS mapping results (Fig. 33b), Zn element is not concentrated in the nanorods compared with Mn element and O element, and the distribution of Zn element is very similar as that of S element. Hence, it is inferred that the little amount of Zn element in the nanorods are caused by the diffusion of ZnSO$_4$ electrolyte into the β-MnO$_2$ nanorods and there are no obvious Zn intercalation reaction.
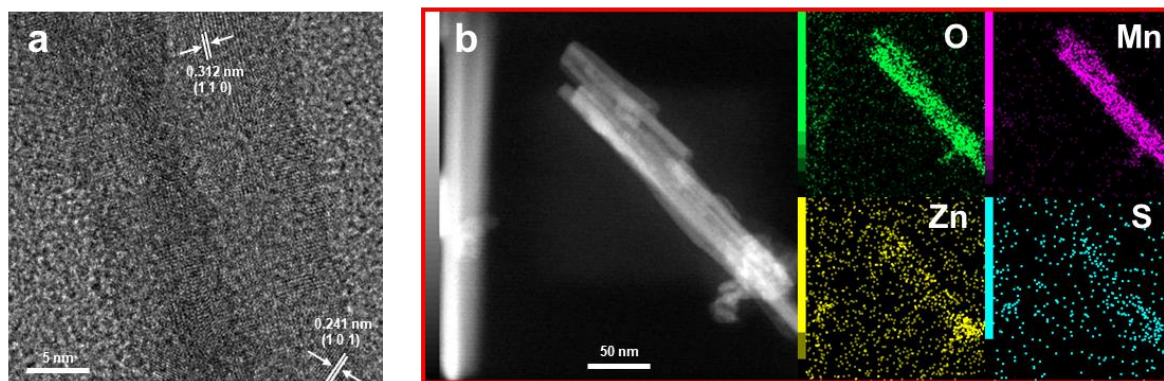
Figure 33. (a) HRTEM image of the nanorods after the Zn/β-MnO$_2$ battery is fully discharged (1 V). (b) EDS mapping of the nanorods after the Zn/β-MnO$_2$ battery is fully discharged (1 V).

51
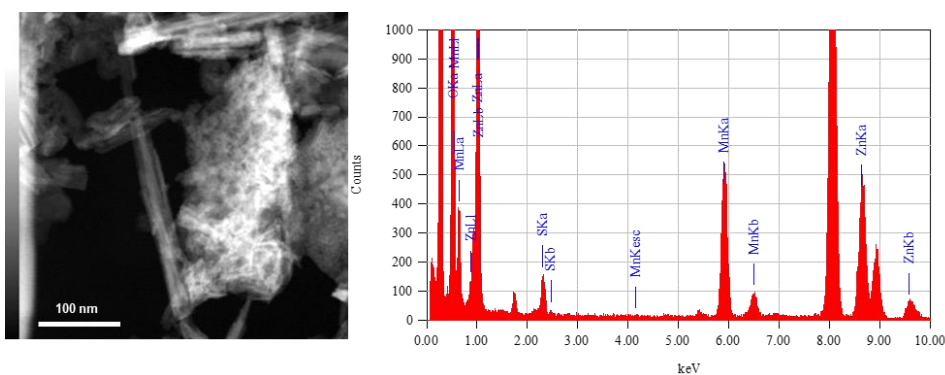
The Film Standardless Standardless Quantitative Analysis
Fitting Coefficient:0.6660

Element	Mass %	Atomic %	Counts	Sigma
O K	39.22	70.27	12344.84	0.65
S K	2.52	2.26	1160.00	0.16
Mn K	23.23	12.12	7731.20	0.56
Zn K	35.03	15.35	6780.40	0.93

Figure 34. EDS results of the formed aggregations after the Zn/β-MnO₂ battery is charged to 1.9 V at its 2nd cycle.

After the battery is fully charged to 1.9 V, the aggregations are formed (Fig. 32c), which contain element of Mn, Zn, O and S based on EDS mapping (Fig. 32e). Moreover, the EDS results (Fig. 34) shows that the amount of S is little. It is believed that the insignificant amount of S element is from the residue of incompletely reacted ZHS. From the high-resolution TEM image of the formed aggregations (Fig. 32d), part of the aggregations is disordered, demonstrating that the formed aggregations have very low crystallinity. Besides the disorder region, lattice fringes of 0.266 nm and 0.25 nm can be detected, which can be ascribed to (3 1 0) and (2 0 3) planes in tetragonal $(Zn,Mn)_2Mn_5O_{12} \cdot 4H_2O$ (or Woodruffite, a mineral with dull

brown color)[72]. The gradual phase transform from β-MnO$_2$ to (Zn,Mn)$_2$Mn$_5$O$_{12}$·4H$_2$O (ZMO) can also be detected by the ex-situ XRD patterns shown in Fig. 35.
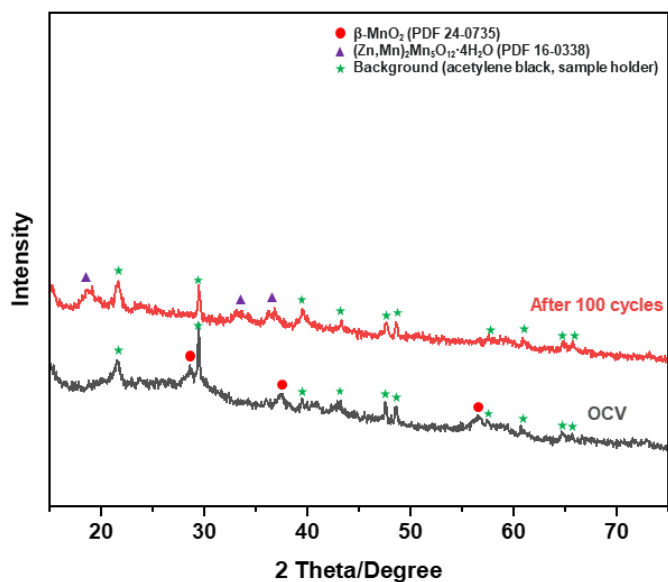
Figure 35. Ex-situ XRD patterns of the cathode (in 2M ZnSO$_4$ electrolyte) before cycling and after cycled 100 times.

3.2.8 Galvanostatic Test of the Zn/β-MnO$_2$ Battery

The cyclability of the Zn/β-MnO$_2$ battery is shown in Fig. 36a, the battery achieves a remarkable specific capacity of 314 mAhg^{-1} at its 5th cycle; however, it experiences rapid capacity fading after further cycles. Fig. 36b exhibits the discharge/charge profile of the Zn/β-MnO$_2$ battery, it is demonstrated that although the capacity fades dramatically from 3rd cycle to 30th cycle, the capacity contributed from 1st discharge plateau (from 1.5 V to 1.35 V) remains

53
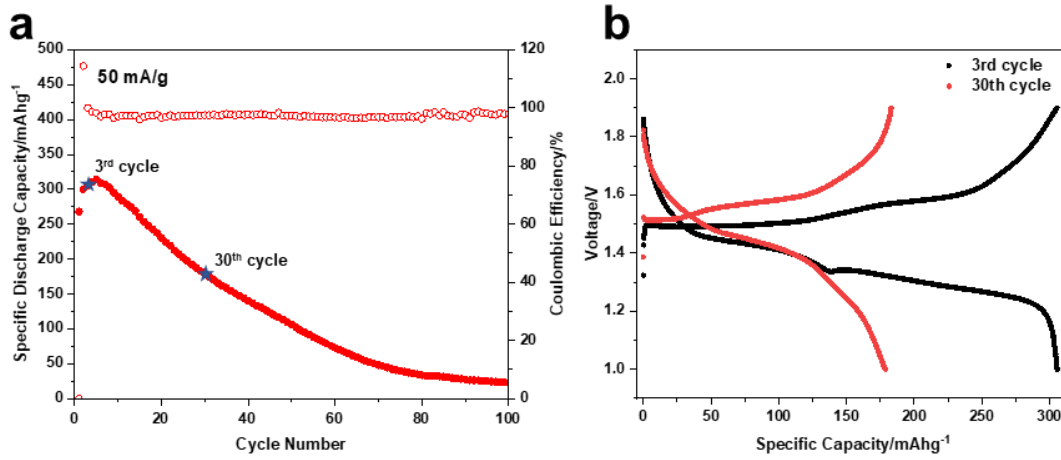
Figure 36. (a) Cyclability of Zn/β-MnO₂ battery in 2 M ZnSO₄ electrolyte (1 V - 1.9 V, 50 mAg⁻¹). (b) Discharge/charge profile for 3ʳᵈ cycle and 30ᵗʰ cycle of Zn/β-MnO₂ battery in 2 M ZnSO₄ electrolyte (1 V - 1.9 V, 50 mAg⁻¹).

unchanged. The main capacity loss is caused by the shorten of 2nd discharge plateau (from 1.35 V to 1.2 V).

3.2.9 Mn^{2+} Concentration Evolution in the Zn/β-MnO₂ Battery during Cycling

ICP-MS is used to study the Mn^{2+} concentration evolution in the Zn/β-MnO₂ battery during cycling. Firstly, the concentration of Mn^{2+} ions in the electrolyte after 1st discharge process is measured. Since the original electrolyte is 2 M ZnSO₄ without any Mn^{2+} ions, the dissolved Mn^{2+} ions after the 1st discharge process must originate from the dissolution reaction, which is a 2 e⁻ transfer reaction. Based on this, we can calculate the capacity contribution from dissolution reaction during the 1st discharge process. The detailed calculations are shown below:

$$C_{contribution} = ([Mn^{2+}]_{dis} \cdot V_{electrolyte} \cdot M_{Mn} / m_{MnO2}) \cdot C_{2e}$$

(Note: $C_{contribution}$ is the capacity contribution from dissolution reaction; $[Mn^{2+}]_{dis}$ is the concentration of Mn^{2+} ions after the 1st discharge process; $V_{electrolyte}$ is the volume of electrolyte; M_{Mn} is the atomic mass of Mn element; m_{MnO2} is the loading mass of MnO_2 cathode; C_{2e} is the theoretical capacity of 2 e^- transfer reaction for MnO_2.)

All abovementioned parameters are known so that $C_{contribution}$ can be calculated. The concentration of Mn^{2+} after the 1st discharge process is about 0.077 M, and the calculated capacity from dissolution is about 188.61 mAhg^{-1}. Considering the total specific capacity of the 1st discharge process is 267.93 mAhg^{-1}, the capacity contributed by the dissolution reaction is above 70%. This result strongly proves that the dissolution reaction is one of the main reactions happening in the 1st cycle.

ICP-MS is then conducted to measure the concentration of Mn ions in the electrolyte at different voltages for 3rd cycle and 30th cycle. As shown in Fig. 37, for both the 3rd cycle and the 30th cycle, the concentration of Mn ions in the electrolyte increases when the battery is discharged, and decreases when the battery is charged, indicating the dissolution process and deposition process, respectively. More importantly, during the 2nd discharge plateau (from 1.35 V to 1.2 V), the Mn concentration in the electrolyte for 30th cycle increases much less than that for 3rd cycle, revealing that the main capacity loss during the 2nd discharge plateau (from 1.35 V to 1.2 V) could be caused by the decline of dissolution reaction. The phase transformation from β-MnO_2 to lowly crystallized aggregations during cycling can cause the attenuation of dissolution reaction; so, the irreversible reaction during charge process (1.55 V – 1.9 V) is considered as the main cause of capacity loss in the Zn/β-MnO_2 battery.
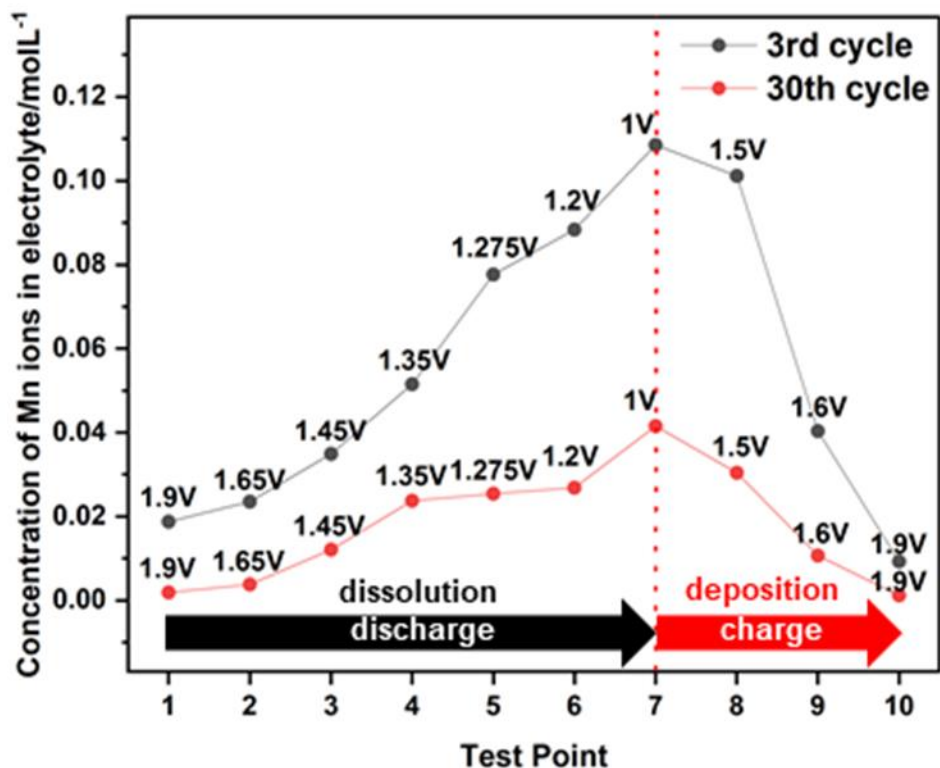
Figure 37. The concentration of Mn ions in electrolyte at different voltages for the 3rd cycle and the 30th cycle.

3.2.10 Electrochemical Impedance of the Zn/β-MnO₂ Battery during Charge Process

To further study the influence of generated ZMO, electrochemical impedance spectroscopy is conducted for the Zn/β-MnO₂ battery at various voltages (1.5 V, 1.55 V, 1.9 V) during charge process. The EIS results and fitting data with corresponding equivalent circuits are shown in Fig. 38 and Table 5. From these EIS results, the electrolyte/electrode

56

resistance experiences negligible change when charged. Also, when the Zn/β-MnO₂ is charged from 1.5 V to 1.6 V, the change of charge-transfer resistance Rct is negligible (395 Ω at 1.5 V, 397.7 Ω at 1.55 V). However, after the battery is fully charged to 1.9 V, where the battery experiences the irreversible reaction generating ZMO, the charge-transfer resistance increases to ~489 Ω. It is very likely that the generation of ZMO blocks the tunnel structure of β-MnO₂ and therefore hinders the charge-transfer reactions.
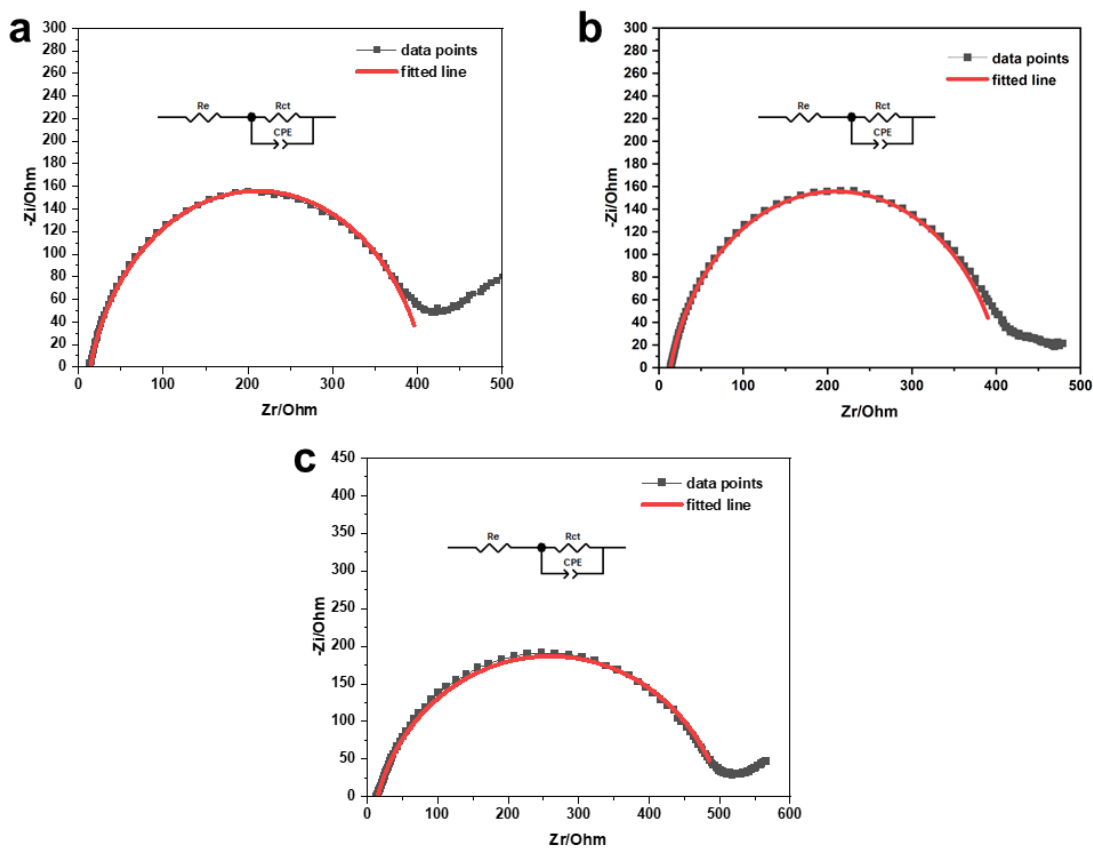
Figure 38. Nyquist Plots of Zn/β-MnO₂ in 2 M ZnSO₄ electrolyte with detailed fitting results and corresponding equivalent circuits (a) after charged to 1.5 V at 2nd cycle, (b) after charged to 1.55 V at 2nd cycle, (c) after charged to 1.9 V at 2nd cycle.

Table 5. Detailed fitting results of the electrochemical impedances.

Sample Details	Re/Ohm	Rct/Ohm	CPE-T	CPE-P
$ZnSO_4$-1.5 V	13.82	395	3.69E-06	0.8515
$ZnSO_4$-1.55 V	13.86	397.7	4.47E-06	0.85318
$ZnSO_4$-1.9 V	14.48	489.2	6.37E-06	0.82986

3.2.11 Verification on Mn^{2+} additives

As discussed in Chapter 1, pre-adding Mn^{2+} ions in electrolyte is a common strategy in Zn/MnO_2 batteries; however, the mechanism and efficiency of Mn^{2+} additives remain controversial. Therefore, batteries containing β-MnO_2 as cathode and 2 M $ZnSO_4$ + 0.2 M $MnSO_4$ as electrolyte are cycled at the current density of 50 mAg^{-1}. As shown in Fig. 39, although pre-adding Mn ions in the electrolyte can improve the capacity in a considerable amount, the cycling performance is apparently not enhanced. The discharge/charge profiles of the 3rd cycle and 30th cycle are shown in Fig. 40a and Fig. 40b, respectively. Obviously, the 2nd discharge plateau cannot be stabilized, which is similar as batteries in 2 M $ZnSO_4$ electrolyte.

For studying the mechanism of capacity fading, SEM images are taken to observe the morphology transformation. As shown in Fig. 41, during charge process, MnO_2 nanowires irreversibly convert into irregular aggregations, which exhibits the same reactions as in 2 M $ZnSO_4$ electrolyte. Therefore, pre-adding Mn^{2+} does not show any improvement in cycling
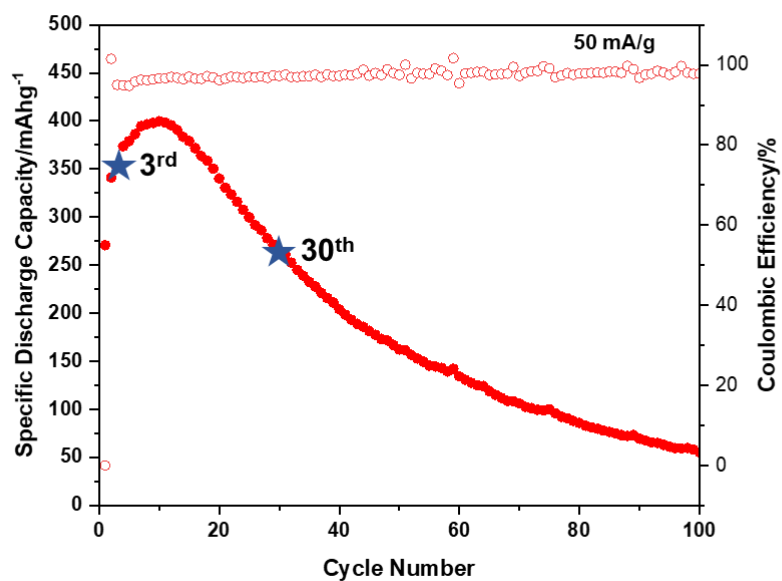
Figure 39. Cycling performance of the Zn/β-MnO₂ battery in 2 M ZnSO₄ + 0.2 M MnSO₄ electrolyte (1 V - 1.9 V, 50 mAg⁻¹).
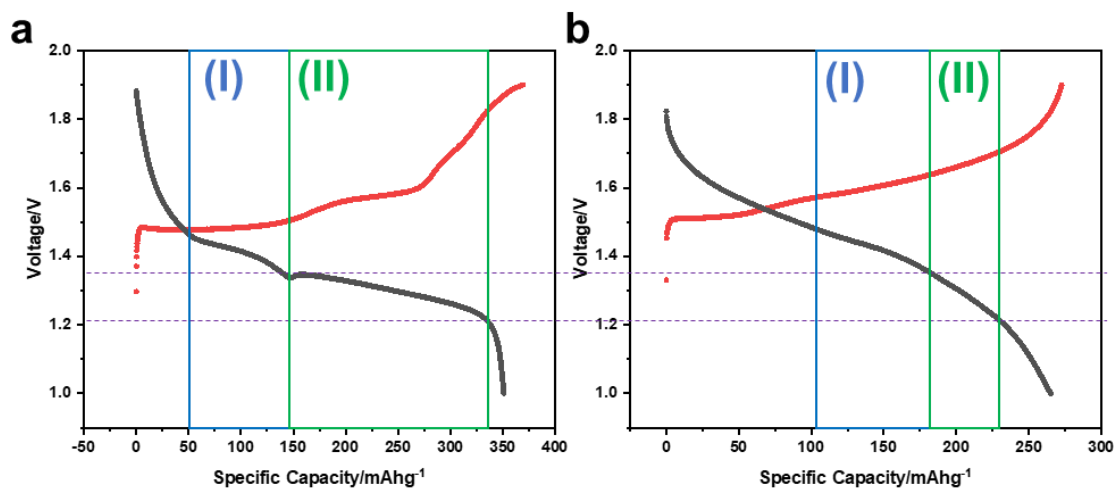
Figure 40. Discharge/charge profile of Zn/β-MnO₂ battery in 2 M ZnSO₄ + 0.2 M MnSO₄ electrolyte at (a) the 3ʳᵈ cycle, (b) the 30ᵗʰ cycle.
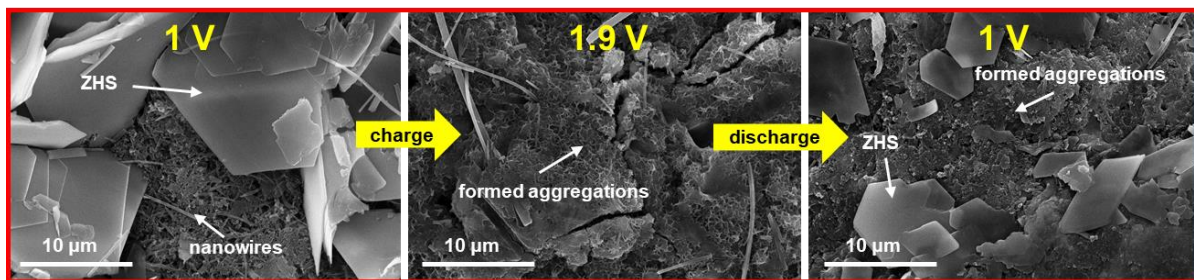
Figure 41. SEM images of the β-MnO₂ cathode during the 1ˢᵗ 2 cycles in 2M ZnSO₄ + 0.2 M MnSO₄ electrolyte.

performance at a small current density of 50 mAg⁻¹, and the additional capacity is considered from the reaction between pre-added Mn ions and side products ZHS.

3.3 Conclusions

To conclude, in this chapter, experiments are accomplished to research the reaction mechanisms in Zn/β-MnO₂. From the characterization results and electrochemical results, the main reactions during discharge process are the conversion reaction ($MnO_2 \rightarrow MnOOH$) and the dissolution reaction ($MnO_2 \rightarrow Mn^{2+}$). The main irreversible reaction occurs in the charge process at over 1.55 V, which is a reaction between side product ZHS and dissolved Mn^{2+} ions in electrolyte. Fig. 42 shows a schematic process of the crystal structure change during cycling. Basically, during discharge process, part of the β-MnO₂ transforms into MnOOH via the conversion reactions. The other part of β-MnO₂ is dissolved by the protons in the electrolyte and becomes Mn^{2+} ions. Since both the conversion reaction and dissolution reaction consumes protons in electrolyte, the total pH in the electrolyte increases, which leads to the generation

of ZHS. When charged, MnOOH can be oxidized back to β-MnO$_2$, as a reversible reaction; however, the side product ZHS can react with Mn^{2+} ions in the electrolyte, to form Woodruffite (ZMO aggregations) which cannot be further reduced to ZHS and Mn^{2+} ions. Hence, this reaction is considered as an irreversible reaction and the main cause of capacity fading.
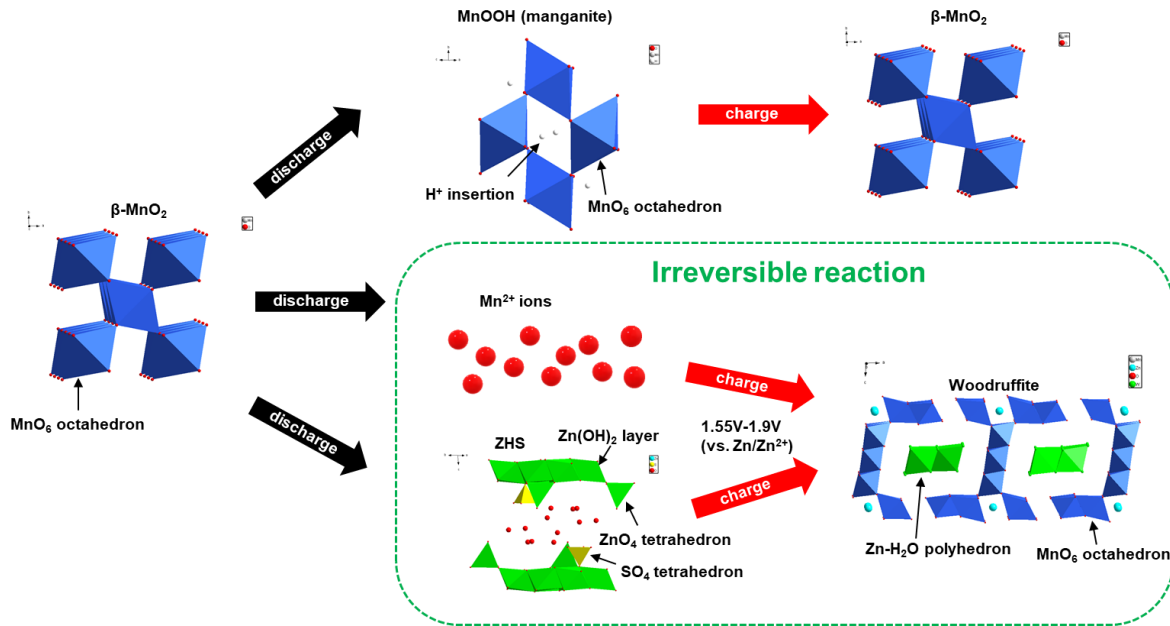
Figure 42. Schematic illustration of phase change of β-MnO$_2$ cathode during cycling.

Fig. 43 gives a more straightforward overview of the morphology change of the cathode materials during cycling. During the 1st discharge process, the generated ZHS nanoflakes cover the surface of the β-MnO$_2$ cathode, and the dissolved Mn^{2+} ions migrate to the electrolyte. After the battery is fully charged, Mn^{2+} ions near cathode react with the ZHS nanoflakes, forming the dull brown ZMO aggregations. The aggregations generate a dense and thick layer on the top of the cathode, and partially blocks the pathway to underneath MnO$_2$ nanowires. Afterwards, at the 2nd discharge process, similar reactions during the 1st discharge happens

again, the generated ZHS and residual ZMO covers the surface. After 100 cycles, the entire cathode transforms into dense, thick ZMO aggregations, causing huge volume change and capacity fading.
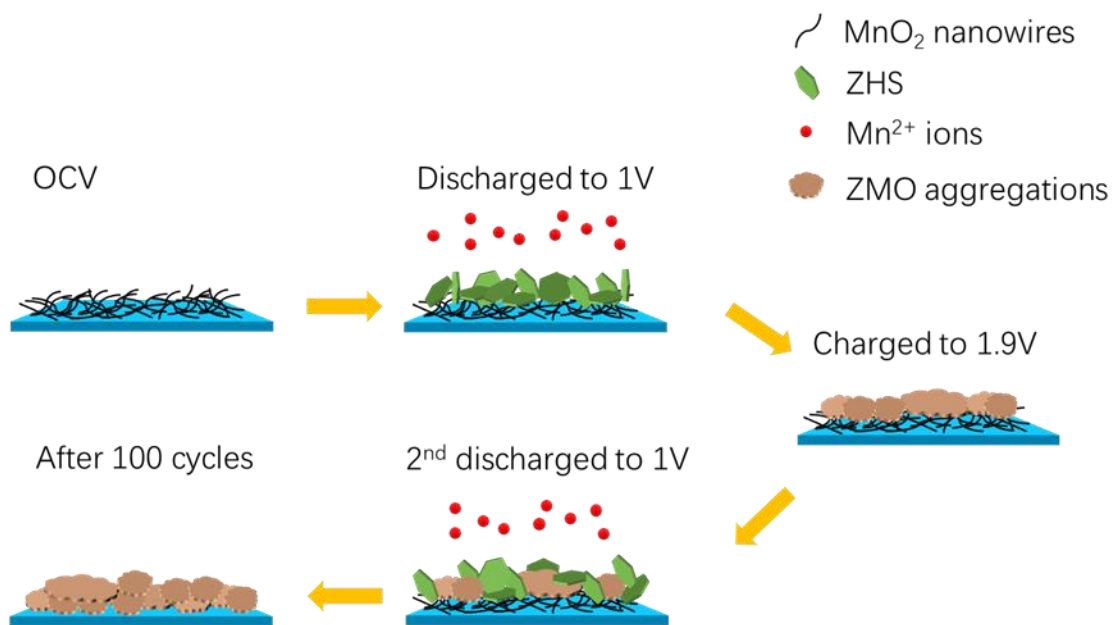
Figure 43. Schematic illustration of the cathode morphology change during cycling.

Chapter 4: Regulating Proton Concentration by Ion Exchange Resin in Zn/β-MnO₂ Batteries

As comprehensively discussed in Chapter 3, the precursor the irreversible reaction is ZHS, which is generated because the consumption of protons during discharge process. Since eliminating the reactants of the irreversible reaction is considered as an efficient strategy to achieve high reversibility in Zn/MnO₂ batteries, strongly acidic ion exchange resin (hydrogen form) is employed to regulate the proton distribution in the electrolyte and suppress the growth of ZHS in Chapter 4.

4.1 Strongly Acidic Ion Exchange Resin (IER)

Strongly acidic ion exchange resin (IER) is composed of cross-linked polystyrene matrix and sulphonate (SO_3^{2-}) functional groups which can be charged with protons (hydrogen form of strongly acidic IER)[73]. Strongly acidic IER can release protons and adsorb metal ions when the surrounding pH is relatively high, which can also happen in reverse when the surrounding pH is relatively low[74]. Therefore, hydrogen-formed strongly acidic IER (Dowex 50W X8, hydrogen form, 200-400 mesh, Sigma-Aldrich) is used to regulate the proton distribution in this work.

To have an overview of the morphology and functional groups of the ion exchange resin, SEM and FT-IR are conducted, respectively. As shown in Fig. 44a, the strongly acidic IER is made of beads with diameters around 80 μm. Fig. 44b shows the FT-IR spectrum of the proposed strongly acidic IER. Strongly acidic IER is composed of cross-linked polystyrene
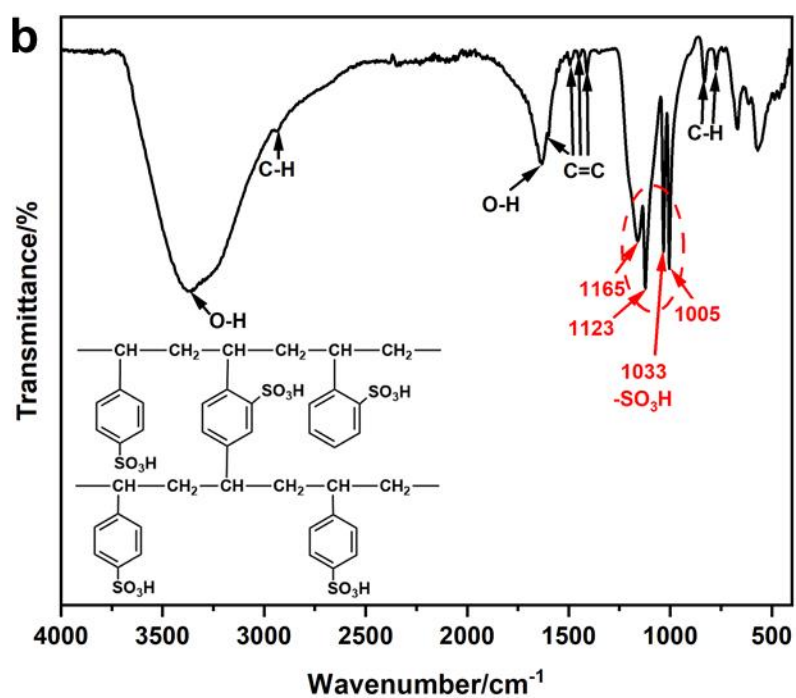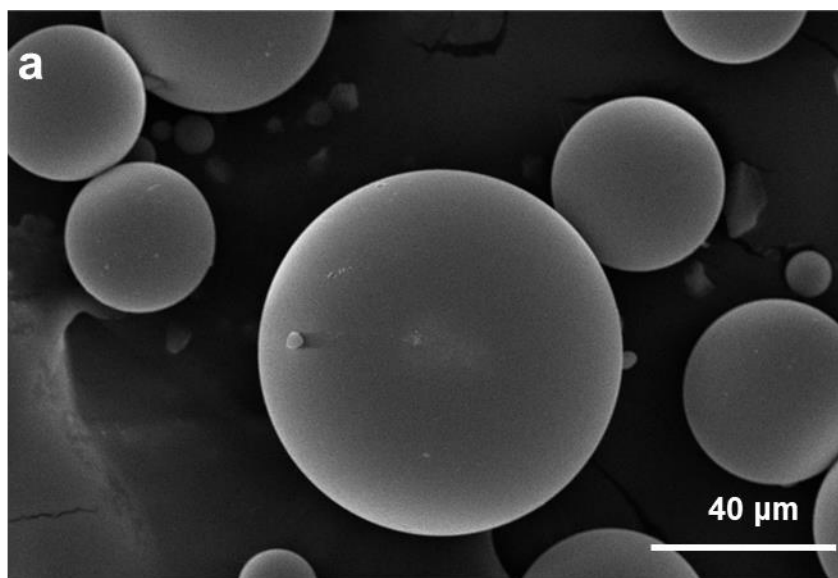
Figure 44. (a) SEM image of the strongly acidic cation exchange resin. (b) FT-IR spectrum of the strongly acidic cation exchange resin.

matrix and sulphonate ($-SO_3^-$) functional groups which are charged with protons[73]. According to reported research[75,76], the peaks around 3370 cm^{-1} and 2925 cm^{-1} are assigned to O-H stretching vibrations in H_2O (the moisture in ion exchange resin) and C-H stretching vibrations, respectively; the peak around 1634 cm^{-1} is ascribed to O-H deformation vibrations; the 4 peaks at 1603 cm^{-1}, 1495 cm^{-1}, 1450 cm^{-1}, 1415 cm^{-1} are assigned to C=C vibrations of benzene rings; the $-SO_3H$ functional group is identified by the 4 peaks at around 1165 cm^{-1}, 1123 cm^{-1}, 1033 cm^{-1} and 1055 cm^{-1}; the two small peaks at 830 cm^{-1}, 774 cm^{-1} are from C-H out-of-plane deformation vibration. The presence of functional group ($-SO_3^-$) charged with protons can adsorb multi-valance cations such as Zn^{2+} ions and Mn^{2+} ions and release protons. More importantly, this process is reversible when the surrounding pH is low[74].

4.2 Design of Zn/IER/β-MnO₂ Swagelok-type Batteries

Therefore, a Swagelok-type battery containing strongly acidic ion exchange resin is proposed to regulate the proton distribution in the electrolyte. Fig. 45a shows the design of the Swagelok-type battery, 2 layers of absorbed glass mat separator containing 120 μL of H_2SO_4 (pH = 1) solution are selected as the electrolyte near cathode (or catholyte) to provide protons for conversion reaction ($MnO_2 \rightarrow MnOOH$) and dissolution reactions ($MnO_2 \rightarrow Mn^{2+}$). 1 layer of absorbed glass mat separator containing 60 μL of $ZnSO_4$ solution (2 M) is selected as the electrolyte near anode (or anolyte) to accomplish the reversible stripping/deposition of Zn anode. 0.1 g of ion exchange resin is weighed and simply pressed between the separator containing catholyte and the separator containing anolyte to exchange ions with the electrolytes (Fig. 45b) by a Swagelok electrode.
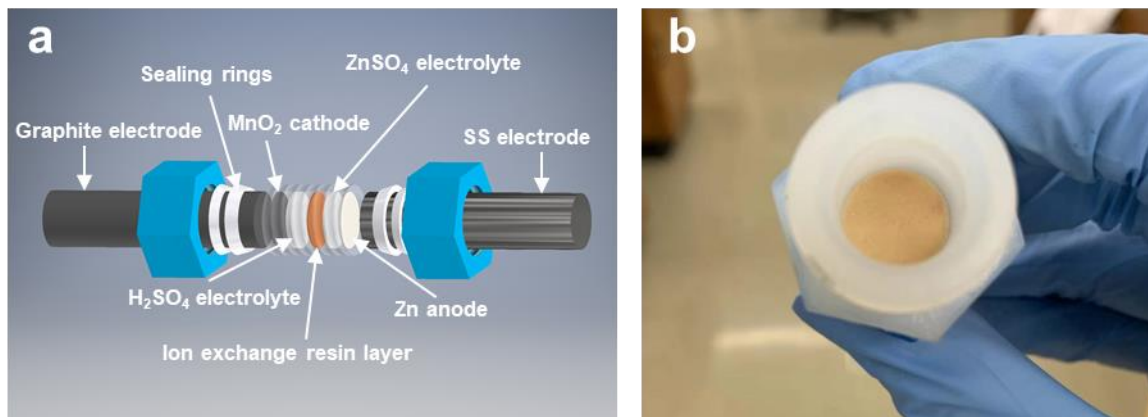
Figure 45. (a) Schematic illustration of the Swagelok-type cell containing ion exchange resin. (b) A picture of the coated ion exchange resin layer.

4.3 Material Characterization and Electrochemical Performance of Zn/IER/β-MnO$_2$ Swagelok-type Batteries

The assembled Swagelok-type battery is then galvanostatically tested under the current density of 50 mAg^{-1}. The electrochemical window is set from 1.0 V to 1.95 V due to its high open circuit voltage (Voc ~ 1.95 V). In this section, the material characterization of both IER and β-MnO$_2$ will be conducted and discussed. Also, the electrochemical performance of the Zn/IER/β-MnO$_2$ will be shown and compared with conventional Zn/MnO$_2$ battery (2M ZnSO$_4$ electrolyte system and 2M ZnSO$_4$ + 0.2 M MnSO$_4$ electrolyte system).

4.3.1 ICP-MS Study of the IER during Cycling

To verify the ability of IER to release and adsorb protons, IER at different voltages during discharge/charge process is collected and digested with HNO$_3$ for ICP-MS analysis. From the ICP-MS results (Fig. 46a), during discharge process, the IER adsorbs Mn^{2+} ions and
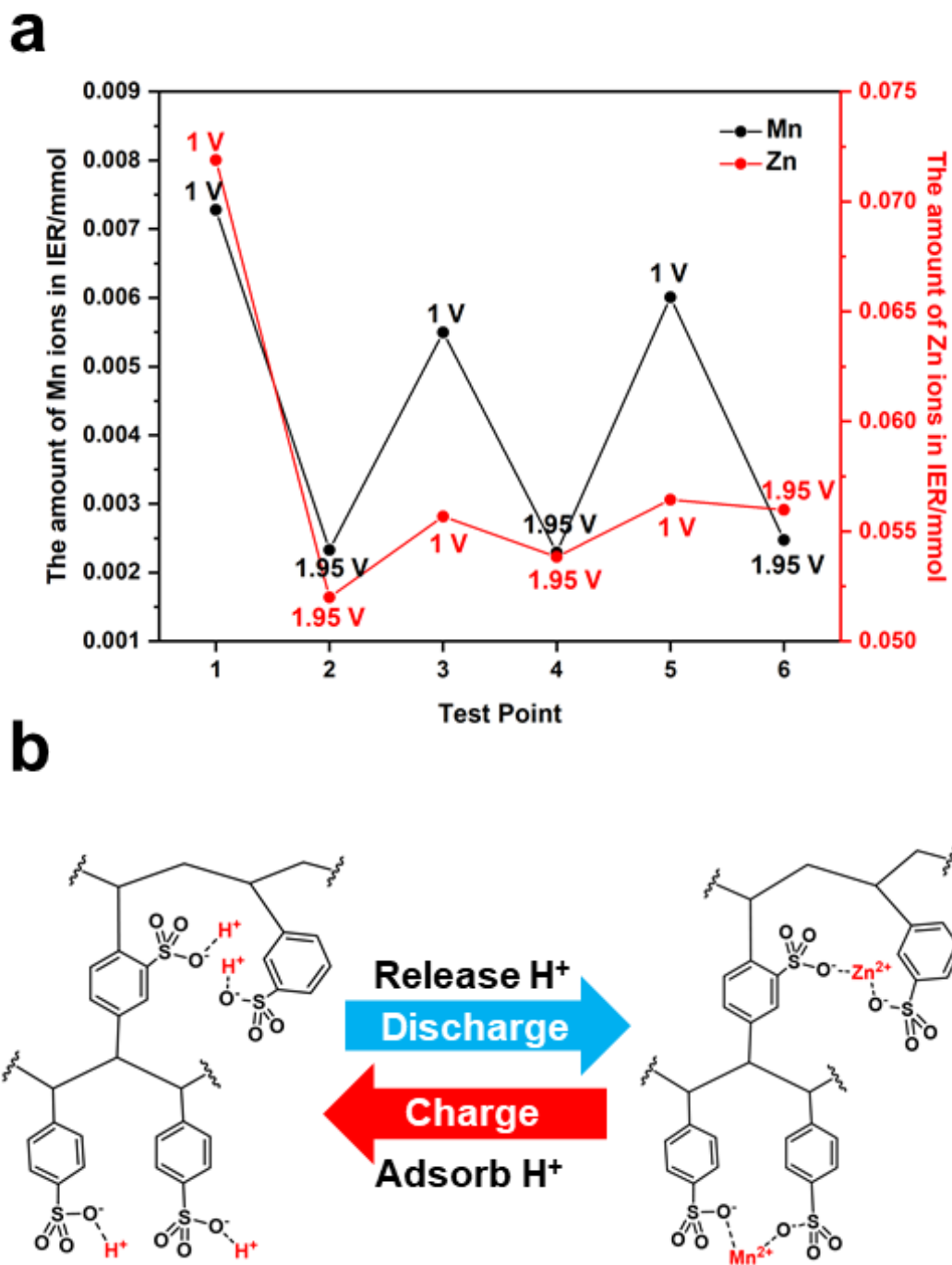
Figure 46. (a) The amount of Mn ions and Zn ions in the ion exchange resin during cycling. (b) Schematic illustration of IER releasing and adsorbing protons.

Zn^{2+} ions in the electrolyte, indicating the release of protons to the electrolyte; during charge process, the IER releases Mn^{2+} ions and Zn^{2+} ions to the electrolyte, indicating the adsorption of protons from the electrolyte. The ion exchange process is shown in Fig. 46b.

4.3.2 Ex-situ XRD Studies of the β-MnO₂ Cathode during Cycling

To further study the influence of IER on ZHS growth, ex-situ XRD of the β-MnO₂ cathode is performed. Fig. 47a shows the discharge/charge profile with selected voltages for ex-situ XRD, and Fig. 47b shows the diffraction patterns. After the battery is discharged to 1.325V, diffraction peaks from ZHS cannot be detected by the XRD. This is caused by the acidic catholyte (H_2SO_4) and proton-releasing IER. After the battery is fully discharged (1 V), similar as β-MnO₂ in 2 M $ZnSO_4$ electrolyte, diffraction peaks of ZHS generate on the cathode. However, after further charged to 1.55 V, the diffraction peaks disappear, demonstrating that the generated ZHS during discharge is much less than that in 2 M $ZnSO_4$ electrolyte. As a result, when the conversion reaction and dissolution reaction reversibly happens during charge process, the protons released are enough for dissolving all the generated ZHS. Since 1.55 V is a critical voltage where the irreversible reaction between ZHS and Mn^{2+} can happen, the elimination of ZHS can strongly avoid the generation of ZMO aggregations. Then, during the further charge-discharge process, ZHS cannot be detected until the voltage reaches 1 V. This result significantly proves the function of IER in Zn/β-MnO₂ battery.
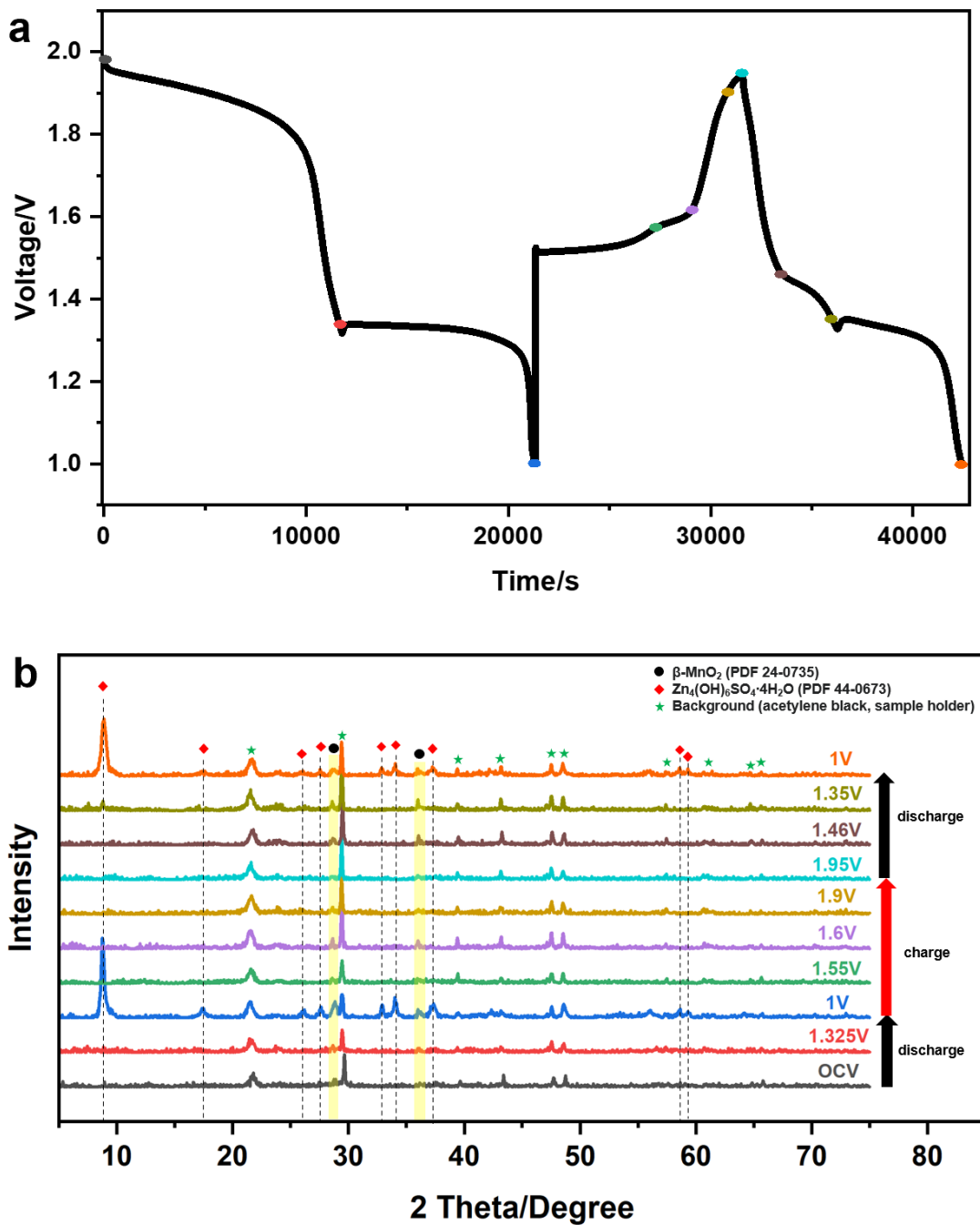
Figure 47. (a) Discharge/charge profile for first 2 cycles of Zn/β-MnO₂ battery in ZnSO₄/IER/H₂SO₄ electrolyte (1 V - 1.9 V, 50 mAg⁻¹) and chosen states for ex-situ XRD. (b) Ex-situ XRD of the cathode during first 2 cycles.

4.3.3 SEM Studies of the β-MnO₂ Cathode during the First 2 Cycles

To verify the ex-situ XRD results and observe the morphology evolution of the cathode material, SEM images are taken for the cathode during first 2 cycles. As shown in Fig. 48a,
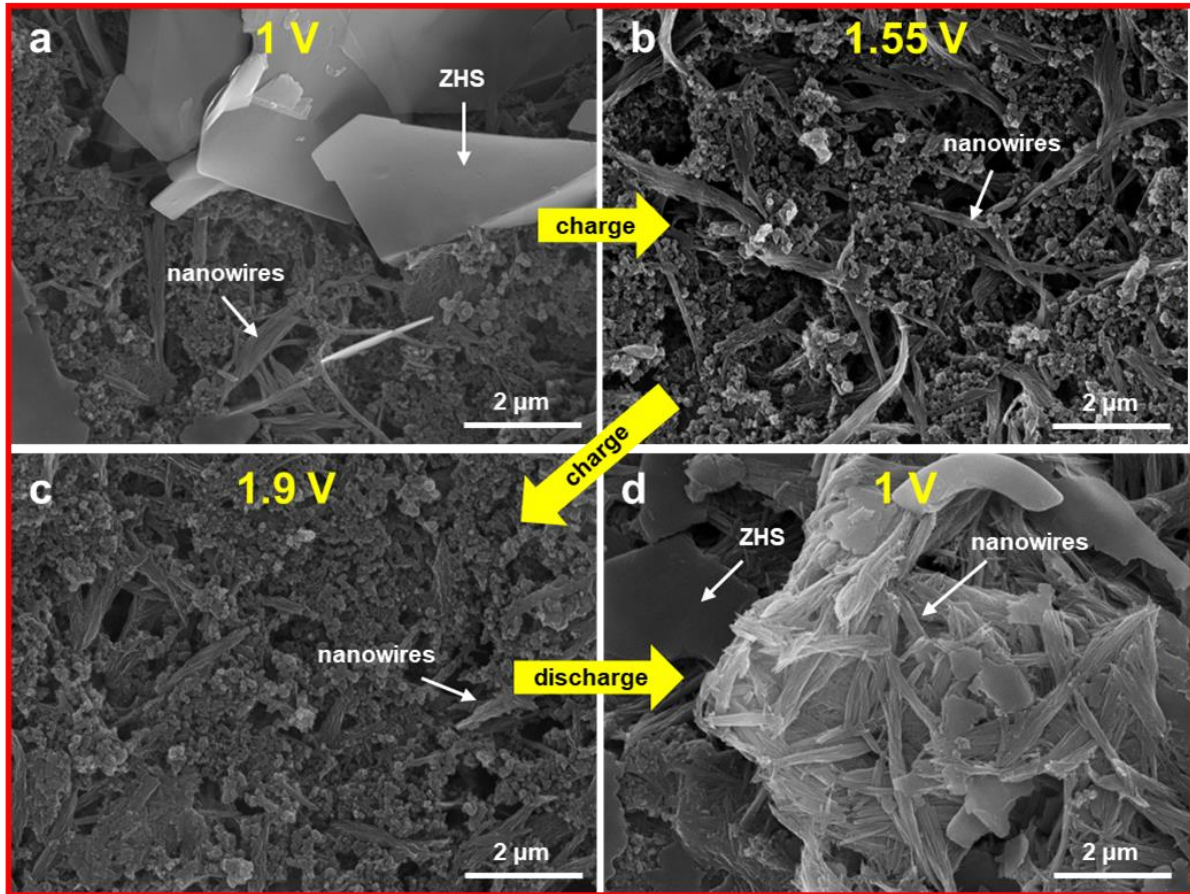
Figure 48. SEM images of β-MnO₂ Cathode in ZnSO₄/IER/H₂SO₄ electrolyte when (a) discharged to 1 V at the 1ˢᵗ cycle, (b) charged to 1.55 V at 2ⁿᵈ cycle, (c) charged to 1.9 V at 2ⁿᵈ cycle, (d) discharged to 1 V at 2ⁿᵈ cycle.

after the battery is fully discharged, ZHS nanoflakes generate on the surface of nanowires. Importantly, after the battery is charged to 1.55 V (Fig. 48b), no ZHS nanoflakes can be detected, which strongly agrees with the ex-situ XRD results. Therefore, the irreversible

reaction cannot happen due to the lack of reactant, and no ZMO aggregations can be detected when the battery is fully charged. Furthermore, the battery is discharged back to 1 V, showing intact nanowires with some ZHS flakes.

4.3.4 Electrochemical Impedance of the Proposed Zn/IER/β-MnO₂ Battery during Charge Process

To obtain the electrochemical impedance, especially the charge-transfer resistance, EIS is performed for the proposed Zn/IER/β-MnO₂ battery during charge process. Fig. 49a shows the comparison between the proposed Zn/IER/β-MnO₂ battery and Zn/β-MnO₂ battery with 2 M ZnSO₄ electrolyte. Simply from the comparison, the radius of the half-circle for the battery with IER is much smaller than that for the battery in 2 M ZnSO₄ electrolyte, demonstrating that the battery with IER has much smaller charge-transfer resistance than the battery in 2 M ZnSO₄ electrolyte. From the detailed fitting results with corresponding equivalent circuits (Fig. 49b-d and Table 6), Zn/β-MnO₂ battery in the proposed ZnSO₄/IER/H₂SO₄ electrolyte shows significant small charge-transfer resistance ($<10\ \Omega$), which is around 50 times smaller than that in 2 M ZnSO₄ electrolyte. Also, even after the battery with IER is fully charged to 1.95 V, the change of charge-transfer resistance is negligible ($5.44\ \Omega$ to $9.95\ \Omega$). This can be ascribed to the elimination of side products ZHS and ZMO during charge process.

Table 6. The detailed EIS fitting results of Zn/IER/β-MnO₂ battery during charge process.

Sample Details	Re/Ohm	Rct/Ohm	CPE-T	CPE-P	Zw-R/Ohm	Zw-T	Zw-P
IER-1.5 V	22.25	5.438	0.0017919	0.82332	203.2	2.081	0.51323
IER-1.55 V	22.06	2.065	0.018021	0.60343	24.09	4.611	0.27334
IER-1.95 V	21.87	9.95	0.0064795	0.56966	35.88	8.698	0.31967

71
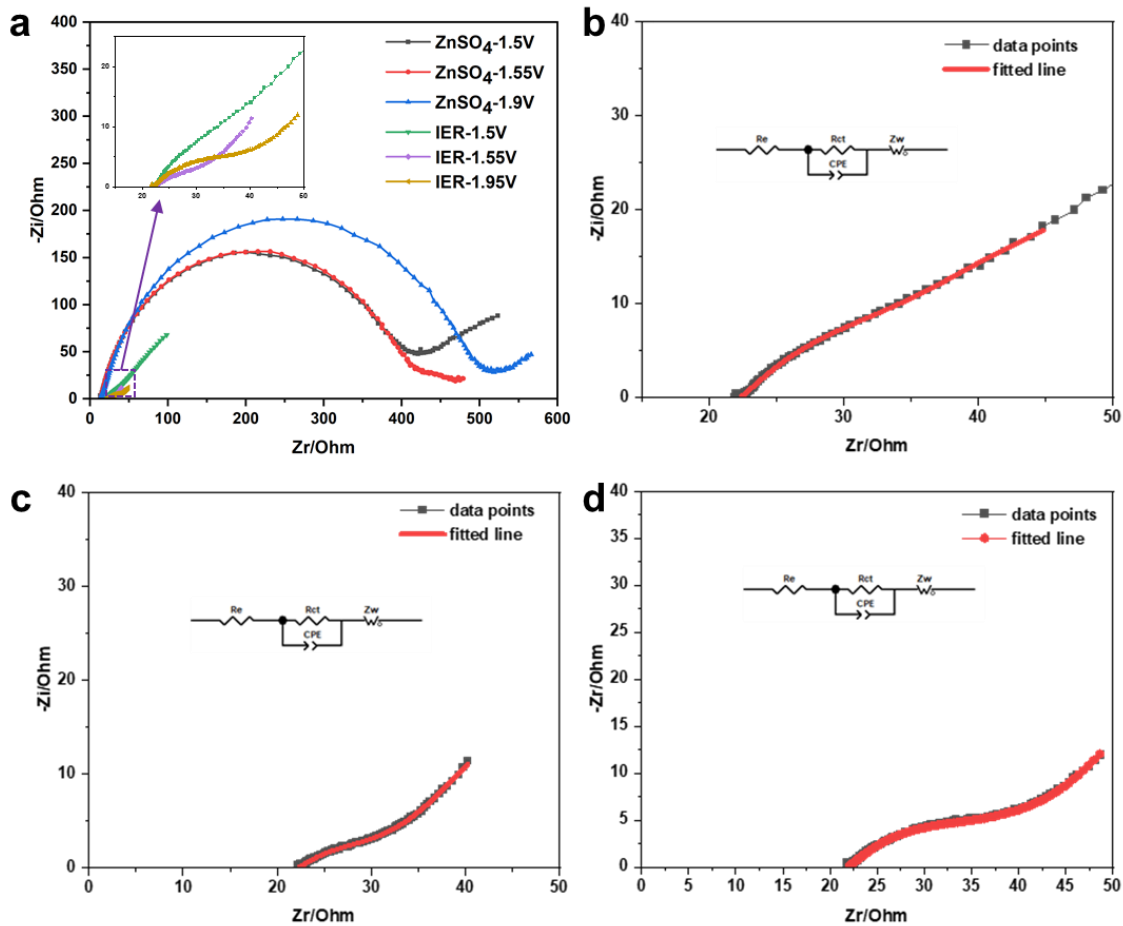
Figure 49. (a) A comparison between EIS results of the battery in ZnSO₄ electrolyte and ZnSO₄/IER/H₂SO₄ electrolyte during charge process. Detailed EIS fitting results of the Zn/IER/β-MnO₂ battery during charge process at (b) 1.5 V, (c) 1.55 V, (d) 1.95 V.

4.3.5 Galvanostatic Test of the Designed Zn/IER/β-MnO$_2$ Battery

The cyclability of the Zn/β-MnO$_2$ batteries in 2 M ZnSO$_4$ electrolyte system and ZnSO$_4$/IER/H$_2$SO$_4$ electrolyte system is shown in Fig. 50a. At a low current density of 50 mAg^{-1}, the proposed Zn/β-MnO$_2$ battery with IER can provide a reversible specific capacity of 170 mAhg^{-1} over 200 cycles, corresponding to continuous discharge/charge for above 1450 hours. The capacity retention of Zn/β-MnO$_2$ battery with IER after 200 cycles is ~85% and ~83% higher than that of β- Zn/MnO$_2$ battery in 2 M ZnSO$_4$ electrolyte and 2 M ZnSO$_4$ + 0.2 M MnSO$_4$ electrolyte, respectively. Also, the columbic efficiency of the Zn/β-MnO$_2$ battery in ZnSO$_4$/IER/H$_2$SO$_4$ electrolyte is improved to be ~99.84%, while the columbic efficiency of the Zn/β-MnO$_2$ battery in 2 M ZnSO$_4$ electrolyte and 2 M ZnSO$_4$ + 0.2 M MnSO$_4$ electrolyte is only 98.74% and 98.84%, respectively. The discharge/charge profile for 3rd cycle, 30th cycle, 200th cycle of Zn/β-MnO$_2$ batteries in ZnSO$_4$/IER/H$_2$SO$_4$ electrolyte system is shown in Fig. 50b. Compared with 2 M ZnSO$_4$ electrolyte system, the use of ZnSO$_4$/IER/H$_2$SO$_4$ electrolyte system stabilizes the 2nd discharge plateau (from 1.35 V to 1.2 V); even after 200 cycles, the 2nd discharge plateau does not experience obvious attenuation.
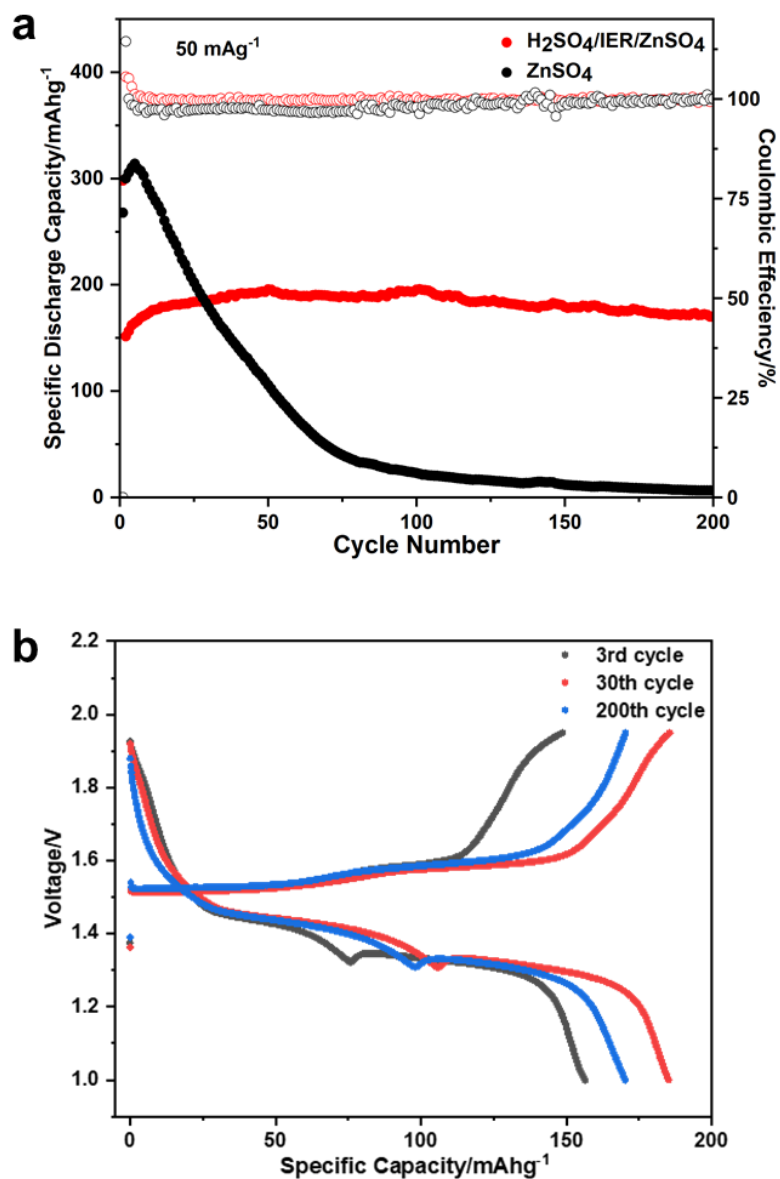
Figure 50. (a) Cycling performance of Zn/β-MnO₂ batteries in 2 M ZnSO₄ electrolyte system (1 V – 1.9 V, 50 mAg⁻¹) and ZnSO₄/IER/H₂SO₄ electrolyte system (1 V - 1.95 V, mAg⁻¹). (b) Discharge/charge profile for 3rd cycle, 30th cycle, 200th cycle of Zn/β-MnO₂ batteries in ZnSO₄/IER/H₂SO₄ electrolyte system (1 V - 1.95 V, 50 mAg⁻¹).

4.3.6 Morphology Overview during Long-term Cycling

To have an overlook of morphology change during long-term cycling, SEM images of the cathode materials before cycling and after 50 cycles are taken and shown in Fig. 51.
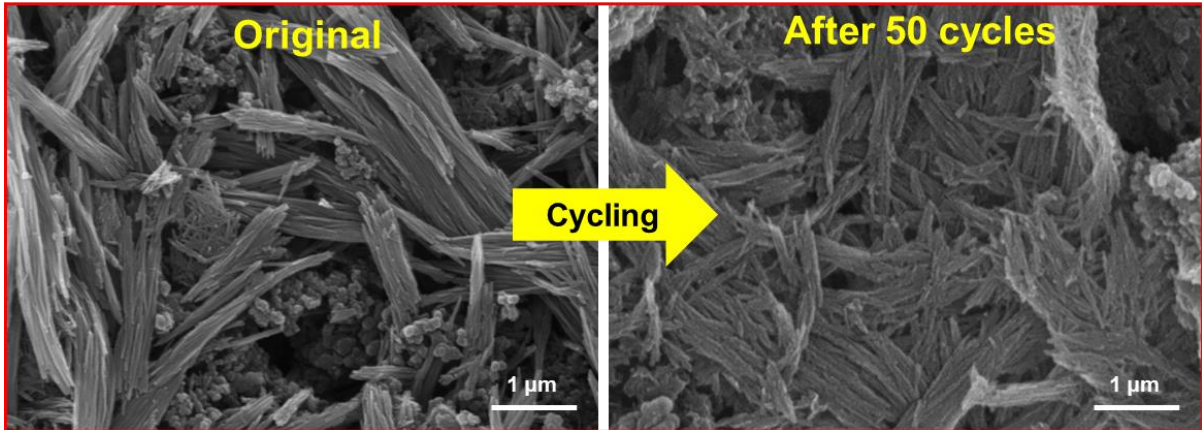
Figure 51. A comparison of SEM images of cathode materials before cycling and after 50 cycles in ZnSO$_4$/IER/H$_2$SO$_4$ electrolyte system (1 V - 1.95 V, 50 mAg^{-1}).

As clearly shown in the SEM images, from the original cathode to cathode after 50 cycles, no obvious morphology varieties are observed. The cathode is still composed of nanowires and no irregular aggregations are detected, which demonstrates the high reversibility of Zn/β-MnO$_2$ batteries in ZnSO$_4$/IER/H$_2$SO$_4$ electrolyte system.

4.3.7 Lifespan Comparison between the proposed Zn/IER/β-MnO$_2$ Battery and Other Reported Zn/MnO$_2$ Batteries

To compare this work with other recently reported aqueous rechargeable Zn/MnO$_2$ batteries, information from other literatures including current density, maximum capacity, and cycle number is collected. Hence, the lifespan range can be calculated and compared with this

work. Table 7 shows the detailed comparison and calculations, and Fig. 52 is a plot with maximum lifespan as y-axis.

Table 7. A detailed comparison between this work and other literatures (2018-2021).

Current Density/Ag^{-1}	Maximum Capacity/mAhg^{-1}; retention	Cycle Number	Lifespan/hours	reference
4	121; 95%	4000	230-242	22
0.3	382; 95%	100	242-255	34
0.6	388; 88%	500	568-647	40
0.2	293; 99%	160	464-469	42
1.848	200; 98%	3000	636-649	47
0.1	256; 100%	50	256	77
0.3	130; 100%	400	347	78
0.7	203; 89%	600	309-348	79
3.08	100; 93%	2000	121-130	80
0.05	195; 87%	200	1450	This work

(Note: The calculations of lifespan ranges (in hours) are shown as followed:

maximum value of lifespan = 2 × maximum capacity/current density × cycle number;

minimum value of lifespan = 2 × minimum capacity/current density × cycle number.)
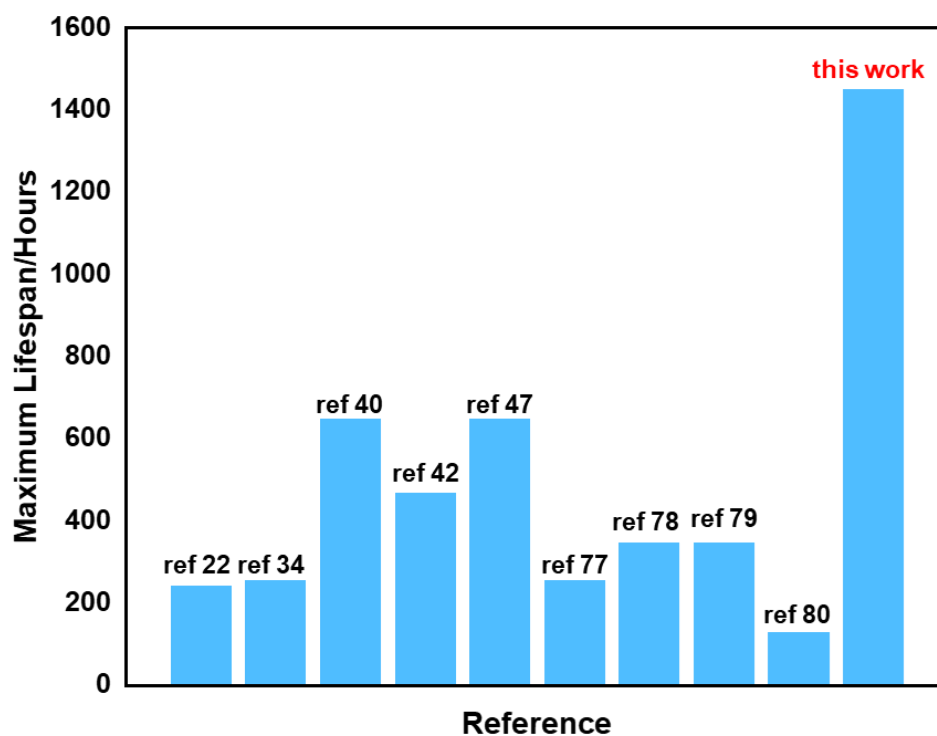
Figure 52. A comparison of maximum lifespan between other rechargeable aqueous Zn/MnO₂ batteries reported during 2018-2021 and this work.

4.3.8 Reaction Mechanisms of the Proposed Zn/IER/β-MnO₂ Battery

The reaction mechanisms of the proposed Zn/MnO₂ battery with IER are shown by the schematic diagram (Fig. 53). As mentioned in section 3.1, protons can insert into the tunnel structure of β-MnO₂ to promotes the conversion reaction ($MnO_2 \rightarrow MnOOH$) and the dissolution reaction ($MnO_2 \rightarrow Mn^{2+}$) during discharge process. The consumption of protons increases the pH of the electrolyte, which forms ZHS in 2 M ZnSO₄ electrolyte. When the
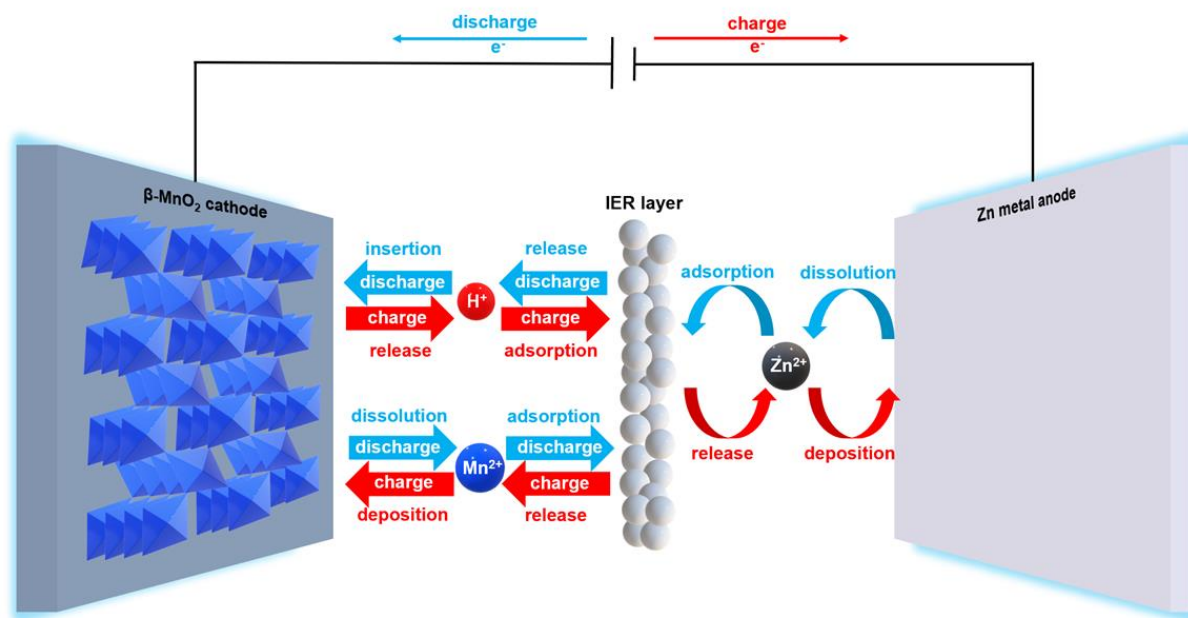
Figure 53. Schematic energy storage mechanisms for the proposed Zn/β-MnO₂ battery with ZnSO₄/IER/H₂SO₄ electrolyte.

ZnSO₄/IER/H₂SO₄ electrolytes are introduced into the system, the increased pH and increased number of multivalent cations (Zn^{2+}, Mn^{2+}) in the electrolytes can cause the adsorption of multivalent cations (Zn^{2+}, Mn^{2+}) and release of protons. These protons can buffer the pH in the electrolyte and reduce the amount of ZHS generated. In this case, after the battery is further charged to 1.55 V where it undergoes part of the conversion reaction (MnOOH → MnO₂), the generated ZHS is completely removed, and the irreversible reaction which forms ZMO aggregations is inhibited due to the lack of reactants. Importantly, after the battery is further charged, the completion of conversion reaction (MnOOH → MnO₂) and deposition reaction (Mn^{2+} → MnO₂) causes the reduction of pH in the electrolytes and the concentration of multivalent cations (Zn^{2+}, Mn^{2+}) in the electrolytes. Consequently, the IER is regenerated by

78

adsorbing protons in the electrolytes and release multivalent cations (Zn^{2+}, Mn^{2+}), which ensures that IER can sustainably provide protons during discharge process.

4.4 Conclusions

As a conclusion, because the capacity loss is caused by a gradual phase transformation from MnO_2 into lowly crystallized aggregations, which is initiated from an irreversible reaction between Mn^{2+} ions and ZHS during charge process, strategy regarding to regulating proton distribution is proposed via introducing an IER layer between the catholyte (H_2SO_4) and the anolyte ($ZnSO_4$). The use of strongly acidic cation exchange resin successfully suppresses the growth of ZHS and hence inhibits the irreversible reaction. Specifically, the sulphonate groups in the ion exchange resin adsorbs Zn^{2+} ions as well as Mn^{2+} ions and release protons during discharge process; moreover, they release Zn^{2+} ions as well as Mn^{2+} ions and adsorb protons during charge process. The reversible ion exchange process realizes the regulation of proton distribution in the electrolyte and eliminates ZHS when the battery is charged over 1.55 V where the irreversible reaction happens. Therefore, the irreversible reaction which generates ZMO aggregations is inhibited due to the lack of reactants, and the Zn/MnO_2 battery achieves a high reversibility. At the current density of 50 mAg^{-1}, the capacity retention of Zn/β-MnO_2 battery with IER after 200 cycles (> 1450 hours continuous discharging/charging) is ~85% and ~83% higher than that of Zn/β-MnO_2 battery in 2 M $ZnSO_4$ electrolyte and 2 M $ZnSO_4$ + 0.2 M $MnSO_4$ electrolyte, respectively. Moreover, the average coulombic efficiency is improved from ~98.74% (2 M $ZnSO_4$ electrolyte) or ~98.84% (2 M $ZnSO_4$ + 0.2 M $MnSO_4$ electrolyte) to ~99.84%. Therefore, besides pre-adding Mn^{2+} ions in the electrolyte, we expect that

regulating proton distribution is a promising and efficient method to improve the cyclability of

Zn/MnO$_2$ battery.

Chapter 5: Summary of The Thesis and Recommended Future Work

In Chapter 1, the history of rechargeable batteries are firstly introduced. From the 1st generation of rechargeable batteries (lead-acid batteries) to the most updated lithium-ion batteries, the performance of rechargeable batteries is significantly improved, regarding to improved energy density and enhanced cycling performance. However, the safety issue of lithium-ion batteries urges researchers to find the next-generation batteries. Aqueous rechargeable zinc ion battery (ARZIB) is a promising candidate of the next-generation batteries because of its superior safety (aqueous electrolyte) and huge potential (high capacity of Zn metal and relatively low reduction potential). In ARZIBs, seeking for a proper cathode material is the most important project. MnO_2, as a low cost, nontoxic, and high theoretical capacity material, attracts much attention from researchers, which also motivates us to do research on MnO_2 cathode. However, $Zn-MnO_2$ batteries still suffer from many issues. The issues are mainly focused on the unclear energy storage mechanism, the controversial topics on the widely used Mn^{2+} additives, and the low cycling performance under small current density. These are also questions that we are committed to address in this thesis.

Chapter 2 is a brief introduction to all material characterization techniques and electrochemical methods used in this thesis. Basically, their working principles and specifications are introduced.

Chapter 3 is the critical discovery on the mechanism of $Zn-MnO_2$ batteries. Basically, it is demonstrated that the dissolution reaction happening during discharge process is practically the major reaction in $Zn-MnO_2$ batteries, which is different from previous reports

considering dissolution as side reaction. More importantly, the dissolution reaction itself is actually not the reason for capacity fading. The side products ZHS and dissolved Mn^{2+} ions are the root causes of irreversibility. During charge process, these two side products can react to form ZMO irregular aggregations, which not only increases the charge-transfer resistance in the whole battery, but also causes irreversible phase conversion.

Based on the mechanisms, Chapter 4 gives an efficient solution. Considering Mn dissolution is difficult to suppress, the main work is on controlling/regulating proton distribution to suppress the growth of the other side product, ZHS. Interestingly, when strongly acidic IER is applied in the battery, pH can be practically regulated, and ZHS is eliminated at the critical voltage where the irreversible reaction happens. Therefore, the proposed battery with IER layer achieves much higher capacity retention than the battery with conventional $ZnSO_4$ electrolyte and the battery with Mn^{2+} additives. Since the adopted current density in this thesis is much lower than that in most mainstream literatures and the cycle number is considerable, it is believed that regulating proton concentration is an efficient method to improve cycling performance in Zn/MnO_2 batteries.

It is strongly suggested that the future work of Zn/MnO_2 should be committed to regulate the proton distribution/concentration in the electrolyte. Many chemicals containing sulfonic group are worth trying, such as sulfanilic acid and methanesulfonic acid. Also, based on the battery design in this work, different types of strongly acidic cation exchange resin can be tried.

References

(1)   The role of renewable energy in the global energy transformation | Elsevier Enhanced Reader https://reader.elsevier.com/reader/sd/pii/S2211467X19300082?token=A2BDEC32166FED01 53F29DBA822F72472800CB9A857F8ECB93F65D747DA0C0F83C9530268B7B6CF69D6 C1AA9BBF2F252&originRegion=us-east-1&originCreation=20211022201044 (accessed 2021 -10 -22). https://doi.org/10.1016/j.esr.2019.01.006.

(2)   Chen, H.; Cong, T. N.; Yang, W.; Tan, C.; Li, Y.; Ding, Y. Progress in Electrical Energy Storage System: A Critical Review. *Prog. Nat. Sci.* **2009**, *19* (3), 291–312. https://doi.org/10.1016/j.pnsc.2008.07.014.

(3)   Hossain, E.; Faruque, H. M. R.; Sunny, M. S. H.; Mohammad, N.; Nawar, N. A Comprehensive Review on Energy Storage Systems: Types, Comparison, Current Scenario, Applications, Barriers, and Potential Solutions, Policies, and Future Prospects. *Energies* **2020**, *13* (14), 3651. https://doi.org/10.3390/en13143651.

(4)   Garche, J. Advanced Battery Systems—the End of the Lead–Acid Battery? *Phys. Chem. Chem. Phys.* **2001**, *3* (3), 356–367. https://doi.org/10.1039/B005451H.

(5)   11. Nickel-Based Batteries: Materials and Chemistry - Knovel https://app-knovel-com.proxy.lib.uwaterloo.ca/web/view/khtml/show.v/rcid:kpETDSS005/cid:kt00C52L38/vie werType:khtml/root_slug:electricity-transmission/url_slug:nickel-based-batteries?&kpromoter=federation&b-toc-cid=kpETDSS005&b-toc-url-slug=introduction-transmission&b-toc-title=f&page=2&view=collapsed&zoom=1 (accessed 2021 -10 -22).

(6)   Mossali, E.; Picone, N.; Gentilini, L.; Rodrìguez, O.; Pérez, J. M.; Colledani, M. Lithium-Ion Batteries towards Circular Economy: A Literature Review of Opportunities and Issues of Recycling Treatments. *J. Environ. Manage.* **2020**, *264*, 110500. https://doi.org/10.1016/j.jenvman.2020.110500.

(7)   Li, W.; Song, B.; Manthiram, A. High-Voltage Positive Electrode Materials for Lithium-Ion Batteries. *Chem. Soc. Rev.* **2017**, *46* (10), 3006–3059. https://doi.org/10.1039/C6CS00875E.

(8)   Bratsch, S. G. Standard Electrode Potentials and Temperature Coefficients in Water at 298.15 K. *J. Phys. Chem. Ref. Data* **1989**, *18* (1), 1–21. https://doi.org/10.1063/1.555839.

(9)   Chawla, N.; Bharti, N.; Singh, S. Recent Advances in Non-Flammable Electrolytes for Safer Lithium-Ion Batteries. *Batteries* **2019**, *5*. https://doi.org/10.3390/batteries5010019.

(10)   Song, M.; Tan, H.; Chao, D.; Fan, H. J. Recent Advances in Zn-Ion Batteries. *Adv. Funct. Mater.* **2018**, *28* (41), 1802564. https://doi.org/10.1002/adfm.201802564.

(11)   Wang, L.; Zheng, J. Recent Advances in Cathode Materials of Rechargeable Aqueous Zinc-Ion Batteries. *Mater. Today Adv.* **2020**, *7*, 100078. https://doi.org/10.1016/j.mtadv.2020.100078.

(12)   Liu, S.; Kang, L.; Kim, J. M.; Chun, Y. T.; Zhang, J.; Jun, S. C. Recent Advances in Vanadium-Based Aqueous Rechargeable Zinc-Ion Batteries. *Adv. Energy Mater.* **2020**, *10* (25), 2000477. https://doi.org/10.1002/aenm.202000477.

(13)   Ming, J.; Guo, J.; Xia, C.; Wang, W.; Alshareef, H. N. Zinc-Ion Batteries: Materials, Mechanisms, and Applications. *Mater. Sci. Eng. R Rep.* **2019**, *135*, 58–84. https://doi.org/10.1016/j.mser.2018.10.002.

(14)   Liu, Y.; Zhi, J.; Sedighi, M.; Han, M.; Shi, Q.; Wu, Y.; Chen, P. Mn2+ Ions Confined by Electrode Microskin for Aqueous Battery beyond Intercalation Capacity. *Adv. Energy Mater.* **2020**, *10* (42), 2002578. https://doi.org/10.1002/aenm.202002578.

(15)   Shoji, T.; Hishinuma, M.; Yamamoto, T. Zinc-Manganese Dioxide Galvanic Cell Using Zinc Sulphate as Electrolyte. Rechargeability of the Cell. *J. Appl. Electrochem.* **1988**, *18* (4), 521–526. https://doi.org/10.1007/BF01022245.

(16)   Julien, C. M.; Mauger, A. Nanostructured MnO2 as Electrode Materials for Energy Storage. *Nanomaterials* **2017**, *7* (11), 396. https://doi.org/10.3390/nano7110396.

(17)   Post, J. E. Manganese Oxide Minerals: Crystal Structures and Economic and Environmental Significance. *Proc. Natl. Acad. Sci.* **1999**, *96* (7), 3447–3454. https://doi.org/10.1073/pnas.96.7.3447.

(18)   Shin, J.; Seo, J. K.; Yaylian, R.; Huang, A.; Meng, Y. S. A Review on Mechanistic Understanding of MnO2 in Aqueous Electrolyte for Electrical Energy Storage Systems. *Int. Mater. Rev.* **2020**, *65* (6), 356–387. https://doi.org/10.1080/09506608.2019.1653520.

(19)   Mao, J.; Wu, F.-F.; Shi, W.-H.; Liu, W.-X.; Xu, X.-L.; Cai, G.-F.; Li, Y.-W.; Cao, X.-H. Preparation of Polyaniline-Coated Composite Aerogel of MnO2 and Reduced Graphene Oxide for High-Performance Zinc-Ion Battery. *Chin. J. Polym. Sci.* **2020**, *38* (5), 514–521. https://doi.org/10.1007/s10118-020-2353-6.

(20)   Guo, C.; Tian, S.; Chen, B.; Liu, H.; Li, J. Constructing A-MnO2@PPy Core-Shell Nanorods towards Enhancing Electrochemical Behaviors in Aqueous Zinc Ion Battery. *Mater. Lett.* **2020**, *262*, 127180. https://doi.org/10.1016/j.matlet.2019.127180.

(21)   Cao, J.; Zhang, D.; Zhang, X.; Wang, S.; Han, J.; Zhao, Y.; Huang, Y.; Qin, J. Mechanochemical Reactions of MnO2 and Graphite Nanosheets as a Durable Zinc Ion Battery Cathode. *Appl. Surf. Sci.* **2020**, *534*, 147630. https://doi.org/10.1016/j.apsusc.2020.147630.

(22)   Jiang, W.; Xu, X.; Liu, Y.; Tan, L.; Zhou, F.; Xu, Z.; Hu, R. Facile Plasma Treated β-MnO2@C Hybrids for Durable Cycling Cathodes in Aqueous Zn-Ion Batteries. *J. Alloys Compd.* **2020**, *827*, 154273. https://doi.org/10.1016/j.jallcom.2020.154273.

(23)   Wang, K.; Zhang, X.; Han, J.; Zhang, X.; Sun, X.; Li, C.; Liu, W.; Li, Q.; Ma, Y. High-Performance Cable-Type Flexible Rechargeable Zn Battery Based on MnO2@CNT Fiber Microelectrode. *ACS Appl. Mater. Interfaces* **2018**, *10* (29), 24573–24582. https://doi.org/10.1021/acsami.8b07756.

(24)   Pan, H.; Shao, Y.; Yan, P.; Cheng, Y.; Han, K. S.; Nie, Z.; Wang, C.; Yang, J.; Li, X.; Bhattacharya, P.; Mueller, K. T.; Liu, J. Reversible Aqueous Zinc/Manganese Oxide Energy

Storage from Conversion Reactions. *Nat. Energy* **2016**, *1* (5), 1–7. https://doi.org/10.1038/nenergy.2016.39.

(25)   Jin, Y.; Zou, L.; Liu, L.; Engelhard, M. H.; Patel, R. L.; Nie, Z.; Han, K. S.; Shao, Y.; Wang, C.; Zhu, J.; Pan, H.; Liu, J. Joint Charge Storage for High-Rate Aqueous Zinc–Manganese Dioxide Batteries. *Adv. Mater.* **2019**, *31* (29), 1900567. https://doi.org/10.1002/adma.201900567.

(26)   Zeng, Y.; Zhang, X.; Meng, Y.; Yu, M.; Yi, J.; Wu, Y.; Lu, X.; Tong, Y. Achieving Ultrahigh Energy Density and Long Durability in a Flexible Rechargeable Quasi-Solid-State Zn–MnO2 Battery. *Adv. Mater.* **2017**, *29* (26), 1700274. https://doi.org/10.1002/adma.201700274.

(27)   Zhang, N.; Cheng, F.; Liu, J.; Wang, L.; Long, X.; Liu, X.; Li, F.; Chen, J. Rechargeable Aqueous Zinc-Manganese Dioxide Batteries with High Energy and Power Densities. *Nat. Commun.* **2017**, *8* (1), 405. https://doi.org/10.1038/s41467-017-00467-x.

(28)   Chen, H.; Kuang, H.; Liu, F.; Wu, Y.; Cai, S.; Xu, M.; Bao, S.-J. A Self-Healing Neutral Aqueous Rechargeable Zn/MnO2 Battery Based on Modified Carbon Nanotubes Substrate Cathode. *J. Colloid Interface Sci.* **2021**, *600*, 83–89. https://doi.org/10.1016/j.jcis.2021.04.097.

(29)   Wang, A.; Zhou, W.; Huang, A.; Chen, M.; Chen, J.; Tian, Q.; Xu, J. Modifying the Zn Anode with Carbon Black Coating and Nanofibrillated Cellulose Binder: A Strategy to Realize Dendrite-Free Zn-MnO2 Batteries. *J. Colloid Interface Sci.* **2020**, *577*, 256–264. https://doi.org/10.1016/j.jcis.2020.05.102.

(30)   Han, J.; Euchner, H.; Kuenzel, M.; Hosseini, S. M.; Groß, A.; Varzi, A.; Passerini, S. A Thin and Uniform Fluoride-Based Artificial Interphase for the Zinc Metal Anode Enabling Reversible Zn/MnO2 Batteries. *ACS Energy Lett.* **2021**, *6* (9), 3063–3071. https://doi.org/10.1021/acsenergylett.1c01249.

(31)   Wei, C.; Xu, C.; Li, B.; Du, H.; Kang, F. Preparation and Characterization of Manganese Dioxides with Nano-Sized Tunnel Structures for Zinc Ion Storage. *J. Phys. Chem. Solids* **2012**, *73* (12), 1487–1491. https://doi.org/10.1016/j.jpcs.2011.11.038.

(32)   Sun, W.; Wang, F.; Hou, S.; Yang, C.; Fan, X.; Ma, Z.; Gao, T.; Han, F.; Hu, R.; Zhu, M.; Wang, C. Zn/MnO2 Battery Chemistry With H+ and Zn2+ Coinsertion. *J. Am. Chem. Soc.* **2017**, *139* (29), 9775–9778. https://doi.org/10.1021/jacs.7b04471.

(33)   Lee, B.; Seo, H. R.; Lee, H. R.; Yoon, C. S.; Kim, J. H.; Chung, K. Y.; Cho, B. W.; Oh, S. H. Critical Role of PH Evolution of Electrolyte in the Reaction Mechanism for Rechargeable Zinc Batteries. *ChemSusChem* **2016**, *9* (20), 2948–2956. https://doi.org/10.1002/cssc.201600702.

(34)   Interfacial chemical binding and improved kinetics assisting stable aqueous Zn–MnO2 batteries - ScienceDirect https://www.sciencedirect.com/science/article/pii/S2468606920300940?casa_token=OCawTw-TFbIAAAAA:rbYuupaWXISjil9MJqUqHLnbgLbkuMZwOFfCvBgxNcioXW4bFHrYZ3PO_W5_n6z6At2B-zymxg01 (accessed 2021 -10 -23).

(35)   Moon, H.; Ha, K.-H.; Park, Y.; Lee, J.; Kwon, M.-S.; Lim, J.; Lee, M.-H.; Kim, D.-H.; Choi, J. H.; Choi, J.-H.; Lee, K. T. Direct Proof of the Reversible Dissolution/Deposition of Mn2+/Mn4+ for Mild-Acid Zn-MnO2 Batteries with Porous Carbon Interlayers. *Adv. Sci.* **2021**, *8* (6), 2003714. https://doi.org/10.1002/advs.202003714.

(36)   Li, G.; Chen, W.; Zhang, H.; Gong, Y.; Shi, F.; Wang, J.; Zhang, R.; Chen, G.; Jin, Y.; Wu, T.; Tang, Z.; Cui, Y. Membrane-Free Zn/MnO2 Flow Battery for Large-Scale Energy Storage. *Adv. Energy Mater.* **2020**, *10* (9), 1902085. https://doi.org/10.1002/aenm.201902085.

(37)   Chao, D.; Zhou, W.; Ye, C.; Zhang, Q.; Chen, Y.; Gu, L.; Davey, K.; Qiao, S.-Z. An Electrolytic Zn–MnO2 Battery for High-Voltage and Scalable Energy Storage. *Angew. Chem. Int. Ed.* **2019**, *58* (23), 7823–7828. https://doi.org/10.1002/anie.201904174.

(38)   Qiu, C.; Zhu, X.; Xue, L.; Ni, M.; Zhao, Y.; Liu, B.; Xia, H. The Function of Mn2+ Additive in Aqueous Electrolyte for Zn/δ-MnO2 Battery. *Electrochimica Acta* **2020**, *351*, 136445. https://doi.org/10.1016/j.electacta.2020.136445.

(39)   Zhang, X.; Wu, S.; Deng, S.; Wu, W.; Zeng, Y.; Xia, X.; Pan, G.; Tong, Y.; Lu, X. 3D CNTs Networks Enable MnO2 Cathodes with High Capacity and Superior Rate Capability for Flexible Rechargeable Zn–MnO2 Batteries. *Small Methods* **2019**, *3* (12), 1900525. https://doi.org/10.1002/smtd.201900525.

(40)   Zhao, Q.; Huang, X.; Zhou, M.; Ju, Z.; Sun, X.; Sun, Y.; Huang, Z.; Li, H.; Ma, T. Proton Insertion Promoted a Polyfurfural/MnO2 Nanocomposite Cathode for a Rechargeable Aqueous Zn–MnO2 Battery. *ACS Appl. Mater. Interfaces* **2020**, *12* (32), 36072–36081. https://doi.org/10.1021/acsami.0c08579.

(41)   Liu, M.; Zhao, Q.; Liu, H.; Yang, J.; Chen, X.; Yang, L.; Cui, Y.; Huang, W.; Zhao, W.; Song, A.; Wang, Y.; Ding, S.; Song, Y.; Qian, G.; Chen, H.; Pan, F. Tuning Phase Evolution of β-MnO2 during Microwave Hydrothermal Synthesis for High-Performance Aqueous Zn Ion Battery. *Nano Energy* **2019**, *64*, 103942. https://doi.org/10.1016/j.nanoen.2019.103942.

(42)   Wu, B.; Zhang, G.; Yan, M.; Xiong, T.; He, P.; He, L.; Xu, X.; Mai, L. Graphene Scroll-Coated α-MnO2 Nanowires as High-Performance Cathode Materials for Aqueous Zn-Ion Battery. *Small* **2018**, *14* (13), 1703850. https://doi.org/10.1002/smll.201703850.

(43)   Zhang, Y.; Deng, S.; Li, Y.; Liu, B.; Pan, G.; Liu, Q.; Wang, X.; Xia, X.; Tu, J. Anchoring MnO2 on Nitrogen-Doped Porous Carbon Nanosheets as Flexible Arrays Cathodes for Advanced Rechargeable Zn–MnO2 Batteries. *Energy Storage Mater.* **2020**, *29*, 52–59. https://doi.org/10.1016/j.ensm.2020.04.003.

(44)   Chen, X.; Li, W.; Zeng, Z.; Reed, D.; Li, X.; Liu, X. Engineering Stable Zn-MnO2 Batteries by Synergistic Stabilization between the Carbon Nanofiber Core and Birnessite-MnO2 Nanosheets Shell. *Chem. Eng. J.* **2021**, *405*, 126969. https://doi.org/10.1016/j.cej.2020.126969.

(45)   Tong, H.; Li, T.; Liu, J.; Gong, D.; Xiao, J.; Shen, L.; Ding, B.; Zhang, X. Fabrication of the Oxygen Vacancy Amorphous MnO2/Carbon Nanotube as Cathode for Advanced Aqueous Zinc-Ion Batteries. *Energy Technol.* **2021**, *9* (2), 2000769. https://doi.org/10.1002/ente.202000769.

(46)   Li, Y.; Wang, S.; Salvador, J. R.; Wu, J.; Liu, B.; Yang, W.; Yang, J.; Zhang, W.; Liu, J.; Yang, J. Reaction Mechanisms for Long-Life Rechargeable Zn/MnO2 Batteries. *Chem. Mater.* **2019**, *31* (6), 2036–2047. https://doi.org/10.1021/acs.chemmater.8b05093.

(47)   Liang, R.; Fu, J.; Deng, Y.-P.; Pei, Y.; Zhang, M.; Yu, A.; Chen, Z. Parasitic Electrodeposition in Zn-MnO2 Batteries and Its Suppression for Prolonged Cyclability. *Energy Storage Mater.* **2021**, *36*, 478–484. https://doi.org/10.1016/j.ensm.2020.12.015.

(48)   Yang, J.; Cao, J.; Peng, Y.; Yang, W.; Barg, S.; Liu, Z.; Kinloch, I. A.; Bissett, M. A.; Dryfe, R. A. W. Unravelling the Mechanism of Rechargeable Aqueous Zn–MnO2 Batteries: Implementation of Charging Process by Electrodeposition of MnO2. *Chemsuschem* **2020**, *13* (16), 4103–4110. https://doi.org/10.1002/cssc.202001216.

(49)   Bogner, A.; Jouneau, P.-H.; Thollet, G.; Basset, D.; Gauthier, C. A History of Scanning Electron Microscopy Developments: Towards "Wet-STEM" Imaging. *Micron* **2007**, *38* (4), 390–401. https://doi.org/10.1016/j.micron.2006.06.008.

(50)   Transmission Electron Microscopy: Fundamentals of Methods and Instrumentation. In *Electron Microscopy of Polymers*; Michler, G. H., Ed.; Springer Laboratory; Springer: Berlin, Heidelberg, 2008; pp 15–51. https://doi.org/10.1007/978-3-540-36352-1_3.

(51)   Zhou, W.; Apkarian, R. P.; Wang, Z. L.; Joy, D. Fundamentals of Scanning Electron Microscopy. 40.

(52)   Scanning Electron Microscopy (SEM). In *Electron Microscopy of Polymers*; Michler, G. H., Ed.; Springer Laboratory; Springer: Berlin, Heidelberg, 2008; pp 87–120. https://doi.org/10.1007/978-3-540-36352-1_5.

(53)   Nixon, W. C. The General Principles of Scanning Electron Microscopy. *Philos. Trans. R. Soc. Lond. B. Biol. Sci.* **1971**, *261* (837), 45–50.

(54)   Backscattered Electron - an overview | ScienceDirect Topics https://www.sciencedirect.com/topics/engineering/backscattered-electron (accessed 2021 -10 -26).

(55)   Shen, C.; Li, X.; Li, N.; Xie, K.; Wang, J.; Liu, X.; Wei, B. Graphene-Boosted, High-Performance Aqueous Zn-Ion Battery. *ACS Appl. Mater. Interfaces* **2018**, *10* (30), 25446–25453. https://doi.org/10.1021/acsami.8b07781.

(56)   Zuo, J. M.; Spence, J. C. H. *Advanced Transmission Electron Microscopy*; Springer New York: New York, NY, 2017. https://doi.org/10.1007/978-1-4939-6607-3.

(57)   Malla, P. B.; Komameni, S. High-Resolution Transmission Electron Microscopy (HRTEM) in the Study of Clays and Soils. In *Soil Restoration*; Lal, R., Stewart, B. A., Eds.; Stewart, B. A., Series Ed.; Advances in Soil Science; Springer New York: New York, NY, 1990; Vol. 17, pp 159–186. https://doi.org/10.1007/978-1-4612-3316-9_4.

(58)   Xu, W.; Wang, Y. Recent Progress on Zinc-Ion Rechargeable Batteries. *Nano-Micro Lett.* **2019**, *11* (1), 1–30. https://doi.org/10.1007/s40820-019-0322-9.

(59)   Shindo, D.; Oikawa, T. Energy Dispersive X-Ray Spectroscopy. In *Analytical Electron Microscopy for Materials Science*; Shindo, D., Oikawa, T., Eds.; Springer Japan: Tokyo, 2002; pp 81–102. https://doi.org/10.1007/978-4-431-66988-3_4.

(60)   Lou, S.; Liu, Y.; Yang, F.; lin, shuren; Zhang, R.; Deng, Y.; Wang, M.; Tom, K.; Zhou, F.; Ding, H.; Bustillo, K.; Wang, X.; Yan, S.; Scott, M.; Minor, A.; Yao, J. 3D Architecture Enabled by Strained 2D Material Heterojunction. *Nano Lett.* **2018**, *18*. https://doi.org/10.1021/acs.nanolett.7b05074.

(61)   Stanjek, H.; Häusler, W. Basics of X-Ray Diffraction. *Hyperfine Interact.* **2004**, *154* (1–4), 107–119. https://doi.org/10.1023/B:HYPE.0000032028.60546.38.

(62)   Ramachandran, V. S.; Beaudoin, J. J. *Handbook of Analytical Techniques in Concrete Science and Technology: Principles, Techniques and Applications*; Elsevier, 2000.

(63)   Fourier Transform Infrared Spectroscopy - an overview | ScienceDirect Topics https://www.sciencedirect.com/topics/engineering/fourier-transform-infrared-spectroscopy (accessed 2021 -10 -31).

(64)   Basalekou, M.; Pappas, C.; Tarantilis, P. A.; Kallithraka, S. Wine Authenticity and Traceability with the Use of FT-IR. *Beverages* **2020**, *6* (2), 30. https://doi.org/10.3390/beverages6020030.

(65)   Wilschefski, S. C.; Baxter, M. R. Inductively Coupled Plasma Mass Spectrometry: Introduction to Analytical Aspects. *Clin. Biochem. Rev.* **2019**, *40* (3), 115–133. https://doi.org/10.33176/AACB-19-00024.

(66)   Neware BTS4000 Series – Customizable Output Power Range and Functions – Neware Battery Testers.

(67)   Bard, A. J.; Faulkner, L. R. *Electrochemical Methods: Fundamentals and Applications*; Wiley: New York, 2001.

(68)   Guo, X.; Zhou, J.; Bai, C.; Li, X.; Fang, G.; Liang, S. Zn/MnO2 Battery Chemistry with Dissolution-Deposition Mechanism. *Mater. Today Energy* **2020**, *16*, 100396. https://doi.org/10.1016/j.mtener.2020.100396.

(69)   Lee, B.; Seo, H. R.; Lee, H. R.; Yoon, C. S.; Kim, J. H.; Chung, K. Y.; Cho, B. W.; Oh, S. H. Critical Role of PH Evolution of Electrolyte in the Reaction Mechanism for Rechargeable Zinc Batteries. *ChemSusChem* **2016**, *9* (20), 2948–2956. https://doi.org/10.1002/cssc.201600702.

(70)   Kohler, T.; Armbruster, T.; Libowitzky, E. Hydrogen Bonding and Jahn–Teller Distortion in Groutite,α-MnOOH, and Manganite,γ-MnOOH, and Their Relations to the Manganese Dioxides Ramsdellite and Pyrolusite☆. **1997**. https://doi.org/10.1006/JSSC.1997.7516.

(71)   Swanson, H. E. Standard X-Ray Diffraction Powder Patterns: Section 10- Data for 84 Substances. 166.

(72)   Frondel, C. New Manganese Oxides: Hydrohausmannite and Woodruffite*. *Am. Mineral.* **1953**, *38* (9–10), 761–769.

(73)   Bauman, W. C.; Eichhorn, J. Fundamental Properties of a Synthetic Cation Exchange Resin. *J. Am. Chem. Soc.* **1947**, *69* (11), 2830–2836. https://doi.org/10.1021/ja01203a065.

(74)   Chowdiah, V.; Foutch, G. L. A Kinetic Model for Cationic-Exchange-Resin Regeneration. *Ind. Eng. Chem. Res.* **1995**, *34* (11), 4040–4048. https://doi.org/10.1021/ie00038a045.

(75)   Ghosh, S.; Dhole, K.; Tripathy, M.; Kumar, R.; Sharma, R. FTIR Spectroscopy in the Characterization of the Mixture of Nuclear Grade Cation and Anion Exchange Resins. *J. Radioanal. Nucl. Chem.* **2015**, *304*. https://doi.org/10.1007/s10967-014-3906-3.

(76)   Strasheim, A.; Buijs, K. Infra-Red Spectra of Ion-Exchangers on Polystyrene Base. *Spectrochim. Acta* **1961**, *17* (4), 388–392. https://doi.org/10.1016/0371-1951(61)80090-8.

(77)   Wang, S.; Yuan, Z.; Zhang, X.; Bi, S.; Zhou, Z.; Tian, J.; Zhang, Q.; Niu, Z. Non-Metal Ion Co-Insertion Chemistry in Aqueous Zn/MnO2 Batteries. *Angew. Chem. Int. Ed.* **2021**, *60* (13), 7056–7060. https://doi.org/10.1002/anie.202017098.

(78)   Yang, H.; Chang, Z.; Qiao, Y.; Deng, H.; Mu, X.; He, P.; Zhou, H. Constructing a Super-Saturated Electrolyte Front Surface for Stable Rechargeable Aqueous Zinc Batteries. *Angew. Chem. Int. Ed.* **2020**, *59* (24), 9377–9381. https://doi.org/10.1002/anie.202001844.

(79)   Wang, J.; Wang, J.-G.; Qin, X.; Wang, Y.; You, Z.; Liu, H.; Shao, M. Superfine MnO2 Nanowires with Rich Defects Toward Boosted Zinc Ion Storage Performance. *ACS Appl. Mater. Interfaces* **2020**, *12* (31), 34949–34958. https://doi.org/10.1021/acsami.0c08812.

(80)   Li, J.; Chen, Y.; Guo, J.; Wang, F.; Liu, H.; Li, Y. Graphdiyne Oxide-Based High-Performance Rechargeable Aqueous Zn–MnO2 Battery. *Adv. Funct. Mater.* **2020**, *30* (42), 2004115. https://doi.org/10.1002/adfm.202004115.